Abstract

Effects of Hard but Finite Pi Pulses: From Uncontrolled Coherence Flow to Extreme Line-narrowing and MRI of Solids

Yanqun Dong

May 2009

This doctoral dissertation presents a detailed NMR study of the surprisingly large effects arising from the non-zero duration of strong π pulses in spin-$\frac{1}{2}$ dipolar solids, and the development of new technique for spin coherence control based on our understanding of the finite pulse effects.

When multiple phase-coherent π pulses are applied, NMR experiments of various dipolar solids have shown results that conflict with the conventional expectations set by the δ-pulse approximation, even when the pulses are unusually strong. One of the most dramatic results is the observation of either a long-lived echo train, or a fast decay of echoes, depending on the phase of pulses. This phenomenon is referred to as the Pulse Sequence Sensitivity (PSS) in this thesis. With the help of simulations, we demonstrated the importance of the non-zero duration of pulses for this effect. Simulations with N spins ($4 \leq N \leq 8$) and an inflated dipolar coupling strength can reproduce the PSS observed in experiments. Further simulations with

the snapshots of density matrix also indicate that the internal structure of π pulses (the system's internal Hamiltonian under π pulses) opens up extra coherence pathways that contribute to the long-lived echo tail in simulations.

Using Average Hamiltonian theory, the leading correction terms arising from the non-zero duration of pulses were identified and their important roles are discussed. Using the zeroth and first-order average Hamiltonian terms, a new class of spin echoes were designed and demonstrated in experiments. The good agreement between our theoretical predictions and the experimental observations indicated that the tiny difference between hard π pulses and their δ-pulse approximation could be used as a new way for coherence control. Using this new technique, new approaches to extreme line-narrowing (the linewidth a Silicon sample was reduced by a factor of nearly 70,000) and magnetic resonance imaging of solids are presented.

Effects of Hard but Finite Pi Pulses: From Uncontrolled Coherence Flow to Extreme Line-narrowing and MRI of Solids

A Dissertation

Presented to the Faculty of the Graduate School

of

Yale University

in Candidacy for the Degree of

Doctor of Philosophy

by

Yanqun Dong

Dissertation Director: Professor Sean E. Barrett

May 2009

To My Parents

Contents

Words of Acknowledgment

Before I came to the United States in 2002, I got an email from Sean inviting me to do a summer project in his lab. I said yes because I figured if I did not like my experience in the summer I could always switch to another lab, and I could use this opportunity to explore Yale before school started. Well, the Barrett lab turned out to be the first and also the last Physics lab I have worked at Yale.

During my first summer at the Barrett lab, I was hooked by their fascinating NMR "puzzles." Moreover, I really enjoyed working with all my colleagues, Anatoly Dementyev, Dale Li, and Kenny MacLean. I thank them all for their help and friendship through these years, especially Tolya and Dale. They were always there to explain to me their NMR knowledge, teach me how to use the software, show me how to set up the spectrometer, and pass to me the wisdom they had gained through their diligent work.

The biggest reason that made me decide to stay in the Barrett lab was Sean. I believe that an interesting project is an important factor in selecting a lab, but a good advisor is even more important. Sean is one of the most talented, approachable, and supportive advisors I have ever seen. In the Barrett lab, there is no such thing

as a stupid question. I can always feel comfortable asking Sean questions, and he always explains to me or discusses with me no matter how trivial the question may sound. From Sean, I have not only learned Physics, but also acquired the important quality of perseverance. The process of finishing this thesis work is certainly not an easy one. Very often we perceived doubts and heard discouraging comments from other colleagues at academic conferences. At times I was on the verge of giving up and wanting to switch to a new project. It was Sean who encouraged me and restored belief back in my heart. I admire Sean for his optimism, his courage, and his spirit that has kept us moving forward.

In 2004, Rona Ramos joined the Barrett lab and I could not be happier. I got not only one more talented colleague, but also a good girl friend that I could share a lot of things with. In the past few years, as an international student trying to adjust herself to the new culture and learn the new language, I got tremendous help from Rona both in work and in life and I cannot thank her enough. Rona has also worked closely with me on this thesis project. In later years, there were a few bright undergraduate students doing senior projects in the Barrett lab, and John Murray was one of them. John made important contributions to our project, and I am thankful to him.

I would also like to give my special thanks to Michel Devoret, Steven Girvin, Jack Sandweiss, Charles Slichter, and Kurt Zilm for their well-informed opinions and helpful feedback to our work and manuscripts. I also want to thank David DeMille, Steven Lamoreaux, and John Harris for serving on my thesis committee.

Steven Girvin and David also took time out of their busy schedules to write me a recommendation letter for my future career. I am also in debt to Xiaoling Wu and E. K. Paulson for their generous assistance with performing some experiments reported in this thesis. I also thank V. Dobrovitski for the helpful communication between us.

Last but not the least, I want to thank my families, especially my husband Min and my parents. Without their unconditional love and support, I could never have finished this thesis.

In the June of 2008, my son Benjamin was born. During my pregnancy and my maternity leave, Sean, Rona, my families, and every friend around me have been extremely considerate and supportive. Their kindness has left my heart filled with warmth and gratitude that I will treasure for the rest of my life.

Sincerely,

Yanqun Dong

List of Figures

List of Tables

Glossary of Terms

AHT	Average Hamiltonian Theory	74
APCP	Alternating-Phase CP pulse sequence	47
APCPMG	Alternating-Phase CPMG pulse sequence	47
B_{ij}	Dipolar coupling constant $B_{ij} = \frac{1}{2}\frac{\gamma^2\hbar^2}{r_{ij}^3}(1 - 3\cos^2\theta_{ij})$	35
CCW	Counter-Clockwise	109
CW	Clockwise	109
CP	Carr-Purcell pulse sequence	47
CPMG	Carr-Purcell-Meiboom-Gill pulse sequence	43
DANTE	Delays Alternating with Nutations for Tailored Excitation	142
DDS	Direct Digital Synthesizer	29
DBM	Double Balanced Mixer	30
DR	Disorder Realization	54
FID	Free Induction Decay	37
FWHM	Full Width at Half Maximum	37
γ	Gyromagnetic ratio	11
$\hbar$	Planck's constant divided by 2π	8

H_0	External magnetic field	12
ω_1, H_1	Pulse strength	36
$\bar{\mathcal{H}}^{(0)}$	The zeroth order average Hamiltonian	77
$\bar{\mathcal{H}}^{(1)}$	The first order average Hamiltonian	77
HE	Hahn Echo or Spin Echo	41
$\mathcal{H}_p$	The pulse Hamiltonian $\mathcal{H}_p = -\hbar\omega_1 I_{\phi_T}, \quad \phi = x, y, z$	36
$\mathcal{H}_Z$	Zeeman Hamiltonian $\mathcal{H}_Z = \sum_{i=1}^{N} \Omega_{z_i} I_{z_i}$	36
$\mathcal{H}_{zz}$	Secular Dipolar Hamiltonian $\mathcal{H}_{zz} = \sum_{j>i}^{N} B_{ij}(3I_{z_i}I_{z_j} - \vec{I}_i \cdot \vec{I}_j)$	35
$\mathcal{H}_{int}$	The internal Hamiltonian of a dipolar spin system $\mathcal{H}_{int} = \mathcal{H}_Z + \mathcal{H}_{zz}$	36
$\widetilde{\mathcal{H}_{int}}$	The internal Hamiltonian in the toggling frame	76
$\mathcal{H}_{tot}$	The total Hamiltonian during a pulse $\mathcal{H}_{tot} = \mathcal{H}_{int} + H_p$	36
I_+, I_-	Spin ladder operators	8
I_x, I_y, I_z	Spin operators	8
$I_{x_T}, I_{y_T}, I_{z_T}$	$I_{\phi_T} = \sum_{i=1}^{N} I_{\phi_i}, \quad \phi = x, y, z$	36
MRI	Magnetic Resonance Imaging	132
N	The number of spins included in simulations	54
NMR	Nuclear Magnetic Resonance	7
ω_0	Larmor frequency	14
Ω_z^{loc}	The local Zeeman shift	106

Ω_{offset}^{global}	The global Zeeman offset	106
Ω_z^{net}	The total Zeeman shift $\Omega_z^{net} = \Omega_{offset}^{global} + \Omega_z^{loc}$	106
$\Phi_Z(t)$	The Zeeman phase angle	112
$\Phi_D(t)$	The dipolar phase angle	112
PSS	Pulse Sequence Sensitivity	47
QC	Quantum Coherence	90
RF	Radio Frequency	20
$\rho(t)$	The Density Matrix as a function of time	48
$\sigma_x, \sigma_y, \sigma_z$	Pauli Matrices	11
T_1	Spin-lattice relaxation time	21
T_2	Transverse relaxation time	21
t_c	The cycle time for a cyclic sequence	75
t_p	Pulse duration	36
$\{\phi_1, \phi_2\}$	Basic repeating block $(\tau - 180_{\phi_1} - \tau - \tau - 180_{\phi_2} - \tau)$	107
$\{N, \delta, \psi_1, \psi_2\}$	Big repeating block $(\Delta+\delta)$–90_{ψ_1}–$\{-X,X\}^{\frac{N}{2}}\{X,-X\}^{\frac{N}{2}}$–$90_{\psi_2}$–$(\Delta-\delta)$	120

Chapter 1

Thesis Outline

This thesis focuses on a detailed investigation of the surprisingly large effects arising from the non-zero duration of pulses in NMR experiments where many strong and phase-coherent π pulses are applied.

The whole story begins with the observation of a discrepancy between two standard methods for measuring the spin-spin relaxation time T_2. Based on the conventional δ-pulse approximation for strong pulses, the multiple-π-pulse CPMG measurement should agree with the two-pulse Hahn echo measurement. However, in experiments on simple solids like Silicon, the CPMG sequence gives a long-lived echo tail, which diverges from the fast decay of Hahn echoes. Moreover, multiple-π-pulse sequences using different pulse phases give dramatically different results, which we refer to as the pulse sequence sensitivity (PSS) effect. This PSS phenomenon is also surprising, since the spin-echo decay should not depend on the phase of π pulses within the δ-pulse approximation.

To explain those observations, we first spent a lot of time and effort quantifying

the experimental errors and improving the experimental conditions. However, despite of all the experimental improvements, the PSS effect still persisted in all the test samples, which led us to believe that it was an intrinsic effect. We then started to question the validity of the basis for our predictions: the δ-pulse approximation.

We used computer simulations to investigate the effects of the non-zero duration of π pulses used in experiments. For just a few spins and normal dipolar coupling strength ($1 \times B_{ij}$), the simulations did not show a big PSS. However, we found that the dramatic PSS effect could be reproduced in finite-pulse simulations with just a few spins provided that a larger than normal dipolar coupling strength (e.g. $25 \times B_{ij}$) was used. We made the projection that if a large enough number of spins could be included, then maybe simulations with the regular dipolar coupling strength could show big PSS effect. This projection was supported by the discovery that the height of CPMG echo tail increased with spin number N for the range of N values we tried.

It is important to stress the fact that for each single π pulse, the difference between the δ-pulse approximation and the exact π pulse is tiny. Only when many phase-coherent π pulses are applied in a train, the effects from the non-zero duration of pulses will become pronounced.

To better understand these exact numerical results, we used average Hamiltonian theory to identify the leading-order correction terms arising from the non-zero duration of π pulses. Simulations with leading-order average Hamiltonian showed that the correction terms play an important role in producing the long-lived echo

tail. Using the snapshots of the density matrix and the knock-out manipulations, we showed that the correction terms arising from the non-zero duration of π pulses could open extra coherence pathways that produced the echo tail. However, we did not know quantitatively how much each term contributed to the measured NMR signal since the leading-order average Hamiltonian terms were still too complicated to allow quantitative analysis. This is what the "uncontrolled coherence flow" in the title is referring to, i.e., the long-lived echo tail of CPMG is not a result of intentional coherence control.

We then designed and demonstrated a series of spin echo experiments where the special effects arising from the non-zero duration of pulses could be quantified using an approximate average Hamiltonian. The good quantitative agreement between the theoretical predictions and the experimental observations indicated that the effects of the non-zero duration of π pulses were important in real experiments, and that they could be used as a new technique for spin coherence control. We later used this technique to develop new pulse sequences for extreme line-narrowing and MRI of solids.

The outline of this thesis is listed below:

Chapter 2 gives the reader an introduction to the basic spin physics and the fundamentals of NMR theory. This chapter is only a rough sketch of such topics and the interested reader is encouraged to refer to some excellent NMR books [1, 23, 60, 84] for more details.

Chapter 3 offers an overview of the basic hardware needed to perform high resolution NMR experiments, including the superconducting magnet, the sample probe, the RF transmitter and the quadrature detector. Again, this chapter only offers a brief review of such topics and the reader can refer to the comprehensive book by E. Fukushima and S. B. W. Roeder [27] for more details.

Chapter 4 describes the surprising observations in our earliest NMR experiments on Silicon (Figure 4.5 and Figure 4.6). This chapter first introduces the δ-pulse approximation and the basic NMR experiments, to help the reader understand why we call those observed effects as "surprising."

Chapter 5 presents the results of simulations with non-zero duration π pulses. It first discusses the finite-pulse simulations using weak pulses and big Zeeman shifts. Such simulations can produce a long-lived echo tail in CPMG, but the echo tail height decreases as the pulse strength is increased (Figure 5.2), which contradicts to our experimental observation that the height of CPMG echo tail remains flat over a large range of pulse strength (Figure 5.3). Later, the results from liquid crystal 5CB experiments inspired us to inflate the dipolar coupling strength B_{ij} in the finite-pulse simulations. Such simulations can reproduce the CPMG long-lived echo tail (Figure 5.8) and the PSS effect (Figure 5.12). Moreover, the height of CPMG echo tail depends on the number of spins included in the simulations, which suggests that if a large enough number of spins can be included, the finite-pulse simulations may produce a pronounced echo tail for CPMG and PSS effect even when normal dipolar

coupling strength is used.

Chapter 6 describes how to use the average Hamiltonian theory to identify the correction terms arising from the non-zero duration of pulses. It starts with an outline of the average Hamiltonian theory, then it shows how to use those formula to calculate the zeroth and the first order average Hamiltonian for the multiple π pulse sequences (Equation (6.20) to Equation (6.27)). Included in this chapter are also simulations with the average Hamiltonian terms. An important result is that the correction terms in the first order average Hamiltonian play a crucial role in producing the CPMG echo tail (Figure 6.3).

Chapter 7 investigates the extra coherence pathways opened by the correction terms arising from the non-zero duration of π pulses. Special density matrix manipulations are used to demonstrate that such extra coherence pathways can contribute to the long-lived CPMG echo tail (Figure 7.3 and Figure 7.4). However, we do not have a quantitative understanding of how exactly each term contributes to the spin echo tail. Therefore, we consider the coherence flow in CPMG as uncontrolled, which is in contrast to the specially designed and controlled spin echo experiments presented in the next two Chapters. Snapshots of the density matrix are also used to compare the dramatic difference between the pulse sequences using multiple π pulses and multiple $\pi/2$ pulses (Figure 7.6 and Figure 7.7).

Chapter 8 demonstrates a new series of spin echo experiments designed with just the leading order correction terms arising from the non-zero duration of π pulses.

This series of experiments serve two purposes. The first is to further convince the reader that the special effects resulting from the tiny duration of π pulses are not experimental artifacts, but are real. The second is to see if we could give quantitative analysis to these echo phenomena since we did not have a quantitative explanation for the CPMG echo tail. Analogies of the FID, the Hahn echo, the CPMG echo train, and the magic echo are presented (Figure 8.1 and Figure 8.2). A new kind of echo called quadratic echo is also demonstrated (Figure 8.3). For all these experiments, our model offers good quantitative explanations to the experimental results, which is a big improvement from our understanding of the CPMG echo tail.

Chapter 9 presents new pulse sequences that were designed based on our understanding of the spin echo phenomena described in Chapter 8 and their applications in extreme line-narrowing and MRI of solids. A progress report is given for the line-narrowing experiments as the performance is improved from a linewidth reduction of $\sim$ 1000 (Figure 9.1) to $\sim$ 10000 (Figure 9.3), and finally to $\sim$ 70000 (Figure 9.5). The possibility of using a new pulse sequence to achieve MRI of solids is demonstrated in the well-reproduced top-hat line shapes (Figure 9.11). Our progress toward 3-dimentional imaging of solids is also discussed and demonstrated (Figure 9.15).

A list of symbols and acronyms can be found in the glossary list right before this Chapter. The appendix offers a detailed instruction to the CPMG simulation procedure written in Igor 5.03 that we used to carry out some of the simulations presented in the thesis.

Chapter 2

Introduction to Spin Physics and NMR

Spin, the intrinsic angular momentum, is a fundamental property of elementary particles such as electrons and protons, just like their electric charge and mass. Each individual unpaired electron, proton and neutron has a spin of $\frac{1}{2}$. In this thesis, we are going to focus on nuclear spin, the total spin of protons and neutrons for a given atom. According to the shell model, the nucleons, just like electrons filling the orbitals outside the nucleus, also fill orbitals [14], and their spin can pair up to eliminate the observable spin. For example, Helium $^4_2$He has one proton pair and one neutron pair, and the total nuclear spin is zero. Almost every element in the periodic table has an isotope with a non-zero nuclear spin I. In this Chapter, we will review the basics of spin physics and the fundamentals of nuclear magnetic resonance (NMR theory. Many books provide a great introduction to NMR theory [1, 23, 24, 27, 84].

2.1 Spin Operators

From classical mechanics to quantum mechanics, we replace the classical dynamical quantities by quantum operators [81], for example, we replace the classical momentum $\vec{P}$ by $-i\hbar\vec{\bigtriangledown} = (-i\hbar\frac{\partial}{\partial x}, -i\hbar\frac{\partial}{\partial y}, -i\hbar\frac{\partial}{\partial z})$ where $\hbar$ is the Plank constant divided by 2π. However, spin, the intrinsic angular momentum, does not have a classical equivalent, so we have to use new operators to treat spin in quantum mechanics. Pauli came up with the the special form of spin operators [81], $\vec{S} = (S_x, S_y, S_z)$, with the eigenvalues of $\pm\frac{1}{2}\hbar$ for each component in the case of spin-$\frac{1}{2}$. For simplicity, dimensionless operators $\vec{I} = (I_x, I_y, I_z) = \frac{1}{\hbar}\vec{S}$ are often used. I_x, I_y, and I_z have the following important commutation properties [81],

$$[I_x, I_y] = iI_z, \qquad [I_y, I_z] = iI_x, \qquad [I_z, I_x] = iI_y \tag{2.1}$$

and

$$\vec{I}^2 \mid j,m\rangle = j(j+1) \mid j,m\rangle \tag{2.2}$$

$$I_z \mid j,m\rangle = m \mid j,m\rangle \tag{2.3}$$

where $\mid j,m\rangle$ is a simultaneous eigenstate of $\vec{I}^2$ and I_z, and there are $2j+1$ possible values of m.

$$m = -j, -j+1, \cdots j-1, j \tag{2.4}$$

Often it is convenient to work with the non-Hermitian operators called the ladder operators [81],

$$I_\pm \equiv I_x \pm iI_y \tag{2.5}$$

which will raise or lower the quantum number m by 1,

$$I_{\pm} \mid j,m\rangle = \sqrt{j(j+1) - m(m\pm 1)} \mid j,m\pm 1\rangle \tag{2.6}$$

and $I_{\pm}$ satisfy the following commutation relations,

$$[I_+, I_-] = 2I_z \tag{2.7}$$

$$[I_z, I_{\pm}] = \pm I_{\pm} \tag{2.8}$$

$$[\vec{I}^2, I_{\pm}] = 0 \tag{2.9}$$

In this thesis, we are going to concentrate on spin-$\frac{1}{2}$. For spin-$\frac{1}{2}$, it is conventional to use a simple notation $|\uparrow\rangle$ to represent "spin up" state with $m = \frac{1}{2}$, and $|\downarrow\rangle$ to represent "spin down" state with $m = -\frac{1}{2}$ [81],

$$I_z |\uparrow\rangle = \frac{1}{2} |\uparrow\rangle \tag{2.10}$$

$$I_z |\downarrow\rangle = -\frac{1}{2} |\downarrow\rangle \tag{2.11}$$

2.2 Matrix Representations and Pauli Matrices

When treating spins in quantum mechanics, it is often convenient to represent the spin operators with matrices. We now show how to represent an operator by a square matrix [84].

Let us assume operator A has eigenwaves $\mid a_1\rangle, \mid a_2\rangle, \ldots \mid a_N\rangle$, which form a ket space with dimensionality of N, and

$$A \mid a_i\rangle = a_i \mid a_i\rangle, \qquad i = 1, 2, \ldots N \tag{2.12}$$

The simplest operator in this ket space is the identity operator,

$$1 = \sum_{i=1}^{N} \mid a_i\rangle\langle a_i \mid \tag{2.13}$$

Inserting identity operators, we can represent operator A as,

$$A = \sum_{i=1}^{N}\sum_{j=1}^{N} \mid a_i\rangle\langle a_i \mid A \mid a_j\rangle\langle a_j \mid \tag{2.14}$$

There are N^2 numbers in the form of $\langle a_i \mid A \mid a_j\rangle$ and we may arrange them in an $N \times N$ matrix with $\langle a_i \mid A \mid a_j\rangle$ being the i^{th} row and j^{th} column. Explicitly, the matrix looks like this,

$$A \doteq \begin{pmatrix} \langle a_1 \mid A \mid a_1\rangle & \langle a_1 \mid A \mid a_2\rangle & \cdots & \langle a_1 \mid A \mid a_N\rangle \\ \langle a_2 \mid A \mid a_1\rangle & \langle a_2 \mid A \mid a_2\rangle & \cdots & \langle a_2 \mid A \mid a_N\rangle \\ \vdots & \vdots & \vdots & \vdots \\ \langle a_N \mid A \mid a_1\rangle & \langle a_N \mid A \mid a_2\rangle & \cdots & \langle a_N \mid A \mid a_N\rangle \end{pmatrix} \tag{2.15}$$

where $\doteq$ stands for "is represented by."

For the case of spin-$\frac{1}{2}$, spin angular momentum operator I_z has only two eigenstates, $|\uparrow\rangle$ and $|\downarrow\rangle$. Applying Equation (2.14), I_z can be written as,

$$I_z = (|\uparrow\rangle\langle\uparrow| + |\downarrow\rangle\langle\downarrow|)I_z(|\uparrow\rangle\langle\uparrow| + |\downarrow\rangle\langle\downarrow|) \tag{2.16}$$

Applying the following equations,

$$\langle\uparrow| I_z |\uparrow\rangle = \frac{1}{2}, \qquad \langle\downarrow| I_z |\downarrow\rangle = -\frac{1}{2}, \qquad \langle\uparrow| I_z |\downarrow\rangle = 0, \qquad \langle\downarrow| I_z |\uparrow\rangle = 0$$

we get the matrix representation for I_z in the eigenstate space of I_z or so-called I_z basis,

$$I_z \doteq \begin{pmatrix} \frac{1}{2} & 0 \\ 0 & -\frac{1}{2} \end{pmatrix} = \frac{1}{2}\begin{pmatrix} 1 & 0 \\ 0 & -1 \end{pmatrix} \tag{2.17}$$

Getting the matrix representation for I_x and I_y in the I_z basis is a little bit trickier. From equation (2.5), we get

$$I_x = \frac{1}{2}(I^+ + I^-) \tag{2.18}$$

$$I_y = -\frac{i}{2}(I^+ - I^-) \tag{2.19}$$

Using the facts that,

$$I^+ |\uparrow\rangle = 0, \qquad I^- |\downarrow\rangle = 0, \qquad I^+ |\downarrow\rangle = |\uparrow\rangle, \qquad I^- |\uparrow\rangle = |\downarrow\rangle$$

We get the following matrix representations in the I_z basis,

$$I_x \doteq \begin{pmatrix} 0 & \frac{1}{2} \\ \frac{1}{2} & 0 \end{pmatrix} = \frac{1}{2}\begin{pmatrix} 0 & 1 \\ 1 & 0 \end{pmatrix} \tag{2.20}$$

$$I_y \doteq \begin{pmatrix} 0 & -\frac{i}{2} \\ \frac{i}{2} & 0 \end{pmatrix} = \frac{1}{2}\begin{pmatrix} 0 & -i \\ i & 0 \end{pmatrix} \tag{2.21}$$

These three matrices

$$\sigma_z = \begin{pmatrix} 1 & 0 \\ 0 & -1 \end{pmatrix}, \quad \sigma_x = \begin{pmatrix} 0 & 1 \\ 1 & 0 \end{pmatrix}, \quad \sigma_y = \begin{pmatrix} 0 & -i \\ i & 0 \end{pmatrix} \tag{2.22}$$

are called Pauli matrices [81].

2.3 Spin Energy Levels and Magnetic Resonance

For an intrinsic spin $\vec{I}$, there is also an intrinsic magnetic moment $\vec{\mu}$ that is proportional to $\vec{I}$,

$$\vec{\mu} = \gamma\hbar\vec{I} \tag{2.23}$$

where γ is the gyromagnetic ratio [84]. Some of the most frequently investigated nuclei are listed in Table 2.1 [49].

When placed in a magnetic field, the interaction between the magnetic moment $\vec{\mu}$ and the external magnetic field $\vec{H}_0$ gives a simple Hamiltonian:

$$\mathcal{H} = -\vec{\mu} \cdot \vec{H}_0 \tag{2.24}$$

Taking $\vec{H}_0$ to be along the Z-axis, we get

$$\mathcal{H}_z = -\gamma\hbar H_0 I_z. \tag{2.25}$$

The eigenvalue of I_z is simply m, where $m = -I, -I+1, \cdots I$. Therefore the eigenvalue of $\mathcal{H}_z$ is

$$\mathcal{E}_z = -\gamma\hbar H_0 m, \qquad m = -I, -I+1, \cdots I \tag{2.26}$$

which corresponds to a series of equally-spaced energy levels with the difference of $\gamma\hbar H_0$ between two adjacent ones. A spin in a lower energy level can be excited to a higher energy level when a photon with its energy matching the energy difference is absorbed by the spin. This is the basic concept of nuclear magnetic resonance (NMR) or electron spin resonance (ESR).

Nuclear spins are typically excited using an alternating magnetic field applied perpendicular to the static filed $\vec{H}_0$. For an alternating magnetic field along X-axis

Nuclei	Spin I	γ (MHz/T)
^{1}H	1/2	42.58
^{2}H	1	6.54
^{13}C	1/2	10.71
^{19}F	1/2	40.08
^{29}Si	1/2	-8.46
^{31}P	1/2	17.24

Table 2.1: Some commonly investigated nuclear spins

$H_1 \cos(\omega t)\hat{x}$, the resonance condition is met when

$$\hbar\omega = \Delta E \tag{2.27}$$

where ΔE is the energy difference between the initial and final spin states. Take ^1H, which is spin-$\frac{1}{2}$, as an example. This nuclear spin has two energy levels in an external magnetic $\vec{H}_0$ along the Z direction, the lower energy level, corresponding to the spin lining up to the magnetic field $\vec{H}_0$, and the higher energy level, corresponding to the spin lining anti-parallel to the magnetic field $\vec{H}_0$. The energy splitting is $\gamma\hbar H_0$. To achieve resonance, the exciting magnetic field needs to have the alternating frequency of $\omega = \gamma H_0$.

When a group of many spins are in an external magnetic field, the spin distribution among the different energy levels can be approximated by Boltzmann statistics [54]. For spin-$\frac{1}{2}$ nuclei, when in equilibrium the number of spins in the lower energy level N_+ is higher than the number of spins in the higher energy level N_- , and they have the following relation,

$$\frac{N_-}{N_+} = e^{-\Delta E/kT} \tag{2.28}$$

where ΔE is the energy difference between the two levels, k is Boltzmann's constant, and T is temperature in Kelvin. The net magnetic moment of the many spin system is proportional to $N_+ - N_-$, which, according to Equation (2.28), increases with decreasing temperature, and approaches to zero as the temperature is increased toward infinity. In NMR experiments, good signal relies on a big net magnetic moment from the sample, and this is why some experiments are carried out at low temperature.

2.4 Magnetic Resonance in the Rotating Frame

2.4.1 Without Any Pulse

Before we introduce the rotating frame, let us first look at the classical description of the motion of a magnetic moment $\vec{\mu}$ in a constant external magnetic field $\vec{H}_0$. The magnetic moment experiences a torque $\vec{\tau} = \vec{\mu} \times \vec{H}_0$, and this torque causes the angular momentum $\vec{J}$ to change according to the following equation,

$$\frac{d\vec{J}}{dt} = \vec{\mu} \times \vec{H}_0 \tag{2.29}$$

and since $\vec{\mu} = \gamma \vec{J}$, we can eliminate $\vec{J}$ and get,

$$\frac{d\vec{\mu}}{dt} = \vec{\mu} \times (\gamma \vec{H}_0) \tag{2.30}$$

This equation shows that at any instant the change of $\vec{\mu}$ is perpendicular to both the direction of $\vec{\mu}$ and $\vec{H}_0$. As a result, both the magnitude of $\vec{\mu}$ and the angle θ between $\vec{\mu}$ and $\vec{H}_0$ is fixed, and the magnetic moment $\vec{\mu}$ precesses around $\vec{H}_0$ with a constant angular velocity, forming a cone. This constant angular frequency $\vec{\omega}_0 = \gamma \vec{H}_0$ is called the Larmor frequency [84].

It is obvious that if we jump into a frame that is rotating at the Larmor frequency around the external magnetic field $\vec{H}_0$, then the magnetic moment $\vec{\mu}$ will appear to be static. In the Newtonian classical physics, when considering an object of mass m in an accelerating frame, we add a pseudo-force in the amount of $-m\vec{a}$ to the object of interest, where $\vec{a}$ is the acceleration of the frame. Similarly, if we consider the spin motion in a frame that is rotating with angular velocity $\vec{\Omega}$, we add a "pseudo-torqe"

to the spin,

$$\begin{aligned} \frac{\partial \vec{\mu}}{\partial t} &= \vec{\mu} \times \gamma \vec{H}_0 - \vec{\Omega} \times \vec{\mu} \\ &= \vec{\mu} \times (\gamma \vec{H}_0 + \vec{\Omega}) \end{aligned} \tag{2.31}$$

Equation (2.31) tells us that in the rotating frame the spin obeys an equation with the same form, except with a revised effective magnetic field $\vec{H}_{eff}$

$$\vec{H}_{eff} = \vec{H}_0 + \frac{\vec{\Omega}}{\gamma} \tag{2.32}$$

Clearly when $\vec{\Omega} = -\gamma \vec{H}_0$, the spin is static in the rotating frame.

2.4.2 With an External Pulse

In the last section, we mentioned that an alternating magnetic field is often used to exite spins in NMR or ESR experiments. Let us now look at the effect of an alternating magnetic field in the rotating frame. If we assign the direction of the big external static magnetic field to be $\hat{z}$, then the alternating magnetic fields applied to excite spins are normally in the transverse X-Y plane. Let us turn on an alternating magnetic field in the $\hat{x}$ direction of the lab frame, $\vec{H}_1(t) = 2H_1 \cos(\omega t)\hat{x}$, as an example. This field can be readily broken down into two rotating components, $\vec{H}_r$ and $\vec{H}_l$,

$$\vec{H}_r = H_1(\cos(\omega t)\hat{x} + \sin(\omega t)\hat{y})$$

$$\vec{H}_l = H_1(\cos(\omega t)\hat{x} - \sin(\omega t)\hat{y})$$

where $\vec{H}_r$ is rotating counterclockwise with angular velocity of $\omega\hat{z}$ and $\vec{H}_l$ clockwise with angular velocity of $-\omega\hat{z}$. If we choose a rotating frame that makes one magnetic

field component, say H_l, to be static, then the other component will appear to rotate at twice of the angular velocity 2ω. In the practice of NMR, ω is in the order of MHz, and the characteristic time Δt of the processes we are interested in is often in the order of milliseconds or even seconds. When $\omega \cdot \Delta t \gg 1$, which is almost always true in NMR, the effect of the fast-rotating magnetic field averages out and can be typically ignored in the rotating frame. Therefore, in the rotating frame that makes $\vec{H}_l$ static, we will just drop $\vec{H}_r$ (either $\vec{H}_l$ or $\vec{H}_r$ looks static in the rotating frame, depending on the sign of γ for a particular type of nuclei).

In the lab frame, we have

$$\frac{d\vec{\mu}}{dt} = \vec{\mu} \times \gamma[H_0\hat{z} + 2H_1 \cos(\omega t)\hat{x}] \tag{2.33}$$

Going to the rotating frame with angular velocity of $\vec{\Omega} = -\omega\hat{z}$, the pulse field is simply $H_1\hat{x}$, and Equation (2.33) becomes

$$\begin{aligned} \frac{\partial\vec{\mu}}{\partial t} &= \vec{\mu} \times [(\gamma H_0 - \omega)\hat{z} + \gamma H_1\hat{x}] \\ &= \vec{\mu} \times \gamma[(H_0 - \frac{\omega}{\gamma})\hat{z} + H_1\hat{x}] \\ &= \vec{\mu} \times \gamma\vec{H}_{eff} \end{aligned} \tag{2.34}$$

Where

$$\vec{H}_{eff} = (H_0 - \frac{\omega}{\gamma})\hat{z} + H_1\hat{x} \tag{2.35}$$

When on resonance or near resonance, the frequency of the pulses matches or close to the Larmor frequency, we have $H_0 - \frac{\omega}{\gamma} \cong 0$ and the effective magnetic field in the rotating frame is nothing but a constant field in $\hat{x}$ direction. Assuming the

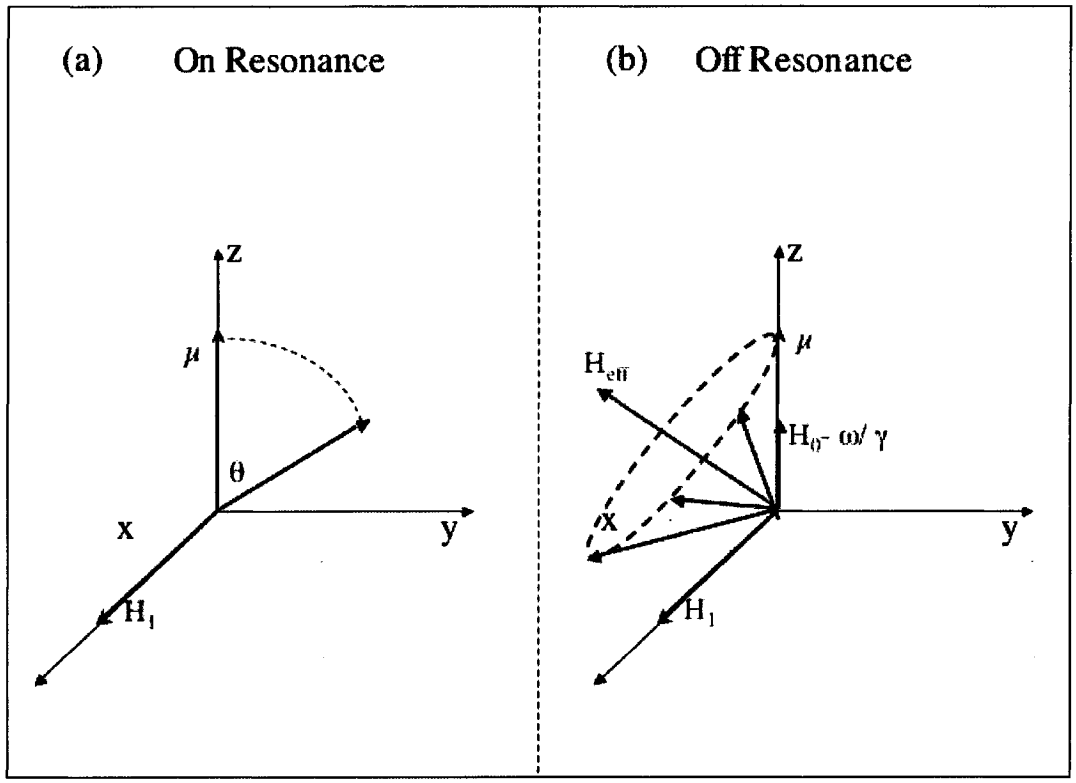

Figure 2.1: The movement of magnetic moment $\vec{\mu}$ in the rotating frame for on resonance (a) and off resonance (b) conditions. Note that $\vec{\mu}$ is initially along $\hat{z}$ and the pulse $\vec{H}_1$ is along $\hat{x}$.

initial magnetic moment is along $\hat{z}$, in this case $\vec{\mu}$ will rotate around $H_1\hat{x}$ in the Y-Z plane by an angle that is determined by the duration of the pulse. When it is off resonance and $H_0 - \frac{\omega}{\gamma}$ is not negligible, $\vec{H}_{eff}$ will be out of the transverse plane and $\vec{\mu}$ will precess around $\vec{H}_{eff}$, forming a cone as illustrated in Figure 2.1.

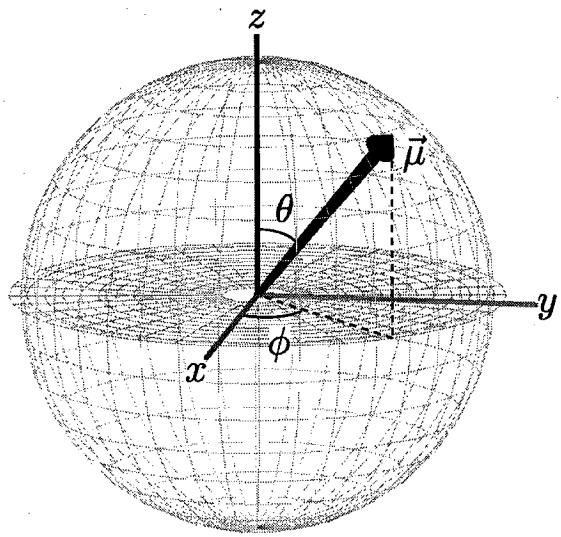

Figure 2.2: The Bloch Sphere representation of a magnetic moment $\vec{\mu}$. Any orientation of $\vec{\mu}$ can be described by the two phase angles θ and ϕ.

2.5 Bloch Sphere

To visualize the movement of spins, it is convenient to introduce the Bloch Sphere as depicted in Figure (2.2) [84]. In this Bloch sphere picture, a spin can be represented as a vector with the origin at the center of the sphere. As the spin moves, its vector tip traces a path along the surface of the Bloch sphere. To demonstrate the validity of Bloch sphere, let us consider an isolated spin at an arbitrary quantum state $|\psi\rangle$. This arbitrary state $|\psi\rangle$ can be represented as,

$$|\psi\rangle = \cos(\frac{\theta}{2})\,|\uparrow\rangle + e^{i\phi}\sin(\frac{\theta}{2})\,|\downarrow\rangle \tag{2.36}$$

where the coefficients are chosen to satisfy the normalization $\langle\psi|\psi\rangle = 1$. Knowing the representation of the quantum state, we may calculate the expectation value of

the spin angular moment $\vec{I}$. In the matrix representation,

$$I_x \doteq \begin{pmatrix} 0 & \frac{1}{2} \\ \frac{1}{2} & 0 \end{pmatrix}, \quad |\uparrow\rangle \doteq \begin{pmatrix} 1 \\ 0 \end{pmatrix}, \quad \text{and} \quad |\downarrow\rangle \doteq \begin{pmatrix} 0 \\ 1 \end{pmatrix} \tag{2.37}$$

Therefore,

$$\begin{aligned} \langle I_x \rangle &= \langle \psi | I_x | \psi \rangle \\ &= (\cos(\frac{\theta}{2}) \quad e^{-i\phi} \sin(\frac{\theta}{2})) \times \begin{pmatrix} 0 & \frac{1}{2} \\ \frac{1}{2} & 0 \end{pmatrix} \times \begin{pmatrix} \cos(\frac{\theta}{2}) \\ e^{i\phi} \sin(\frac{\theta}{2}) \end{pmatrix} \\ &= \frac{1}{2} \sin(\theta) \cos(\phi) \end{aligned}$$

Similarly, we can get

$$\begin{aligned} \langle I_y \rangle &= \langle \psi | I_y | \psi \rangle = \frac{1}{2} \sin(\theta) \sin(\phi) \\ \langle I_z \rangle &= \langle \psi | I_z | \psi \rangle = \frac{1}{2} \cos(\theta) \end{aligned}$$

Therefore, the expectation value of spin magnetic moment is,

$$\begin{aligned} \langle \vec{\mu} \rangle &= \gamma \hbar (\langle I_x \rangle \hat{x} + \langle I_y \rangle \hat{y} + \langle I_z \rangle \hat{z}) \\ &= \frac{1}{2} \gamma \hbar (\sin(\theta) \cos(\phi) \hat{x} + \sin(\theta) \sin(\phi) \hat{y} + \cos(\theta) \hat{z}) \end{aligned}$$

which demonstrates that a Bloch Sphere vector can be used to represent the expectation value of magnetic moment, hence the magnetization (which is the quantity of magnetic moment per unit volume).

2.6 T_1 and T_2 Processes

For a system of nuclear spins at equilibrium, the net magnetization lies along $\hat{z}$. This magnetization M_0 is referred to as the longitudinal magnetization at equilibrium,

$$M_0 = \frac{1}{2}\gamma\hbar(N_+ - N_-) \tag{2.38}$$

where N_+ (N_-) represents the number of spins that are spin-up (spin-down) or on the lower (higher) energy level assuming a positive γ. The distribution of N_+ and N_- can be approximated with Boltzmann statistics (Equation(2.28)). The net magnetization along $\hat{x}$ and $\hat{y}$ are called transverse magnetization and at equilibrium they are both zero.

A radio frequency (RF) pulse at Larmor frequency can be used to excite spins and rotate the net magnetization down to the transverse plane. Some time after this initial saturation, the spins will recover back to equilibrium. This spin-lattice relaxation process is often described by the equation

$$M_z(t) = M_0(1 - e^{-\frac{t}{T_1}}) \tag{2.39}$$

which is used to infer a value for T_1.

To understand T_1, recall that when a spin relaxes back to the lower energy level, it needs to give up its extra energy $\gamma\hbar H_0$. Unless there is a heat reservoir to accept this energy through some energy transfer pathway, this spin cannot relax back to the lower energy level. Thus the speed at which $M_z(t)$ returns to its equilibrium value depends on the mechanisms available to transfer the extra energy to something else,

such as translational movement of atoms, rotations of atoms, vibrations of atoms, etc. All these thermal energy reservoirs are collectively called the "lattice," which is the reason why T_1 is referred to as the spin-lattice relaxation time (or sometimes longitudinal relaxation time) [27, 84].

Now let us take a look at T_2, the spin-spin relaxation time or transverse relaxation time. When the net magnetization is brought from $\hat{z}$ direction to the transverse plane, spins start to precess about the $\hat{z}$ axis due to the external magnetic field along $\hat{z}$. Microscopically, spins in a sample may experience different local magnetic field as the result of H_0 inhomogeneity or some internal interactions. As a result, some spins precess faster than the Larmor frequency and some slower than the Larmor frequency. Therefore, as the spins precess in the transverse plane, the phase differences among spins will develop gradually. At some point, the phase differences are so big that the total transverse magnetization decays to zero. A curve fit of this decay (which is sometimes exponential or Gaussian depending on the decay mechanisms) is often used to infer T_2 (conventionally, the T_2 quantity measured in this way is called T_2^*. Please refer to Section 4.2 and Section 4.4 of Chapter 2 for more details) [27, 84].

Since the transverse magnetization will relax back to $\hat{z}$ as a result of the spin-lattice process, T_2 cannot exceed T_1. For solid samples, T_2 is usually much smaller than T_1 and effect of T_1 on T_2 can be ignored. For liquid samples, because the dipole-dipole interactions among nuclear spins are averaged out through the fast tumbling motion of the liquid molecules, T_2 can approach T_1 [84, 27].

Chapter 3

NMR Hardware

Ever since the discovery of NMR technique by the Nobel prize laureates Edward M. Purcell [74] and Felix Bloch [8, 9, 10], various NMR experiments have been designed to achieve different goals. Before we get into the actual experiments, let us first take a look at the NMR hardware that is needed to carry out accurate and high-resolution experiments. The book titled "Experimental Pulse NMR: a Nuts and Bolts Approach" by E. Fukushima and S. B. W. Roader provides an excellent reference book for the experimental details of NMR technique [27].

3.1 Superconducting Magnet

A strong and homogeneous external magnetic field is needed for high resolution NMR experiments. In most NMR experiments, we start with the initial equilibrium magnetization M_0 (strictly speaking, it is close to equilibrium since the equilibrium state takes an infinitely long time to reach), and the NMR signal is proportional to the magnitude of M_0. A large M_0 requires a strong magnetic field H_0. For a high resolution NMR signal, H_0 also has to be spatially homogeneous and stable in time.

Improving these characteristics of the external field enables the study of tiny local field variations due to intrinsic interactions in a sample.

Nowadays, superconducting magnets are typically used in NMR. They can produce stronger magnetic fields than ordinary iron-core electromagnets. Since no power is lost to ohmic resistance in the windings, superconducting magnets can be cheaper to operate. However, superconducting magnets require careful maintenance since they need to be kept below the critical temperature of the superconductive windings. Liquid helium is used as a coolant for most superconducting magnets. The magnet and coolant are contained in a thermally insulated container called a cryostat. Liquid helium in the cryostat will slowly burn off while maintaining a low temperature of 4.2 K. Since liquid nitrogen is much cheaper than liquid helium, an outer jacket containing liquid nitrogen at 77 K is often used to slow the boil-off rate of liquid helium in inner cryostat.

Another advantage of a superconducting magnet is that it can run in a persistent mode [27]. This persistent mode enables the field to remain constant to a higher precision than the stability of the power supply would allow. A superconducting switch attached to a small heater is used to achieve the persistent mode. As illustrated in Figure 3.1, a superconducting switch is in parallel with the superconducting solenoid that is used to produce a large magnetic field. First, the superconducting switch is heated to above its critical temperature to "open" the switch so that the superconducting solenoid can be energized by the power supply. After the current running

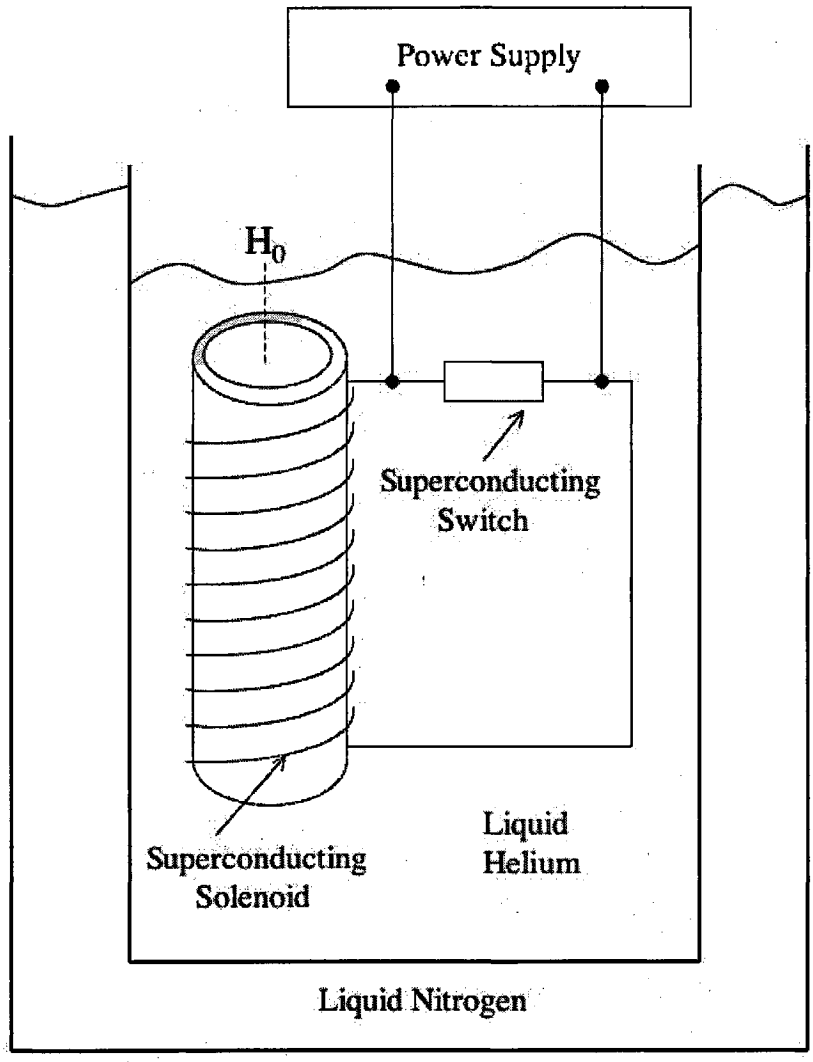

Figure 3.1: The superconducting solenoid is in parallel with a superconducting switch. The switch is first open to let the superconducting solenoid get energized to the desired field strength, and is then closed to reach the persistent mode.

Attribute	Value
Superconducting Material	Nb_3Sn wire
Maximum Central Field	12.0 Tesla
Field Stability	< 0.02 ppm/hr
Operating Current	109.4 Amps at 12 Tesla
Stored Energy	1.02 MegaJoules
Field Homogeneity	< 0.2 ppm
High Homogeneity Volume	10 mm diameter sphere
Bore Diameter	88 mm
Helium Reservoir Volume	35 liters
Helium Boil-off Rate	< 0.019 liters/hr
Total Weight	400 kg

Table 3.1: Oxford Instruments Teslatron Superconducting NMR Magnet.

in the solenoid achieved the desired value, hence the desired magnetic field strength, the switch is "closed" by turning off the heater and cooling the switch into the superconducting state. The current from the power supply can now be ramped down, and the current across the closed switch ramps up to match the current across the solenoid. The power supply can then be disconnected. The current running in the superconducting circuit will not persist forever because of a small residual resistance due to joints or a phenomenon called flux motion resistance. However, the down-drift of the magnetic field in the persistent mode is very slow for our magnet.

Most of the experiments described in this thesis were performed on our Oxford Instruments Teslatron superconducting magnet. The attributes of this magnet are listed in Table 3.1. Most experiments were carried out at 12 Tesla, with the inhomogeneity less than one part per million (ppm) at the center of the magnet across the volume of ~ 1 cm^3 and the field drift of less than 0.02 ppm per hour.

To achieve the high field homogeneity at the center of the superconducting magnet Teslatron, a process called "shimming" is performed using the pre-installed superconducting shim coils. The purpose of the shimming process is to adjust the fields generated by shim (field gradient) coils so that they can cancel the field gradients generated by the big superconducting solenoid. In our magnet, the following field gradients are considered and taken care of, $\frac{\partial}{\partial z}$, $\frac{\partial^2}{\partial z^2}$, $\frac{\partial}{\partial x}$, $\frac{\partial}{\partial y}$, $\frac{\partial^2}{\partial x \partial y}$, $\frac{\partial^2}{\partial x^2}$, and $\frac{\partial^2}{\partial y^2}$. To do a shimming, we first conduct a spatial mapping near the center of the magnetic field using a small deuterium sample of the size of ~ 1 mm^3. Then we calibrate the six superconducting shim coils by measuring the fields they generate with a certain current value. Finally we calculate and apply the appropriate current value for each coil so that the total field is close to a constant (variation < 0.2 ppm) across the volume of ~ 1 cm^3. Sometimes the above three steps are repeated again to achieve even better homogeneity.

3.2 Sample Probe

The sample probe is a crucial part of the experimental setup. It holds the sample in the strong magnetic field, transmits RF pulses into the sample, and detects the signal from the sample. Some sample probes may have special features such as a sample spinner to do Magic Angle Spinning [84], temperature controlling circuitry to heat the sample, or gradient coils to produce a gradient in H_0 field. For most of the experiments reported in this thesis, they were carried out in a single channel sample

probe which contains a resonant circuit enclosed inside a copper can.

The sample of interest is placed in a small copper coil, which is part of a resonant circuit. The probe is inserted into the superconducting magnet in such a way that the sample should stay in the most homogeneous area of the magnet, or the center of the magnet. Depending on the resonance frequency, we pick one of the two tank circuits shown in Figure 3.2. For a frequency below 100 MHz, we typically use the series-parallel circuit, where a matching capacitor C_m is in series with a tuning capacitor C_t and the tuning capacitor is in parallel with the sample coil. For a frequency equal to or greater than 100 MHz, the parallel-series circuit is often used, where C_m and C_t are in parallel and C_t is in series with a sample coil. In both designs, the circuit is connected to a 50Ω coaxial line; C_m and C_t are tunable capacitors in the range of 2-25 pico-farad (pF); L is the inductance of the copper coil ($\sim$ 4-15 turns) with the typical range of 10 $\sim$ 100 micro-Henries; r is the effective resistance in the circuit, which is in the order of a few Ohms. Note that the sample under study is inserted into the copper coil.

In practice, 100 MHz is not a clear-cut line to decide which circuit to choose. For frequency not too far away from 100 MHz, the circuit design is chosen by trial and error. Very often extra fixed capacitors (1-100 pF) need to be added in parallel or in series with C_m and C_t, to simultaneously tune the circuit at a target frequency ω_0 and match it to 50Ω coaxial line impedance. The values of the tuning and matching

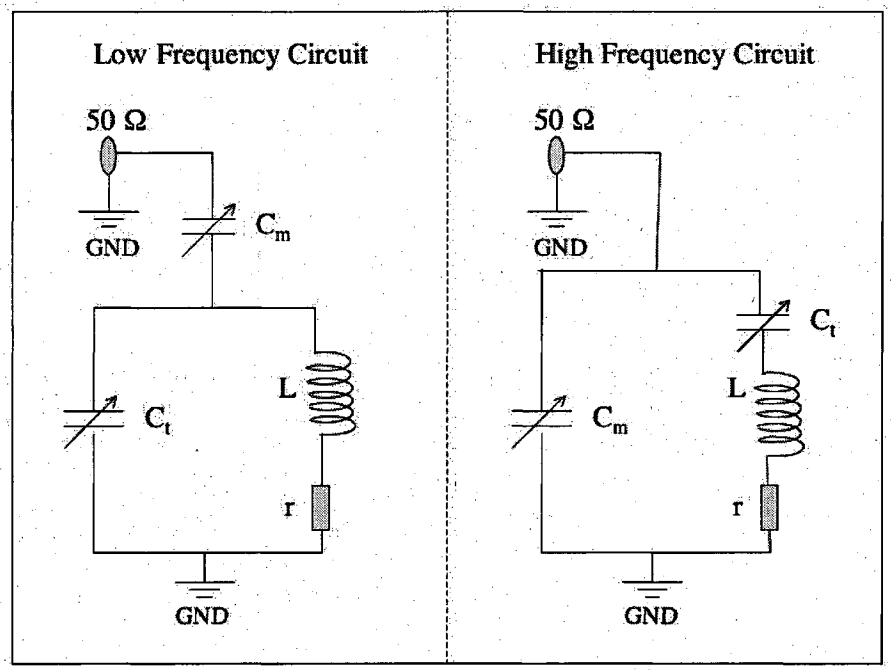

Figure 3.2: Low frequency resonance circuit (series-parallel) for f <100 MHz and high frequency resonance circuit (parallel-series) for f ≥100 MHz.

capacitances can be calculated using the following formula,

$$\text{Low frequency circuit:} \quad C_t = \frac{L\omega - \sqrt{r/50\Omega}\sqrt{r^2 - (50\Omega)r + L^2\omega^2}}{\omega(r^2 + L^2\omega^2)}$$
$$C_m = \frac{\sqrt{r/50\Omega}}{\omega\sqrt{r^2 - (50\Omega)r + L^2\omega^2}} \tag{3.1}$$

$$\text{High frequency circuit:} \quad C_t = \frac{L\omega + \sqrt{(50\Omega - r)r}}{\omega(r^2 - (50\Omega)r + L^2\omega^2)}$$
$$C_m = \frac{1 - r/50\Omega}{\omega\sqrt{(50\Omega - r)r}} \tag{3.2}$$

In practice, the values of tuning and matching capacitances are found by trial and error. While soldering the tank circuit, precautions need to be taken to avoid sharp spikes in the connecting points since these pointy spikes could lead to "arcing," which

tends to limit the maximum pulse strength H_1.

In the above two resonance circuits, the copper-wire sample coil serves two functions. First, this solenoid coil creates the H_1 field to rotate the net magnetization in pulsed NMR experiments. Second, this coil also detects the precession of the transverse magnetization as it induces a voltage across the coil.

3.3 Pulse NMR Spectrometer

Most of the experiments in this thesis were carried out using a commercial pulse NMR spectrometer called the Apollo, made by Tecmag. The Apollo is mainly composed two parts, the RF transmitter and the receiver.

RF Transmitter

For pulse NMR spectroscopy, the RF wave needs to be modulated into pulses of desired durations and often the pulses need to be phase coherent. The common scheme of a phase coherent RF transmitter consists a RF frequency synthesizer, a pulse generator, and an amplifier [27]. The RF frequency synthesizer produces a continuous RF wave at low power, and the pulse generator modulates the continuous RF wave to desired duration or shape. Then the pulse is fed into a amplifier to achieve desired level. Since the Apollo uses Direct Digital Synthesizer (DDS), the pulse amplitude, pulse duration, pulse phase, and pulse shape can be controlled with high precision. The Apollo can provide phase-coherent pulses over a relatively long time, but its slow phase drifting does present a problem in the experiments with an

anomalously large number of pulses over a time as long as tens of seconds, as discussed in Chapter 9.

Moreover, the DDS of the Apollo can make coherent frequency jumps in the transmitter and receiver, which allows us to do certain special experiments with frequency hopping as described in Chapter 8 and Chapter 9.

Quadrature Receiver

NMR receivers usually have three stages [27], a pre-amplifier to make the signal from the RF coil larger, followed by a quadrature detector to remove the RF carrier and separate out the M_x and M_y signals, and then another amplifier to further boost the signals. One of the two signals (M_x and M_y) is assigned to be "real" and the other to be "imaginary." The Apollo has a digital receiver and the pre-amplifier is not integrated into the receiver section to allow more flexibility for the user. In practice, a pre-amplifier of 32.5 dB or 60 dB was used depending on the size of the signal.

A key part of a quadrature detector is a device called Double Balanced Mixer (DBM) [27], which can produce the sum and the difference of the two input frequencies. For example, if the two input signals have frequencies A and B, the output will have frequencies A+B and A-B. Therefore, when the NMR signal at frequency $\omega = \omega_0 + \omega'$ is mixed again with the ω_0 reference wave of the pulses, the output will have the frequencies ω' and $2\omega_0 + \omega'$. In practice, since $\omega_0 \gg \omega'$, frequency ω' can be singled out by feeding the output of DBM to a low-pass filter. Figure 3.3 shows a

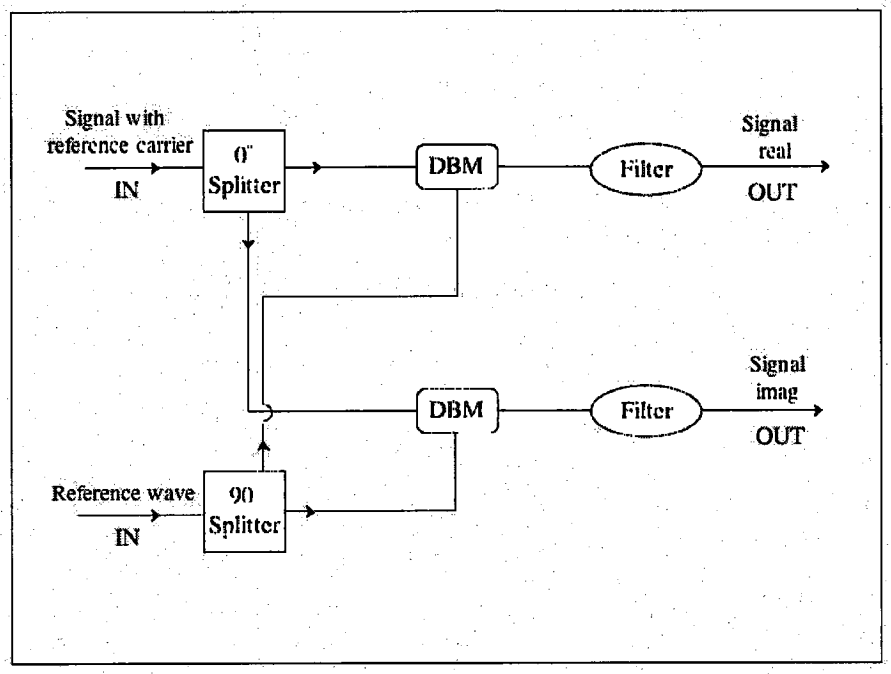

Figure 3.3: A schematic of a typical quadrature detector.

schematic of a typical quadrature detector, which contains two splitters (0° and 90°), two DBMs, two filters and two amplifiers.

Chapter 4

Unexpected Spin Echoes in Dipolar Solids

NMR has powerful applications in many areas. In recent years, it has also been used to identify physical systems with long decoherence times that may be useful for quantum computation [52]. Many suggestions have been made to implement quantum computation with nuclear or electron spins [15, 20, 21]. Motivated by proposals to use nuclear spins in semiconductors for quantum computation [40, 41, 43, 72, 89], we set out to measure the spin-spin relaxation time T_2 for ^{31}P and ^{29}Si in Silicon doped with Phosphorous [4, 28, 83, 85]. During our measurements, we encountered a few surprising experimental results [17, 48]. The surprises we observed are presented in this Chapter, together with an introduction to a few most fundamental NMR pulse sequences as the background to understand why we called those results "surprising." Note that we only discuss pulse NMR and all the pulses are applied in the X-Y plane. To understand how these fundamental pulse sequences work, we will first use the conventional δ-pulse approximation, i.e. the pulses do nothing other than

rotating the spins by a desired angle, since the pulses applied in these experiments are very strong. However, as we will show over the next few Chapters, the δ-pulse approximation can break down when many strong180° or π pulses are applied in a phase-coherent way.

4.1 The δ-Pulse Approximation

4.1.1 The Internal Hamiltonian

With no external pulses applied, the spin system has an internal Hamiltonian that may include many interactions. For the spin-$\frac{1}{2}$ solid samples (we typically assume that there is only a single type of spin in the sample unless otherwise noted) we investigated in this thesis, we only include the following relevant terms: the Zeeman interaction, the nuclear dipolar interaction, and the chemical shift [19, 30, 70, 71, 73].

As we introduced in Chapter 2, nuclear magnetic moment is coupled to an external magnetic field in the form of $-\gamma\hbar H_0 I_z$, assuming $\vec{H}_0 = H_0\hat{z}$. In reality, no matter how good a superconducting magnet is, there is some degree of field inhomogeneity ΔH_0. Therefore, generally we write this Zeeman interaction Hamiltonian of a N-spin system in the Lab frame as,

$$\mathcal{H}^{Lab} = \sum_{i=1}^{N} -\gamma\hbar(H_0 + \Delta H_{0_i})I_{z_i} \tag{4.1}$$

Next we will consider the direct dipolar coupling between two magnetic moments $\vec{\mu}_1$ and $\vec{\mu}_2$. The well-known classical interaction energy E is [38],

$$E = \frac{\vec{\mu}_1 \cdot \vec{\mu}_2}{r^3} - \frac{3(\vec{\mu}_1 \cdot \vec{r})(\vec{\mu}_2 \cdot \vec{r})}{r^5} \tag{4.2}$$

where $\vec{r}$ is the vector from $\vec{\mu}_1$ to $\vec{\mu}_2$. For the quantum description, we can simply substitute $\vec{\mu}_1$ by $\gamma\hbar\vec{I}_1$ and $\vec{\mu}_2$ by $\gamma\hbar\vec{I}_2$ (assuming they are the same type of spin),

$$\mathcal{H}_d = \gamma^2\hbar^2\left[\frac{\vec{I}_1\cdot\vec{I}_2}{r^3} - \frac{3(\vec{I}_1\cdot\vec{r})(\vec{I}_2\cdot\vec{r})}{r^5}\right] \tag{4.3}$$

We can rewrite the above equation using the rising and lowering operators $I_\pm$ [81], then regroup the terms according to the quantum order of the operators. Following the notation of C. P. Slichter [84], the direct dipolar coupling can be written as

$$\mathcal{H}_d = \frac{\gamma^2\hbar^2}{r^3}(A+B+C+D+E+F) \tag{4.4}$$

where

$$\begin{aligned}
A &= I_{1_z}I_{2_z}(1-3\cos^2\theta)\\
B &= -\frac{1}{4}(I_1^+I_2^- + I_1^-I_2^+)(1-3\cos^2\theta)\\
C &= -\frac{3}{2}(I_1^+I_{2_z} + I_{1z}I_2^+)\sin\theta\cos\theta e^{-i\phi}\\
D &= -\frac{3}{2}(I_1^-I_{2_z} + I_{1_z}I_2^-)\sin\theta\cos\theta e^{i\phi}\\
E &= -\frac{3}{4}I_1^+I_2^+\sin^2\theta e^{-2i\phi}\\
F &= -\frac{3}{4}I_1^-I_2^-\sin^2\theta e^{2i\phi}
\end{aligned} \tag{4.5}$$

and $\vec{r} = (r\sin\theta\cos\phi, r\sin\theta\sin\phi, r\cos\theta)$. While terms A and B connect degenerate states, terms C and D connect states with energy difference of $\hbar\omega_0$, and terms E and F connects states with energy difference of $2\hbar\omega_0$ [84], where $\omega_0 = \gamma H_0$ is the Larmor frequency. We use a big external magnetic field (normally 12 Testa) and ω_0 is typically in the order of 100 Mhz, which is greatly bigger than a typical dipolar

coupling strength (normally in the order of or less than a few kHz). The total effects of term C, D, E, and F are very small compared to A and B, so keeping only A+B is an excellent high-field approximation [60, 84]. The dipolar term A+B is called the secular dipolar coupling. From now on, we will use this secular dipolar coupling only and call it $\mathcal{H}_{zz}$ by convention. For a system of N spins,

$$\mathcal{H}_{zz} = \sum_{j>i}^{N} B_{ij}\{3I_{z_i}I_{z_j} - \vec{I}_i \cdot \vec{I}_j\} \tag{4.6}$$

where

$$B_{ij} = \frac{1}{2}\frac{\gamma^2\hbar^2}{r_{ij}^3}(1 - 3\cos^2\theta_{ij}) \tag{4.7}$$

The next important Hamiltonian term we will consider is chemical shift term, which arises from the orbital susceptibility of electrons. When a solid is placed in an external magnetic field, the bonding electrons will develop a slight preference for orbiting in the sense favored by the applied magnetic field. Just like a current loop, this imbalance in orbiting electrons produces a magnetic field ΔH_c at the location of the nuclear spin. Therefore, the magnetic resonance frequency of the nuclear spin is $\omega = \gamma(H_0 + \Delta H_c)$ and the change in frequency $\Delta\omega = \gamma\Delta H_c$ is called chemical shift. Because the electron density around each nuclear spin may vary according to the type of nuclei and chemical bonds in the molecule, the value of $\Delta\omega$ varies for nonequivalent nuclear spins.

Combining all the above three interactions, we write the general Hamiltonian of

a N-spin system in the Lab frame as,

$$\mathcal{H}^{Lab} = \sum_{i=1}^{N} -\gamma\hbar(H_0 + \Delta H_{0_i} + \Delta H_{c_i})I_{z_i} + \mathcal{H}_{zz} \tag{4.8}$$

Adding ΔH_{0_i} and ΔH_{c_i} together as ΔH_i^{Loc} and going to the rotating frame of frequency $-\gamma\vec{H}_0$, we can rewrite Equation (4.8) as,

$$\mathcal{H}_{int} = \sum_{i=1}^{N} \Omega_{z_i} I_{z_i} + \mathcal{H}_{zz} = \mathcal{H}_Z + \mathcal{H}_{zz} \tag{4.9}$$

where $\Omega_{z_i} = -\gamma\hbar\Delta H_i^{Loc}$, which varies from spin to spin or spin cluster to spin cluster in a macroscopic sample. We use the subscribe "int" in $\mathcal{H}_{int}$ to indicate that it is the internal Hamiltonian of the spin system, i.e., without any external pulses applied. We will refer $\mathcal{H}_Z$ as the the Zeeman Hamiltonian and $\mathcal{H}_{zz}$ the dipolar Hamiltonian.

4.1.2 The δ-Pulse Approximation

With an external pulse in ϕ direction, the total Hamiltonian (always in the rotating frame unless noted otherwise) is the sum of the internal Hamiltonian $\mathcal{H}_{int}$ (Equation (4.9)) and the external pulse Hamiltonian $\mathcal{H}_p$,

$$\mathcal{H}_{tot} = \mathcal{H}_{int} + \mathcal{H}_p = \mathcal{H}_{int} - \hbar\omega_1 I_{\phi_T} \tag{4.10}$$

where a uniform pulse of strength $\omega_1 = \gamma H_1$ is assumed and $I_{\phi_T} = \sum_{i=1}^{N} I_{\phi_i}$ with $\phi = x, y$. The pulse duration t_p is used to control the rotation angle. For example, a 90° pulse is achieved by setting $\omega_1 t_p = \frac{\pi}{2}$. When the pulse is so strong that $\mathcal{H}_p \gg \mathcal{H}_{int}$, or say it in another way, when the pulse strength $\omega_1/2\pi$ is much bigger than the spectral linewidth, by conventional NMR theory we can make the δ-pulse approximation [1, 26, 34, 60, 84] and ignore the effect of $\mathcal{H}_{int}$ during the short pulse .

Now we will use the δ-pulse approximation to get an idea how the following basic NMR pulse sequences work.

4.2 Free Induction Decay

The simplest NMR pulse experiment is the Free Induction Decay (FID) [1, 23, 84], which is just a single 90° pulse followed by data acquisition. As described in the introduction of T_2 in Chapter 2, the equilibrium magnetization is brought to the transverse plane by a 90° pulse and the spins start to precess around the Z-axis in the transverse plane due to the magnetic field along $\hat{z}$. Because of variations in the local field, some spins will precess faster than the Lamor frequency ω_0 and some slower than ω_0, which causes the spin isochromats (a spin isochromat refers to spins that share the same precession frequency [84]) to get out of phase from each other, resulting a decayed transverse magnetization. Both the Zeeman term and the dipolar term contribute to the FID decay and the decay constant derived from an FID is by convention called T_2^* instead of T_2 [27, 84]. As we will see later that some pulse sequences can refocus the decay caused by ΔH_i^{Loc} to measure the decay constant of T_2, which is longer than T_2^*.

When Fourier transformation [7] is applied to an FID, we get the FID spectrum, as illustrated in Figure 4.1. Note that the Full Width at Half Maximum (FWHM) of the spectrum contains both the Zeeman linewidth and the dipolar linewidth. A narrow spectrum corresponds to a slow decay or a long T_2^*, and vice versa.

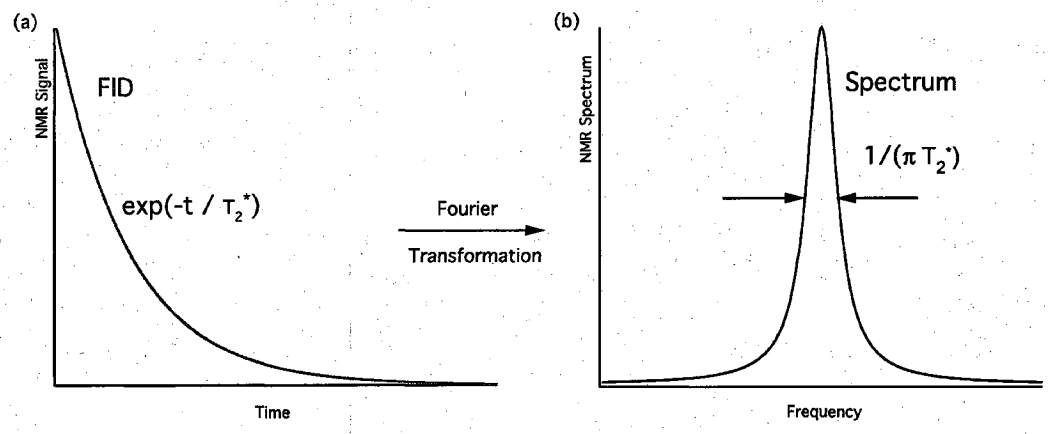

Figure 4.1: Demonstration of a simple exponential-decay FID with decay constant T_2^* (a) and its spectrum (b). Note that the Fourier transformation of this FID is a Lorentizan function, with FWHM of $1/\pi T_2^*$

4.3 Measurement of T_1

The spin-lattice relaxation time T_1 can be measured through two popular ways: saturation recovery, and inversion recovery [27]. Both methods include a preparation pulse (or pulses), a recovery delay, and a measurement pulse.

Saturation recovery method contains a 90° pulse, followed by a delay τ, then another 90° pulse: $90° - \tau - 90°$. The function of the first 90° pulse is to saturate the magnetization, i.e. to make the magnetization along $\hat{z}$ zero. During the τ delay time, the magnetization relaxes back toward equilibrium, forming $M_z(\tau)$ as a function of delay τ. $M_z(\tau)$ is brought to the transverse plane by the second 90° pulse, resulting a FID whose magnitude is proportional to $M_z(\tau)$. The expression of $M_z(\tau)$ is [27]

$$M_z(\tau) = M_0(1 - e^{-\frac{\tau}{T_1}}) \tag{4.11}$$

The inversion recovery method uses a 180° pulse instead as the first pulse : $180° -$

$\tau - 90°$. Assuming the spin system starts from equilibrium, the net magnetization M_0 is inverted from $+\hat{z}$ to $-\hat{z}$ by the first 180° pulse. The recovery during the delay τ goes from $-M_0$ to $+M_0$ [27],

$$M_z(\tau) = M_0(1 - 2e^{-\frac{\tau}{T_1}}) \tag{4.12}$$

Figure 4.2 shows the recovery curve for each method. Since for the inversion recovery

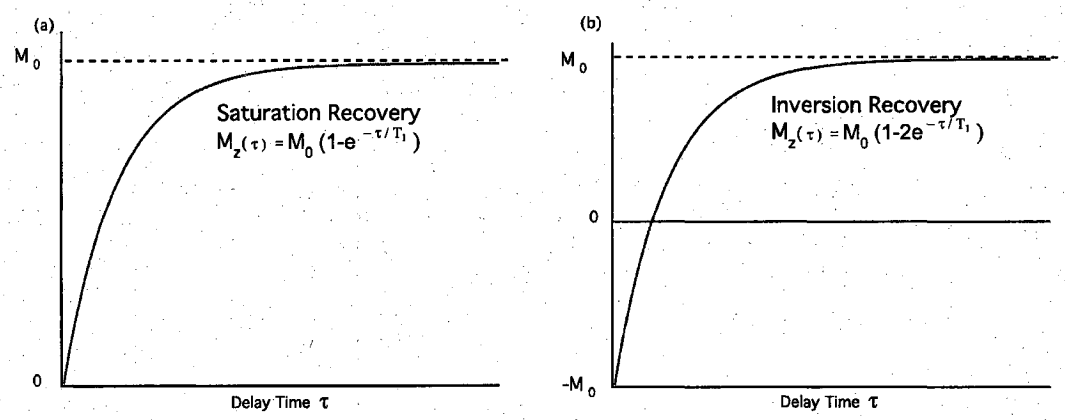

Figure 4.2: Spin-lattice relaxation curve based on two measurement methods, saturation recovery (a) and inversion recovery (b).

method, the spins need to start from equilibrium to give an accurate measurement, a waiting time that is much longer than T_1 must be implemented before the inversion pulse. For samples that have a long T_1, this can be very time-consuming. On the other hand, for the saturation recovery method, as long as the net magnetization along the Z-axis is zero after the saturation, the measurement should be all right. Between two measurements, whether the second is a repeating scan with the same τ or a scan with a different τ, when the delay between the measurement 90° of the first scan and the

saturation 90° of the second scan is much bigger than T_2, the magnetization will be completely dephased and the net magnetization along Z-axis should be zero after the saturation 90° pulse. For our solid samples with T_2 in the order of millisecond, the acquisition window after the measurement 90° pulse usually lasts longer than T_2, so we do not need to implement a delay before the saturation pulse of next scan. In practice, to ensure complete saturation, we usually substitute the first 90° pulse with a so-called saturation train, $(90° - \tau_0)^n$, where τ_0 is a delay time that is bigger than T_2 and n is the number of repetition, usually ~ 100.

After T_1 is measured, we implement a delay of $\sim 5 \times T_1$ in the beginning of any pulse sequence to wait for the spin system to get close to equilibrium before any excitation is applied. If however, the first scan is done after the sample has been sitting in the magnet for overnight, then the first scan is not the same as the second scan, since the waiting time of the first scan is actually overnight plus this $\sim 5 \times T_1$. This longer waiting time means we are starting closer to the equilibrium state, which also means a bigger signal after excitation. This is why we discard the first scan if we want to compare the signal quantitatively. Sometimes, we also implement a saturation train in the beginning of a pulse sequence, followed by a fixed recovery delay time of $\sim 5 \times T_1$. This way, each scan will start from the same initial magnetization.

4.4 Measurement of T_2

4.4.1 Two Pulse Sequence: Hahn Echo Experiment

Part of the magnetization decay observed in an FID arises from the Zeeman term in Equation (4.9). The discovery of the famous Hahn Echo [36, 84] (or Spin Echo) showed that the Zeeman decay could be refocused.

Let us now look at how Hahn Echo (HE) sequence works using the δ-pulse approximation. HE : $90_X - \tau - 180_Y - \tau - Echo$, where 90_X represents a 90° pulse along the X direction, 180_Y is a 180° pulse along the Y direction, and τ is a free evolution delay time. For simplicity we will consider the Zeeman term only. The first 90_X pulse brings the net magnetization from the Z-axis to the Y-axis. Then the transverse magnetization will decay due to the spread of Ω_{z_i} in $\mathcal{H}_Z$, forming an FID. When a 180° pulse is applied after a free evolution time τ, I_z is flipped to $-I_z$, inverting $\mathcal{H}_Z$ to $-\mathcal{H}_Z$. Therefore, the dephasing during the first τ period is followed by the rephasing during the second τ period, forming an echo as demonstrated in Figure 4.3.

How about $\mathcal{H}_{zz}$? Since it also contributes to FID, can it be refocused in HE experiment? $\mathcal{H}_{zz}$ has only bilinear spin operators like $I_{z_i}I_{z_j}$, when both I_{z_i} and I_{z_j} are inverted by a π pulse, $\mathcal{H}_{zz}$ will stay the same. Therefore, the dephasing caused by $\mathcal{H}_{zz}$ during the first delay τ will continue to accumulate after the π pulse. This fact is commonly described as "a π pulse does not refocus the decay caused by homonuclear dipolar coupling." Therefore, the echo acquired at 2τ after the tipping 90° pulse will be smaller than the FID. As τ is gradually increased, a series of Hahn echo

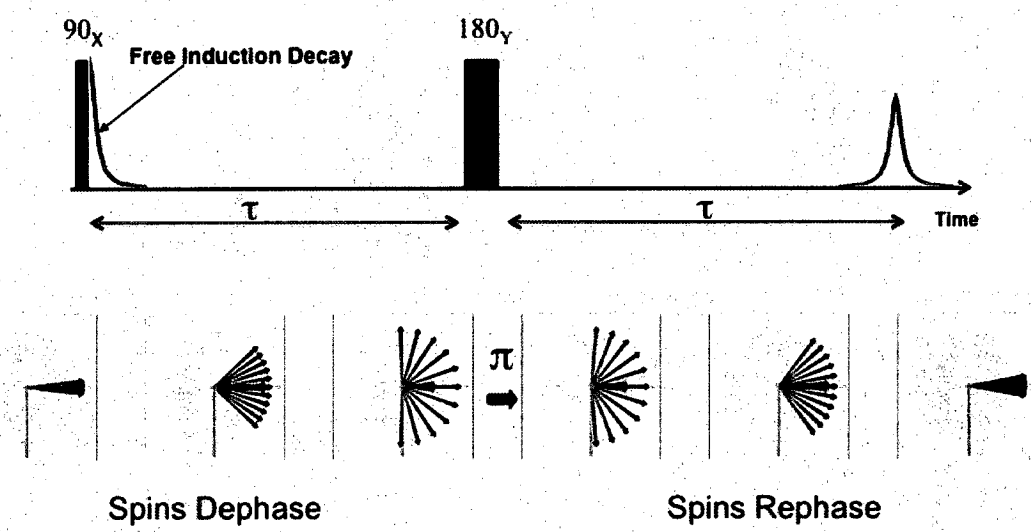

Figure 4.3: The demonstration of HE with the Bloch sphere. Spins precess at different rates in the X-Y plane due to their different local field. Red arrows represent spins with a positive Zeeman shift ($\Omega_z > 0$), blue arrows represents spins with a negative Zeeman shift ($\Omega_z < 0$), and black arrows represent spins on resonance. After the first tipping pulse 90_X, spins start from the Y-axis and fan out in the X-Y plane, forming an FID. After the π pulse (180_Y), spins are moving back toward the Y-axis, forming an echo.

experiments can be performed to obtain a set of gradually decaying echoes. If the peak of each echo is plotted vs decay time (2τ), we will get a decay curve which allows us to derive T_2 as illustrated in Figure 4.4 (a). Note that the statement that the homonuclear dipolar decay cannot be refocused by a π pulse does not mean that it cannot be reversed or avoided. In fact, many techniques have been designed to refocus dipolar dephasing, such as magic echoes [42, 77, 79], or to average out the dipolar coupling using magic angle spinning [5, 6, 31, 32, 50] or pulse sequences [34, 55, 76]. Furthermore, a new dipolar decoupling sequence based on π pulses will be demonstrated and discussed in Chapter 9 of this thesis.

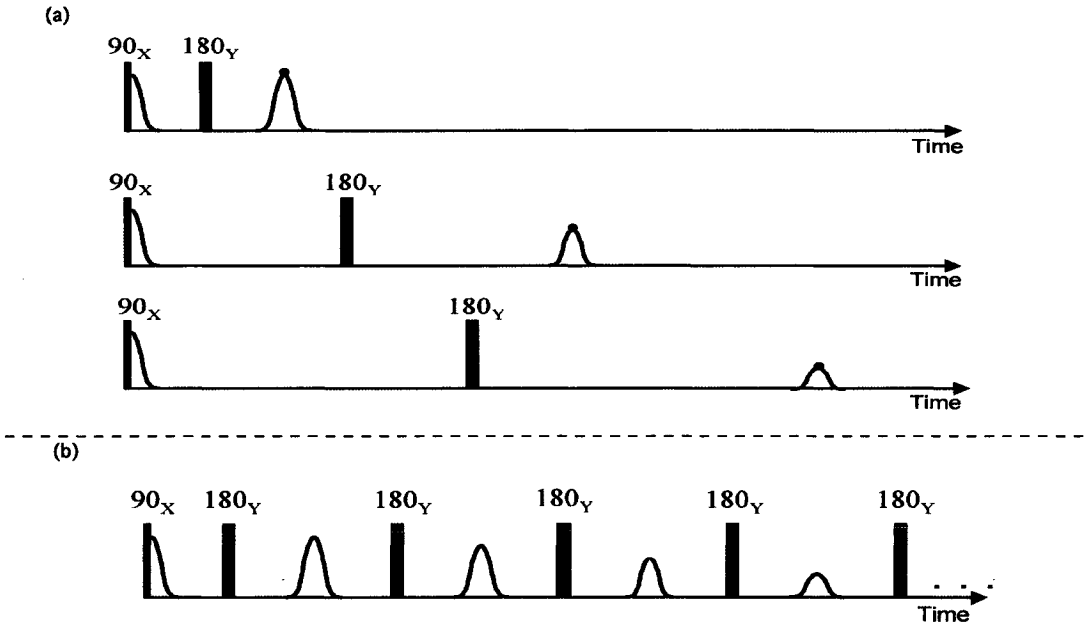

Figure 4.4: Demonstration of T_2 measurement using HE (a) and CPMG (b). Based on the δ-pulse approximation, the CPMG echo train should decay just like those Hahn echoes.

4.4.2 Multiple Pulse Sequence: CMPG Experiment

Doing a series of HE experiments does not seem to be the most efficient way to measure T_2. A multiple-pulse sequence can achieve a T_2 measurement in a single shot. One such sequence is Carr-Purcell-Meiboom-Gill (CPMG) [13, 62, 84]: $90_X - \tau - \{180_Y - 2\tau - 180_Y - 2\tau\}^n$, where n is the number of repetitions of the block in "{}". Since each π pulse will flip the sign of the Zeeman term, the 2τ free evolution periods will alternate between $\mathcal{H}_z$ and -$\mathcal{H}_z$ during the whole CPMG experiment. Therefore, the effect of the Zeeman term will be canceled out, and each echo acquired in the middle of two π pulses will decay due to $\mathcal{H}_{zz}$, as illustrated by Figure 4.4 (b).

4.5 Our Puzzle

Within the δ-pulse approximation, both the Hahn echo experiment and CMPG experiment should measure the same T_2 caused by $\mathcal{H}_{zz}$. However, in experiments we observed a discrepancy between these two methods when measuring the T_2 of ^{29}Si in a power sample of Silicon doped with Phosphorous (Si:P $10^{19}/\text{cm}^3$), as shown in Figure 4.5. Each green dot is the echo peak of a HE measured in a separate experiment with a certain τ value, and the red trace is from a single CPMG experiment. The HE data decay to zero after about 2 miliseconds. However, the CPMG trace seems to refuse to decay after reaching a certain echo height, forming a long-lived echo tail. This was puzzling: why did these two experiments fail to agree with each other as predicated by the δ-pulse approximation?

Furthermore, a long echo tail was not the only result of our multiple π pulse experiments. Since we are free to choose the phase of π pulses, we can define and compare the following pulse sequences [13, 62],

$$\begin{aligned}
\text{CP} &: 90_X - \tau - \{180_X - 2\tau - 180_X - 2\tau\}^n \\
\text{APCP} &: 90_X - \tau - \{180_{-X} - 2\tau - 180_X - 2\tau\}^n \\
\text{CPMG} &: 90_X - \tau - \{180_Y - 2\tau - 180_Y - 2\tau\}^n \\
\text{APCPMG} &: 90_X - \tau - \{180_{-Y} - 2\tau - 180_Y - 2\tau\}^n
\end{aligned}$$

where "AP" stands for "Phase Alternating." Within the δ-pulse approximation, each

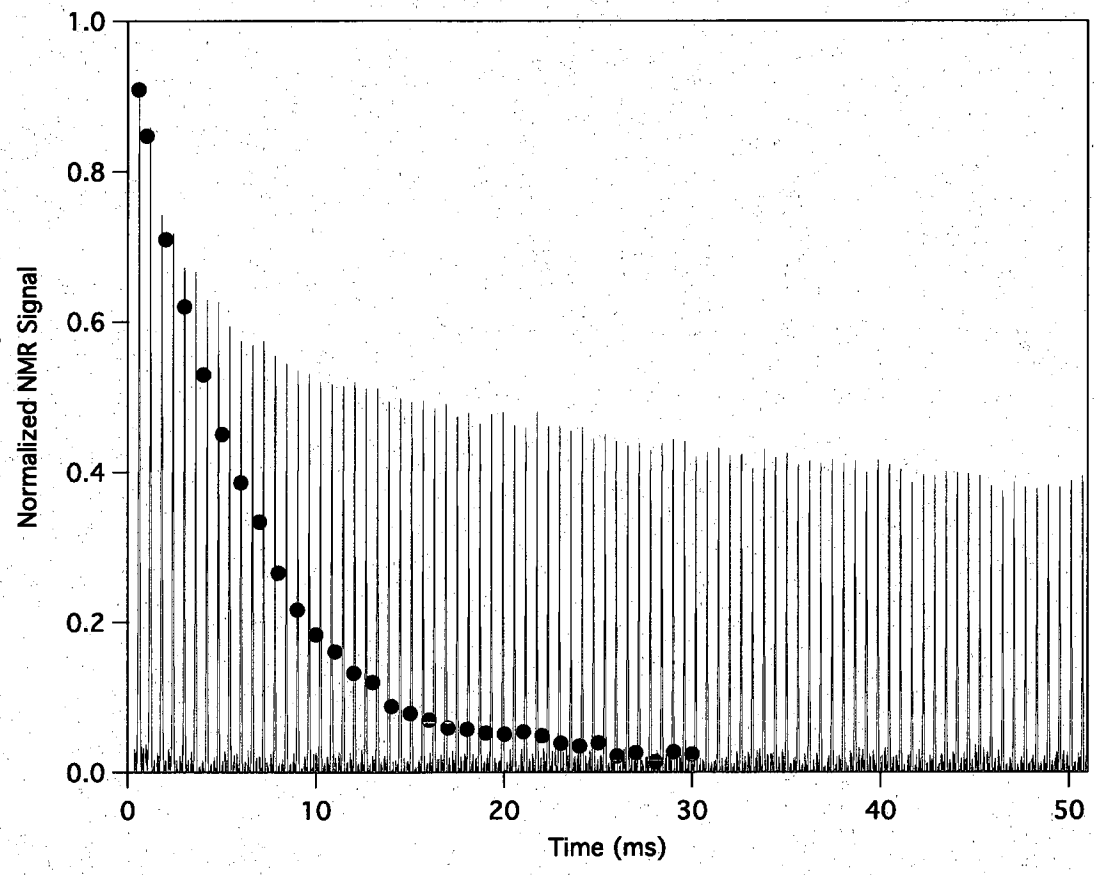

Figure 4.5: Sample: ^{29}Si in a crushed powder of Silicon doped with Phosphorous (Si:P 3.94×10^{19} P/cm^3). Comparison of T_2 measurement by HE (green dots) and CPMG (red trace). Each HE was obtained by an experiment with a single π pulse. The CPMG echo train was generated with multiple π pulses spaced with 2τ=592 μs. Normalization is set by the initial magnetization after the 90_X tipping pulse. Data taken at room temperature in a 12 Tesla field.

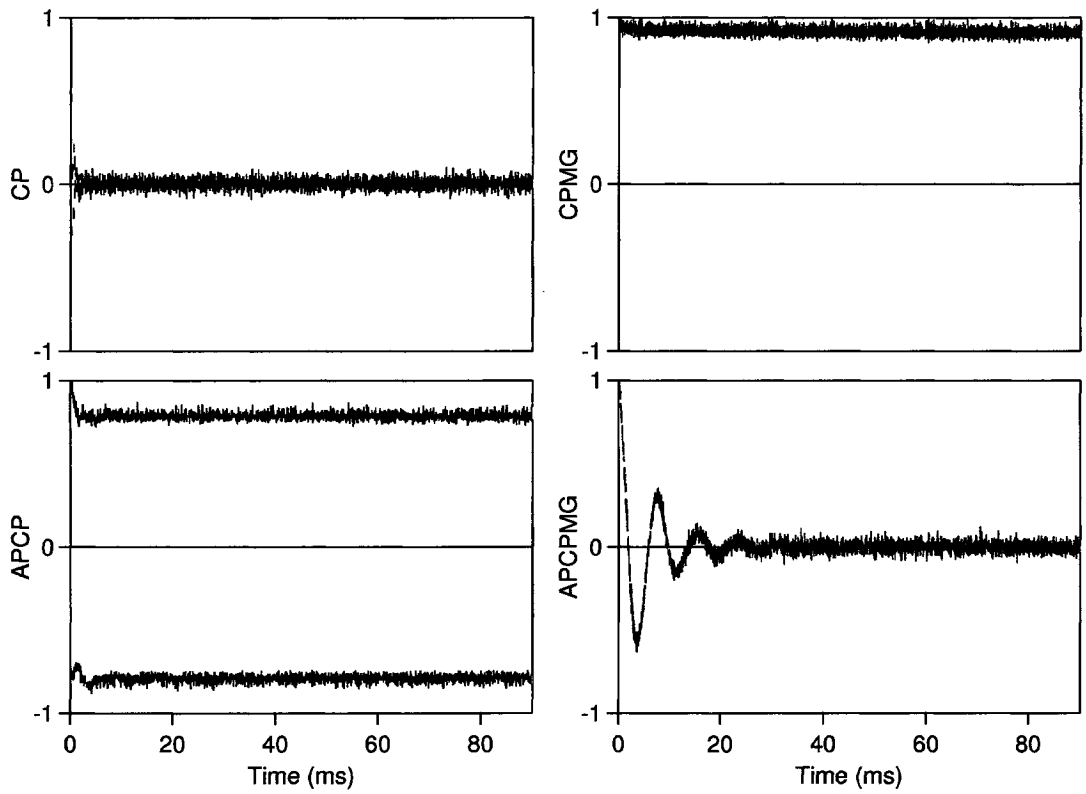

Figure 4.6: Sample: ^{29}Si in a crushed powder of Silicon doped with Antimony (Si:Sb 10^{17} Sb/cm^3). Four pulse sequences with π pulses of different phases applied (Top Left) CP, (Top Right) CPMG, (Bottom Left) APCP, (Bottom Right) APCPMG. 2τ=72 μs, and data taken at room temperature in a 11.74 Tesla field.

π pulse should do the same thing: flipping the sign of $\mathcal{H}_Z$ and leaving $\mathcal{H}_{zz}$ alone, no matter what the pulse phase is. However, our experiments gave us quite dramatic results as shown in Figure 4.6. CPMG and APCP give a long-lived echo tail, while CP and APCPMG decay quickly to zero. We refer to this phenomenon as Pulse Sequence Sensitivity (PSS) in this thesis.

Our efforts trying to solve this puzzle are presented over the next few Chapters, and solving this puzzle led to the design of the new pulse sequences discussed in Chapter 8 and Chapter 9.

4.6 Density Matrix and Time Evolution Operators

To facilitate the discussions in the next few Chapters, we will introduce the notation of density matrix and time evolution operators. From quantum mechanics [81], we know that the expectation value of an operator A can be calculated using the density matrix ρ.

$$\langle A \rangle = Tr\{A\rho\} \tag{4.13}$$

and the density matrix is defined as [81],

$$\rho = \sum_{i=1}^{N}\sum_{j=1}^{N} a_{ij}|\psi_i\rangle\langle\psi_j| \tag{4.14}$$

where $|\psi_i\rangle$ (i=1,2,$\cdots$ N) represents a complete set of orthonormal wave functions. a_{ij} is a complex weight number and will be i^{th} role and j^{th} column of the matrix representation of ρ.

The density matrix ρ evolves according to the Liouville's theorem [81],

$$i\hbar\frac{d}{dt}\rho(t) = [\mathcal{H}, \rho(t)] \tag{4.15}$$

where $\mathcal{H}$ is the Hamiltonian of the system and the brackets denote the quantum mechanical commutator [81]. For a constant $\mathcal{H}$, the solution of Equation (4.15) is

$$\rho(t) = \mathcal{U}\rho(0)\mathcal{U}^{-1} = \mathrm{e}^{-\frac{i}{\hbar}\mathcal{H}t}\rho(0)\mathrm{e}^{+\frac{i}{\hbar}\mathcal{H}t} \tag{4.16}$$

Where $\mathcal{U} = \exp(-\frac{i}{\hbar}\mathcal{H}t)$ is called time evolution operator [81].

For our NMR experiments, the spin system has a piece-wise constant Hamiltonian, i.e. $\mathcal{H}_{tot}$ (Equation (4.10)) during a pulse of duration t_p and $\mathcal{H}_{int}$ (Equation (4.9)) during the free evolution time τ. The time evolution operator for a pulse event is $\mathcal{U} = \exp(-\frac{i}{\hbar}\mathcal{H}_{tot}t_p)$. In the δ-pulse approximation, $-\hbar\omega_1 I_{\phi_T}$ is used to replace the full $\mathcal{H}_{tot}$, and we get $\mathcal{U} = \exp(i\omega_1 I_{\phi_T}t_p)$. Using the fact that $\omega_1 t_p = \pi$ for a 180° pulse, we get the time evolution operator for the event of π pulse in the δ-pulse approximation,

$$\mathcal{R}_\phi = \mathrm{e}^{i\pi I_{\phi_T}} \tag{4.17}$$

where $\mathcal{R}$ is used to indicate the fact that it is a pure rotation operator.

Let us now use the density matrix and time evolution operators to analyze the HE and CPMG experiments. Note that HE is the special case of CPMG: $90_X - \{\tau - 180_Y - \tau\}^m$ with m=1, so we will just work with CPMG. Since the transverse magnetization measured in experiments can be calculated using the density matrix,

$$\langle I_{x_T}\rangle = \mathrm{Tr}[\rho(t)I_{x_T}]$$

$$\langle I_{y_T}\rangle = \mathrm{Tr}[\rho(t)I_{y_T}]$$

we basically just need to know $\rho(t)$. We set the density matrix right after the first tipping 90° pulse as $\rho(0)$, and under the high-temperature and high-field approximation $\rho(0) = I_{y_T}$ [84]. $\rho(t)$ for CPMG is,

$$\rho(t) = \{\mathcal{U}\mathcal{R}_y\mathcal{U}\}^m \rho(0) \{\mathcal{U}^{-1}\mathcal{R}_y^{-1}\mathcal{U}^{-1}\}^m \tag{4.18}$$

where $\mathcal{U} = \exp(-\frac{i}{\hbar}\mathcal{H}_{int}\tau)$. Using the facts that $\mathcal{H}_{int} = \mathcal{H}_Z + \mathcal{H}_{zz}$ and $[\mathcal{H}_Z, \mathcal{H}_{zz}] = 0$, $\mathcal{U}$ can be rewritten as,

$$\mathcal{U} = \mathrm{e}^{-\frac{i}{\hbar}\mathcal{H}_Z\tau}\mathrm{e}^{-\frac{i}{\hbar}\mathcal{H}_{zz}\tau} = \mathcal{U}_Z\mathcal{U}_{zz} \tag{4.19}$$

where the theorem $\mathrm{e}^{A+B} = \mathrm{e}^A + \mathrm{e}^B + \mathrm{e}^{-\frac{1}{2}[A,B]}$ is applied (a proof of this theorem can be found in the Appendix A of the NMR book by C. P. Slichter [84]). Furthermore, $\mathcal{U}_Z$ and $\mathcal{U}_{zz}$ have the following properties under the operation of the π rotation operator $\mathcal{R}_\phi$ (where ϕ=x or y),

$$\mathcal{R}_\phi\mathcal{U}_Z\mathcal{R}_\phi^{-1} = \mathcal{U}_Z^{-1} \tag{4.20}$$

$$\mathcal{R}_\phi\mathcal{U}_{zz}\mathcal{R}_\phi^{-1} = \mathcal{U}_{zz}. \tag{4.21}$$

With these above equations in mind, we can analyze $\rho(t)$ for CPMG in the fol-

lowing way,

$$\begin{aligned}
\rho(t) &= \{\mathcal{U}R_y\mathcal{U}\}^m \rho(0) \{\mathcal{U}^{-1}\mathcal{R}_y^{-1}\mathcal{U}^{-1}\}^m \\
&= \{\mathcal{U}\mathcal{R}_y(\mathcal{R}_y^{-1}\mathcal{R}_y)\mathcal{U}(\mathcal{R}_y^{-1}\mathcal{R}_y)\}^m \rho(0)\{inv\}^m \\
&= \{\mathcal{U}_{zz}\mathcal{U}_Z\mathcal{U}_Z^{-1}\mathcal{U}_{zz}\mathcal{R}_y\}^m \rho(0)\{inv\}^m \\
&= (\mathcal{U}_{zz})^{2m}(R_y)^m\rho(0)(R_y^{-1})^m(\mathcal{U}_{zz}^{-1})^{2m} \\
&= (\mathcal{U}_{zz})^{2m}\rho(0)(\mathcal{U}_{zz}^{-1})^{2m} \\
&= \mathcal{U}_{zz}(t)\rho(0)\mathcal{U}_{zz}^{-1}(t). \qquad (4.22)
\end{aligned}$$

where $\{inv\}$ is the inverse of the operators in brackets to the left of $\rho(0)$, $\mathcal{U}_{zz}(t) = \exp(-\frac{i}{\hbar}\mathcal{H}_{zz}t)$, and we used the fact that $(R_y)^m\rho(0)(R_y^{-1})^m = I_{y_T}$ since a rotation operator along the Y-axis leaves I_y the same. Note that $\rho(t)$ for HE can be obtained by setting $t = 2\tau$ in Equation (4.22).

Equation (4.22) says that in the δ-pulse approximation, $\rho(t)$ of both CPMG and HE depends only on the dipolar time-evolution operator $\mathcal{U}_{zz}$, which implies that the decay of CPMG and HE is caused by $\mathcal{H}_{zz}$ only. This result is consistent with the related analysis used in Section 4.4. Moreover, APCPMG has the same $\rho(t)$ as CPMG, while for AP and APCP we need to make a slight change since $(R_x)^m\rho(0)(R_x^{-1})^m = (-1)^m I_{y_T}$.

Chapter 5

Exact Calculations with Finite Pulses

In the last Chapter, we introduced the unexpected spin echoes in CPMG experiment that appeared long after the HE decayed to zero, and also the puzzling PSS in the multiple π pulse experiments. After we observed these effects, we tried hard to understand them. The first thing came to our mind was that these effects were caused by experimental imperfections. Indeed, the δ-pulse approximation prediction that the T_2 measurement by HE and CPMG should agree with each other does assume perfect pulse rotations. In practice, experimental errors are always present at some level. Therefore, we spent a lot of time exploring many possible experimental errors, trying to assess and quantify their effects. The detailed description of these efforts can be found in our publication [48] and in Dr. Li's doctoral thesis [46]. Here, I will just give a list of some of the things we have considered,

- RF pulse power variation
- Calibration of pulse angle

- RF homogeneity (coil filling factor variation)
- Pulse timings (uneven spacing)
- Repetition rate (long compared to T_1)
- Doping (concentration, type)
- Dipolar coupling strength (Magic Angle Spinning)
- Natural abundance variation (different nuclei)
- Susceptibility broadening (single crystal)
- Phase transients (changing the resonance circuit quality factor Q)
- Temperature (room temperature and 4.2 K)
- Other pulse sequences (composite pulses)

However, the above extrinsic factors could not explain our experiments. Even after greatly improving our experimental conditions, the tail of CPMG echo train persisted well beyond the decay of HE, and the PSS was still observed. Furthermore, we also obtained similar results with other samples such as ^{13}C in ^{60}C and ^{89}Y in Y_2O_3 [48], and comparable experimental observations were also reported by other groups in NMR and ESR [25, 44, 51, 90]. Exclusion of the extrinsic factors from playing a significant role pushes us to search for possible intrinsic reasons, which led us to

question the validity of the δ-pulse approximation. After all, it is the foundation of those apparently wrong predictions.

As we discussed in Chapter 4, in the δ-pulse approximation a pure π rotation leaves $\mathcal{H}_{zz}$ unchanged, while the sign of $\mathcal{H}_Z$ is reversed. However, in practice any real RF pulse takes a non-zero duration to finsh. When the non-zero duration of a pulse is taken into account, the Hamiltonian of a dipolar spin system is not just the external pulse Hamiltonian $\mathcal{H}_p$, but the full $\mathcal{H}_{tot} = \mathcal{H}_p + \mathcal{H}_{int}$ as given in Equation (4.10). But how big is the effect of $\mathcal{H}_{int}$ during π pulses? In this Chapter, we will present our computer simulations that were used to answer this question.

As mentioned in Chapter 4, the samples that we studied appear to be described by the following internal Hamiltonian (without any pulse),

$$\mathcal{H}_{int} = \sum_{i=1}^{N} \Omega_{z_i} I_{z_i} + \sum_{j>i}^{N} B_{ij}\{3I_{z_i}I_{z_j} - \vec{I}_i \cdot \vec{I}_j\} = \mathcal{H}_Z + \mathcal{H}_{zz} \tag{5.1}$$

where $\Omega_{z_i} = -\gamma\hbar\Delta H_i^{Loc}$ and B_{ij} is the dipolar coupling constant. Many of our earliest calculations considered the case that nearby spins had quite different Ω_{z_i} values. As we moved to study lightly-doped Silicon, C_{60}, and adamantane, we realized that bulk diamagnetic broadening was dominating the Zeeman linewidth of our data. This allowed us to further simplify our model by assuming that a cluster of just a few spins (N<9 in our simulations) were close enough to share the same local Zeeman frequency Ω_{z_i}. The internal Hamiltonian then becomes:

$$\mathcal{H}_{int} = \Omega_z I_{z_T} + \mathcal{H}_{zz}, \qquad \text{where} \quad I_{z_T} = \sum_{i=1}^{N} I_{z_i} \tag{5.2}$$

which assumes that all the N spins (N<9) within a cluster have the same Ω_z. However, across a macroscopic sample, other clusters of spins can have different Ω_z values. Therefore, we typically draw Ω_z values from a Gaussian distribution in the simulations that are averaged over multiple disorder realizations (DRs). In the sections and figures that follow, if a value is given for Ω_z, it refers to the FWHM of the Gaussian distribution of Ω_z used in the corresponding simulations.

To numerically simulate a decay curve using finite pulses (throughout this thesis, the term finite pulses refers to pulses with non-zero durations), we use the Silicon lattice as a model. Because the ^{29}Si isotope has a natural abundance (n.a.) of 4.67 %, our simulations are usually averaged over many DRs on a Silicon lattice. For each DR, we choose a central spin in a randomly oriented Silicon lattice (since the samples are usually crushed powders), then around the central spin, the ^{29}Si spins are randomly populated according to its n.a. of 4.67 %. For the case of nonzero Zeeman spread, each DR uses an Ω_z value drawn from a gaussian distribution with a certain FWHM. The density matrix is used to calculate the transverse magnetization of the central spin along $< I_{y_1}(t) >$ [84]. All the simulations in this thesis were done using the software IGOR by WaveMetrics, and a detailed description of the CPMG simulation procedure can be found in the Appendix.

5.1 Simulations in Weak Pulse Limit

V. Dobrovitski, through private communication, first pointed out that a big Zeeman spread during weak pulses (relatively long t_p) could generate the abnormal NMR behavior that we observed. We later confirmed his results though our independent simulations.

In the weak-pulse limit, the π pulses are no longer perfect 180° rotations around the intended axes due to the big Ω_z. For example, a perfect 180° rotation about the Y-axis leaves I_y the same, while changes I_x to $-I_x$. However, in the presence of a big Ω_z, the rotation is no longer about the Y-axis, but about a Y'-axis which forms an angle $\delta\theta$ with the Y-axis in the Y-Z plane ($\tan\delta\theta = \frac{\delta H_z}{H_1}$, where $\delta H_z = -\frac{\Omega_z}{\gamma}$ and H_1 is the pulse strength). Thus this pulse rotates I_y to $aI_y + bI_z$, and I_x to $-cI_x + dI_z$, where a, b, c, d are parameters depending on $\delta\theta$. In the weak pulse limit ($\delta\theta$ is big), b and d can be of the same order as a and c, which means the intended π rotations about the Y-axis in CPMG have non-negligible errors. These pulse imperfections can lead to a long-lived echo tail in CPMG when τ is small, or an even-odd asymmetry when τ is big (Figure 5.1), just as what we observed in many dipolar solid samples [17, 48].

However, since these simulation results are due to weak pulse errors, it is expected that the long tail height will decrease with increasing pulse strength. Indeed, as the pulse strength is increased in simulations, the CPMG tail height gets smaller and

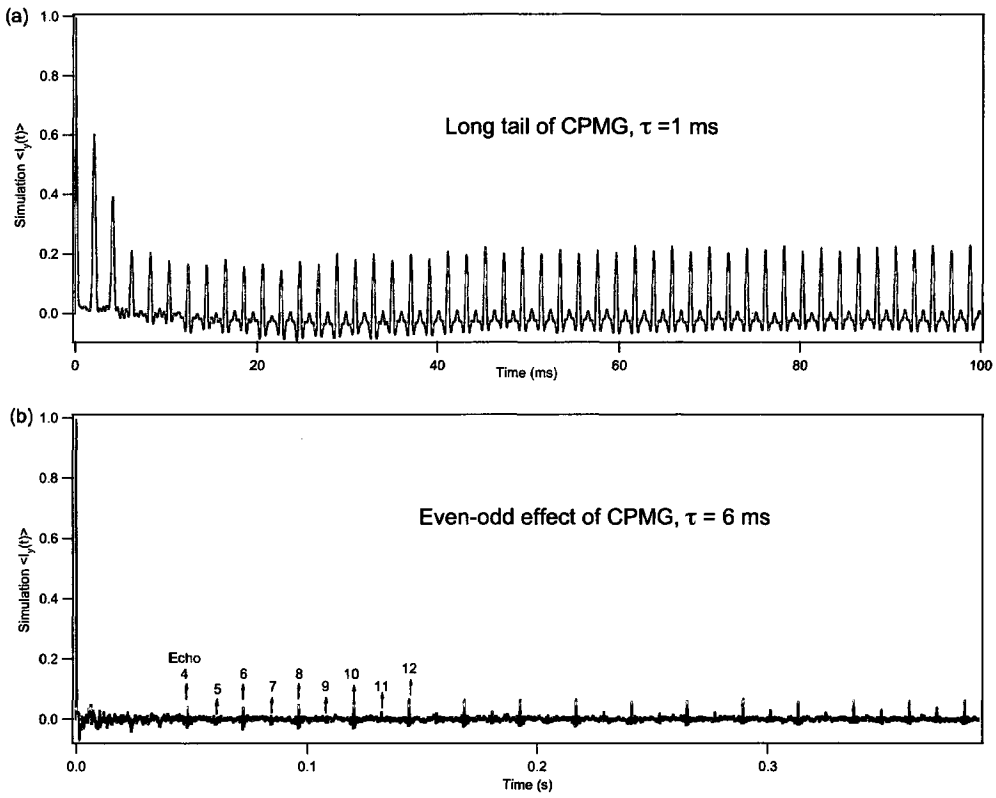

Figure 5.1: The exact calculation of CPMG for (a) τ=1ms and (b) τ= 6ms, using N=6 spins, pulse strength $\omega_1/2\pi$ =8.5 kHz, $\Omega_z/2\pi$=2.5 kHz, and averaged over 400 DRs. In this weak pulse limit, CPMG simulation shows a long-lived echo tail when τ is short (1ms) and even-odd effect when τ is longer (6 ms). The even-odd effect refers to the observation that even-numbered echoes are bigger than then odd-numbered echoes. For example, echo number 10 is bigger than echo number 9, despite the fact echo 9 occurs earlier than echo 10.

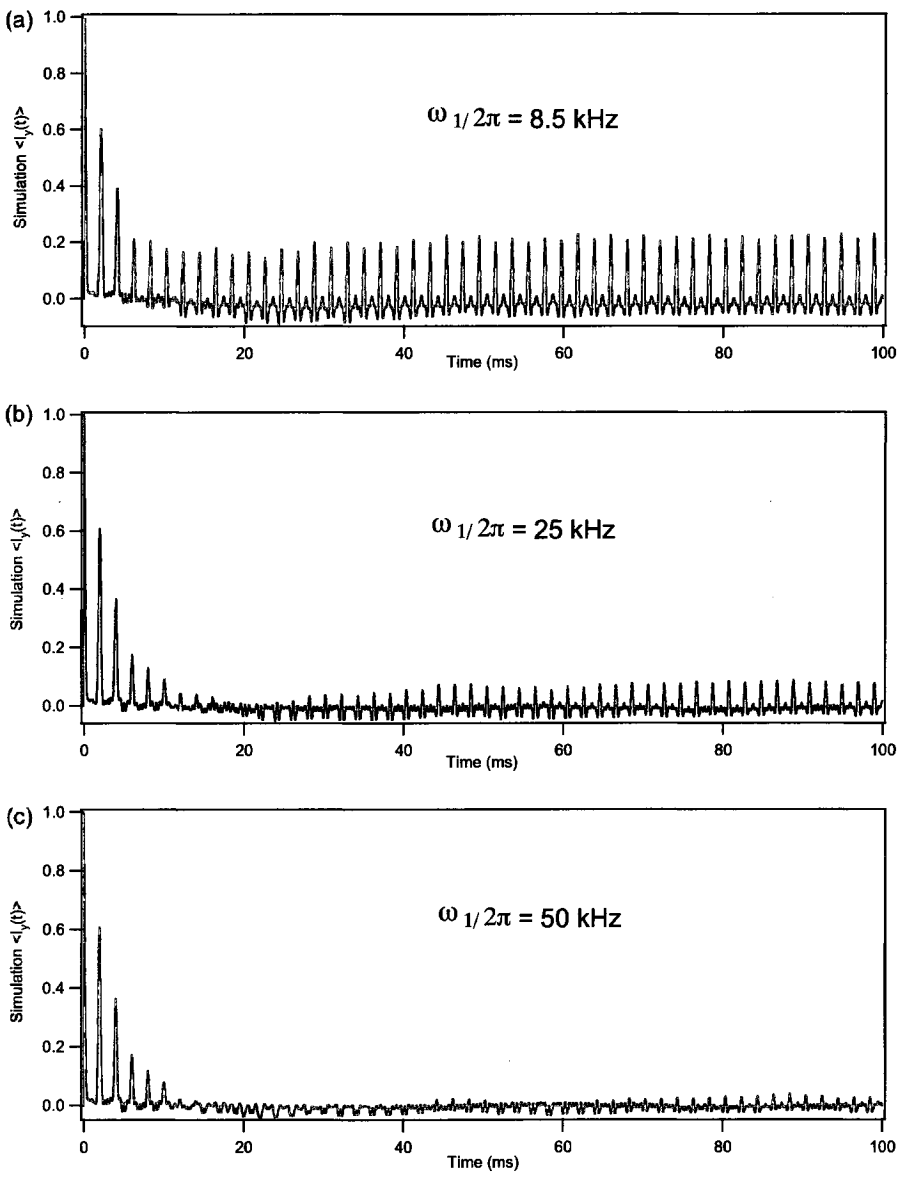

Figure 5.2: The exact simulations of CPMG for different H_1 values, using 6 spins, $\Omega_z/2\pi$=2.5 kHz, τ=1ms, and averaged over 400 DRs. The long CPMG echo tail due to weak pulses (a) starts to decease as $\omega_1/2\pi$ is increased to 25 kHz(b) and the tail drops to almost zero when $\omega_1/2\pi = 50$ kHz (c).

smaller until it is hard to observe when the pulses are only 20 times stronger than Ω_z (Figure 5.2). But in experiments, the tail height of CPMG does not seem to depend on the pulse strength in a wide range, and similar tail height has been observed with pulses as strong as a few hundred times of the linewidth, as it is shown in Figure 5.3. Therefore, even though the weak pulse simulations show some results resembling our experiments, they do not really explain our data.

Note that the simulation results in this section are essentially the same even when $\mathcal{H}_{zz}$ is set to zero during the pulses, in contrast to the strong-pulse simulations we will discuss next.

5.2 Simulations in Strong Pulse Limit

In real experiments, we used strong pulses, from at least tens of times to a few hundred times of the spectral linewidth. As interesting as they are, the weak pulse simulations fail to explain the long CPMG tail when pulses are strong compared to the spectral linewidth. When using the same parameters as in the real experiments (the same pulse strength, the same cycle time, realistic Zeeman spread and dipolar coupling strength) in the simulations with N=7 spins, the simulation results seem nothing like the experiments (Figure 5.4). However, as you zoom in, you will find that the four simulations do differ from each other in the same way as in the experiments. Note that if the δ-pulse approximation was assumed in these four simulations, they yield exactly the same decay curve. The non-zero duration of pulses is the sole cause of

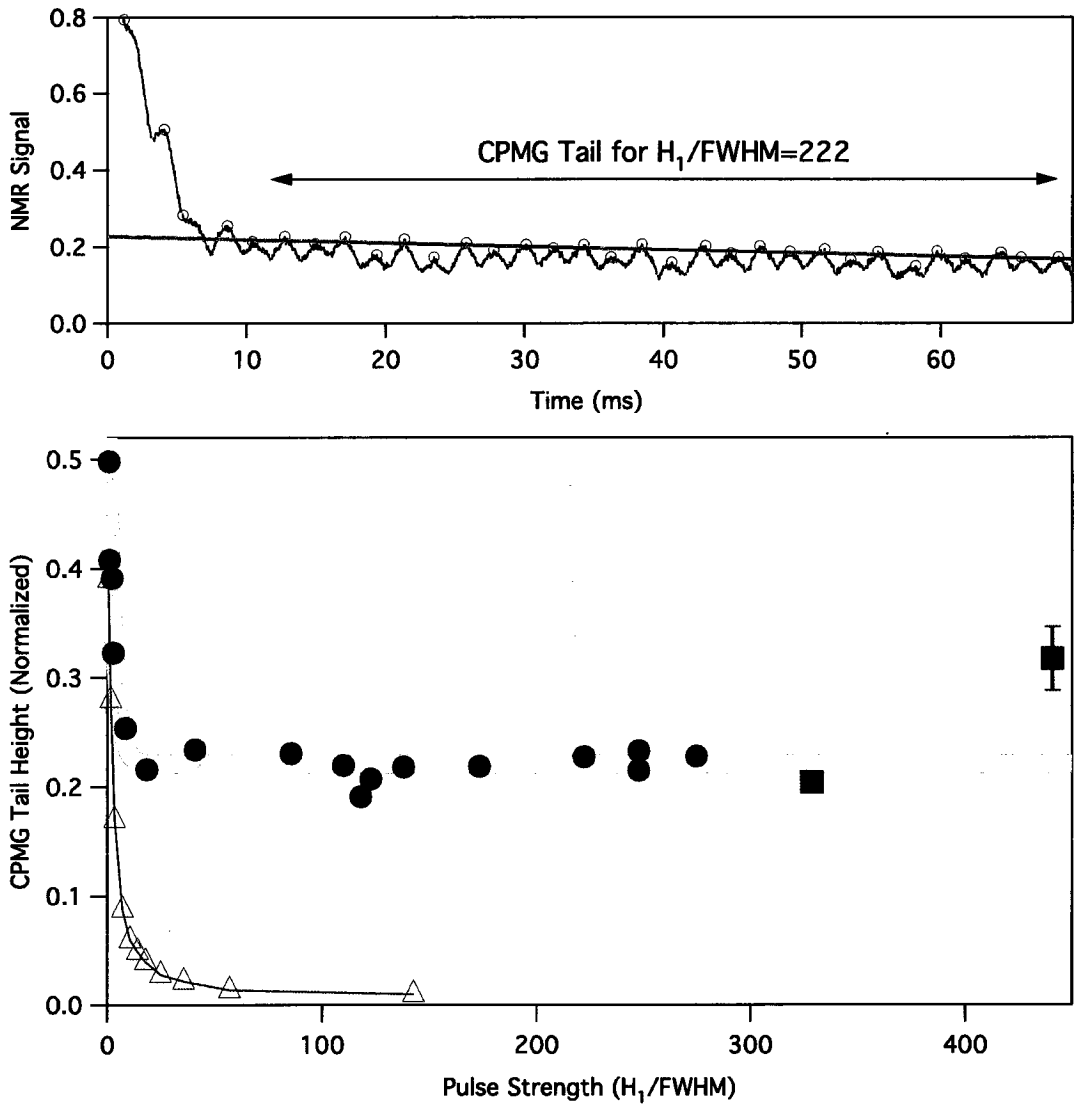

Figure 5.3: Dependence of CPMG tail height on pulse strength. (Top) Tail height is extrapolated as a $t = 0$ intercept for CPMG of ^{29}Si in Si:Sb (10^{17} Sb/cm^3) with $2\tau = 2.192$ ms. This example is for H_1/FWHM=222. (Bottom) CPMG tail height versus pulse strength. Smaller samples and NMR coils were used to achieve the last two points. Exact simulations for N=5 spins in Silicon (triangles) decay to zero for H_1 >FWHM.

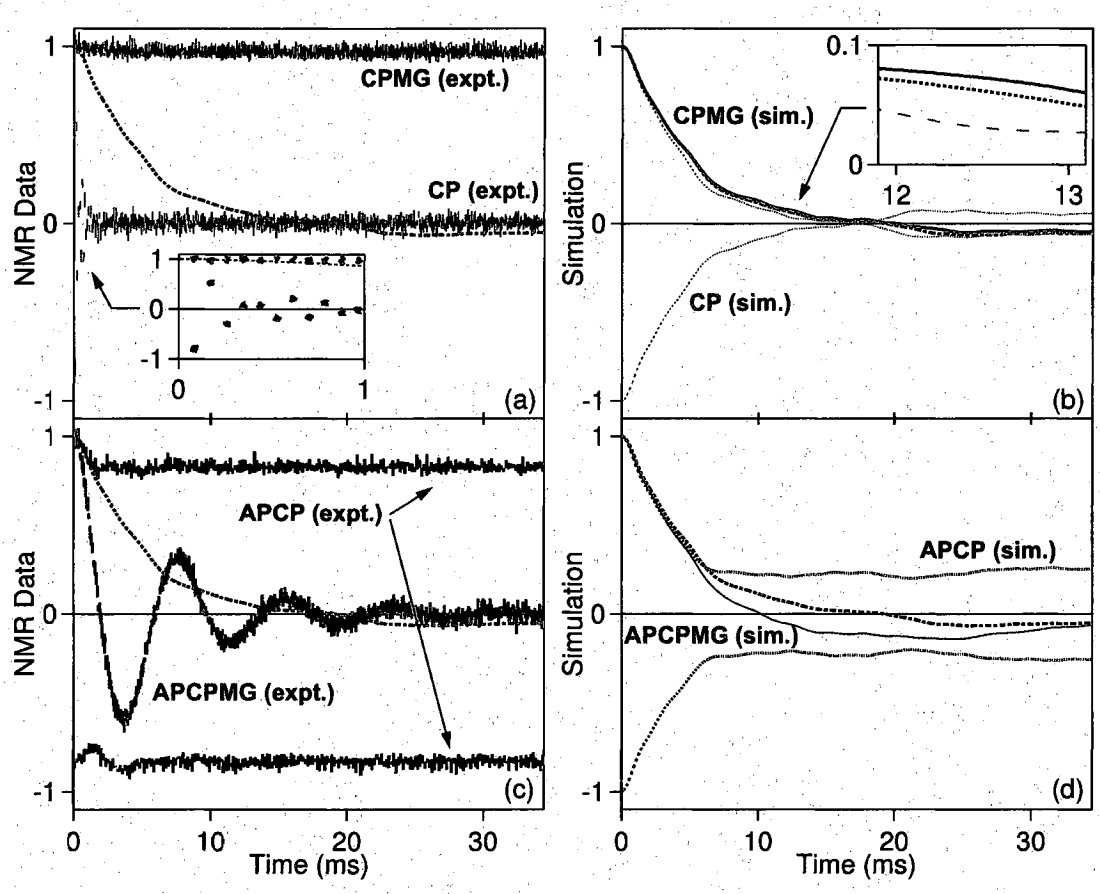

Figure 5.4: (a), (c) ^{29}Si measurements in Si:Sb (10^{17} Sb/cm^3) with the four phase choices from Table 5.1. (b), (d) Simulations with 7 spins for the same experimental conditions: t_p=14 μs, τ=36 μs, and $\omega_1/2\pi$=35.7 kHz, in a 11.75 Tesla field at room temperature. Each curve is averaged over 1000 DRs with Ω_z/h drawn from a 290 Hz wide Gaussian distribution and typical couplings $|B_{12}|/h \approx 44.5$ Hz, $|B_{17}|/h \approx 3.5$ Hz. Inset (a) shows rapid decay of CP data. Inset (b) shows a distinction between CP and CPMG simulations. The black dashed reference (a)-(d) sets $\Omega_z = 0$ and turns off $\mathcal{H}_{zz}$ during each pulse.

Sequence	ϕ_1	ϕ_2	Echo1	Echo2
CP	$+X$	$+X$	$-Y$	$+Y$
APCP	$-X$	$+X$	$-Y$	$+Y$
CPMG	$+Y$	$+Y$	$+Y$	$+Y$
APCPMG	$-Y$	$+Y$	$+Y$	$+Y$

Table 5.1: π pulse and echo phases for four pulse sequences of the form: 90_X-$\{\tau$-180_{ϕ_1}-τ-Echo1-τ-180_{ϕ_2}-τ-Echo2-$\}^n$.

the tiny PSS seen in the N=7 exact calculations (Figure 5.4(b) and 5.4(d)) since no extrinsic pulse errors are included in the simulations. The dashed reference shown in Figure 5.4(a)-5.4(d) is the N=7 exact calculation of CPMG for $\Omega_z = 0$, with $\mathcal{H}_{int}$ set to zero during the pulses. This dashed reference represents the δ-pulse approximation. Given the strength of the pulses, H_1/ FWHM= 108 (H_1 is expressed in Hz, which is actually $\omega_1/2\pi$. We use H_1 for a simpler notation), we were surprised to see any difference in the simulations.

On the other hand, the small PSS in the simulations shown in Figure 5.4 is too tiny to explain the experiments. However, we only included N=7 spins in the simulations due to the limitation of computer power, while every ^{29}Si spin powder cluster in the sample has probably millions of spins. We then hypothesized that if we could include far more spins in our simulations, we might see the dramatic PSS as we saw in experiments. At this point, there is no way to directly test our projection since the current computers can not include that many spins in the simulations using exact diagonalization of density matrix of $2^N \times 2^N$ where N is the number of spins. On the other hand, if our model is correct, then a sample with clusters of just a few spins

should show really small PSS. To test this idea experimentally, we found a promising candidate sample, the liquid crystal 5CB (4-pentyl-4-cyanobiphenyl).

5.3 A Hint from Liquid Crystal 5CB Experiments

Liquid crystal 5CB has a simple phase transition from solid phase to nematic phase at about 23 C°, and from nematic phase to isotropic liquid phase at around 35 C° when heated [11, 22, 64]. In the solid phase, 5CB is an extended dipolar system just like the Silicon sample, i.e., a very large number of spins are coupled together. In the nematic phase, on the other hand, each 5CB molecule rotates about a certain axis, which causes the inter-molecular dipolar couplings between two molecules to average out, while the intra-dipolar couplings of 19 ^{1}H spins within a molecule is largely kept [2, 22, 64, 63]. Therefore, in nematic phase each 5CB molecule acts like an isolated nuclear spin system with 19 ^{1}H spins.

Thus, if our idea that many spins are required for a large PSS effect is correct, a transition from big PSS to small PSS should be observed when a 5CB sample is brought from the solid phase (a many-spin system) to the nematic phase (a few-spin system).

The experiments were carried out with nitrogen gas blowing to the sample stage to control the temperature. The nitrogen gas coming out of the liquid nitrogen dewar was cold enough to bring 5CB to its solid phase (~15 C°). A heater wrapped around

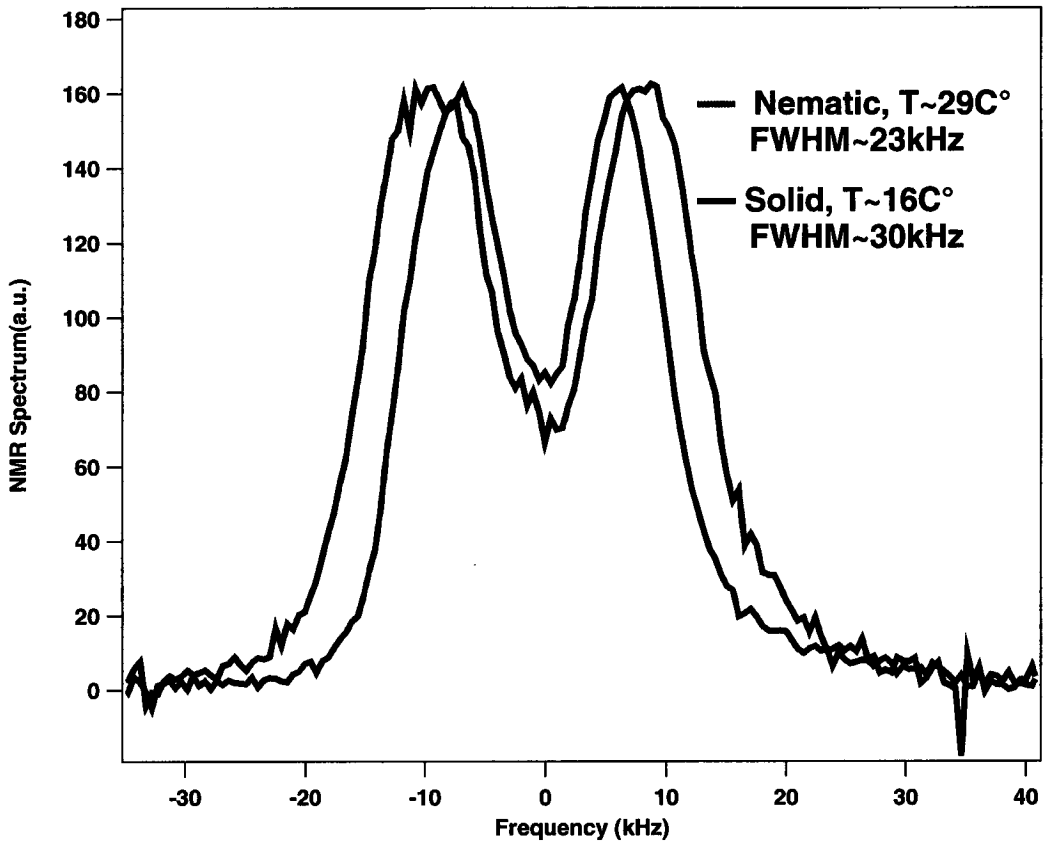

Figure 5.5: FID spectra of ^{1}H in 5CB in solid phase (blue) taken at $\sim$ 15 C° and nematic phase (red) taken at $\sim$ 29 C°. Data taken with $\omega_1/2\pi$ =57.5 kHz in a 12 Tesla magnetic field.

the nitrogen gas tube was used to heat the nitrogen gas before it blew into the sample stage to warm up the sample to around 29 C° to achieve the nematic phase. The FID spectra of the sample in solid and nematic phase are shown is Figure 5.5.

However, when we tried to test our hypothesis, we were disappointed to observe hardly any change in the PSS as the sample was warmed from the solid phase to the nematic phase. Note that the PSS of 5CB in Figure 5.6 is not as dramatic as it is for Silicon in Figure 5.4 because here the spectral linewidth is much bigger. A stronger

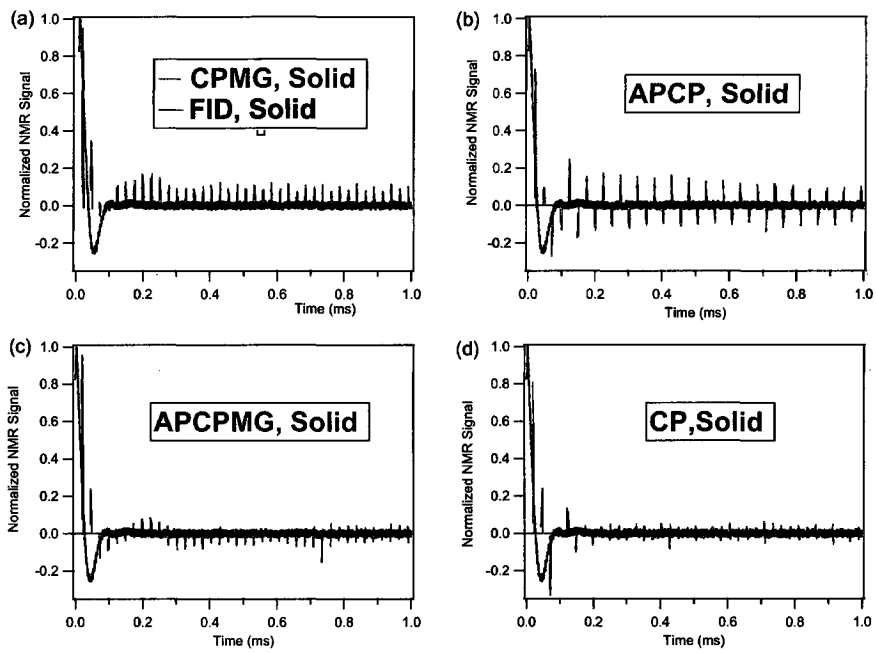

Figure 5.6: The CPMG, APCP, APCPMG, CP experiments of ^{1}H in 5CB in the solid phase at $\sim$ 15 C°. The black trace is the FID in solid phase, which provides a close estimate of Hahn Echo decay curve since the dipolar linewidth greatly dominates the FID spectrum. Even though the signal-to-noise ratio is not very good and the PSS present is small, these four experiments still suggest the same PSS: CPMG and APCP give a long-lived echo tail, while APCPMG and CP decay to zero (or very close to zero). Data taken with $\omega_1/2\pi = 57.5$ kHz, τ=8.4 μs in a 12 Tesla magnetic field.

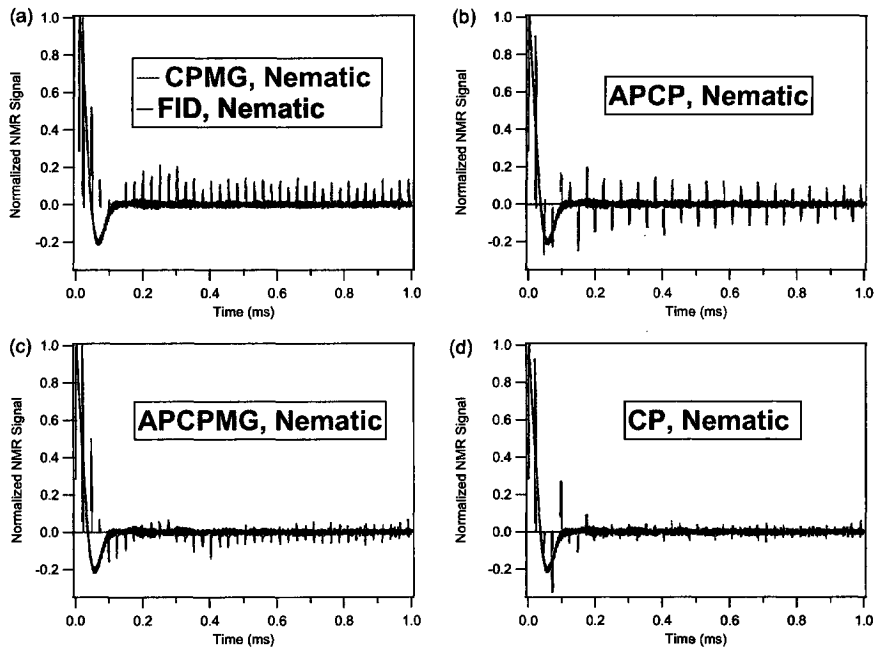

Figure 5.7: The CPMG, APCP, APCPMG, CP experiments of ^{1}H in 5CB in the nematic phase at $\sim$ 29 C°. Despite the fact that the signal-to-noise ratio is not very good, these four experiments give almost exactly the same results as those four taken in solid phase (Figure 5.6). Data taken with $\omega_1/2\pi$ = 57.5 kHz, τ=8.4 μs in a 12 Tesla magnetic field.

pulse strength and a shorter cycle period are needed to increase the size of PSS, which unfortunately was hard to realize with our experimental conditions. Even though the PSS is not as dramatic, these experiments of 5CB still suggest qualitatively the same results as we observed in many other samples [17, 47, 48]. When measured in the nematic phase of 5CB (Figure 5.7), these four pulse sequences give almost exactly the same results as those four taken in the solid phase (Figure 5.6), contrary to our prediction. So, was our prediction completely wrong?

One big difference between the Silicon sample and the 5CB sample is that the dipolar coupling constant B_{ij} of ^{1}H spins in 5CB is about 25 times bigger than that of ^{29}Si in Silicon, corresponding to a $\sim$25 times bigger dipolar Hamiltonian term. So, if bigger dipolar coupling constant is used in the simulations, will a few spins be enough to give a dramatic PSS? We returned to simulations to answer this question.

5.4 Simulations with Inflated Dipolar Coupling

Indeed, when we used a bigger dipolar coupling constant in simulations, we discovered that this could give a long CPMG tail, even in the strong pulse limit with $\Omega_z = 0$ and just a few spins. When the normal dipolar coupling strength B_{ij} of ^{29}Si is used, the CPMG calculation decays to zero (Figure 5.8 (a)). However, as the dipolar coupling constant is inflated to $25 \times B_{ij}$ (Figure 5.8 (b)), and even $150 \times B_{ij}$(Figure 5.8 (c)), a CPMG long tail starts to show up despite the fact that only a few spins are included in these strong pulse calculations. Furthermore, the tail height seems to be proportional

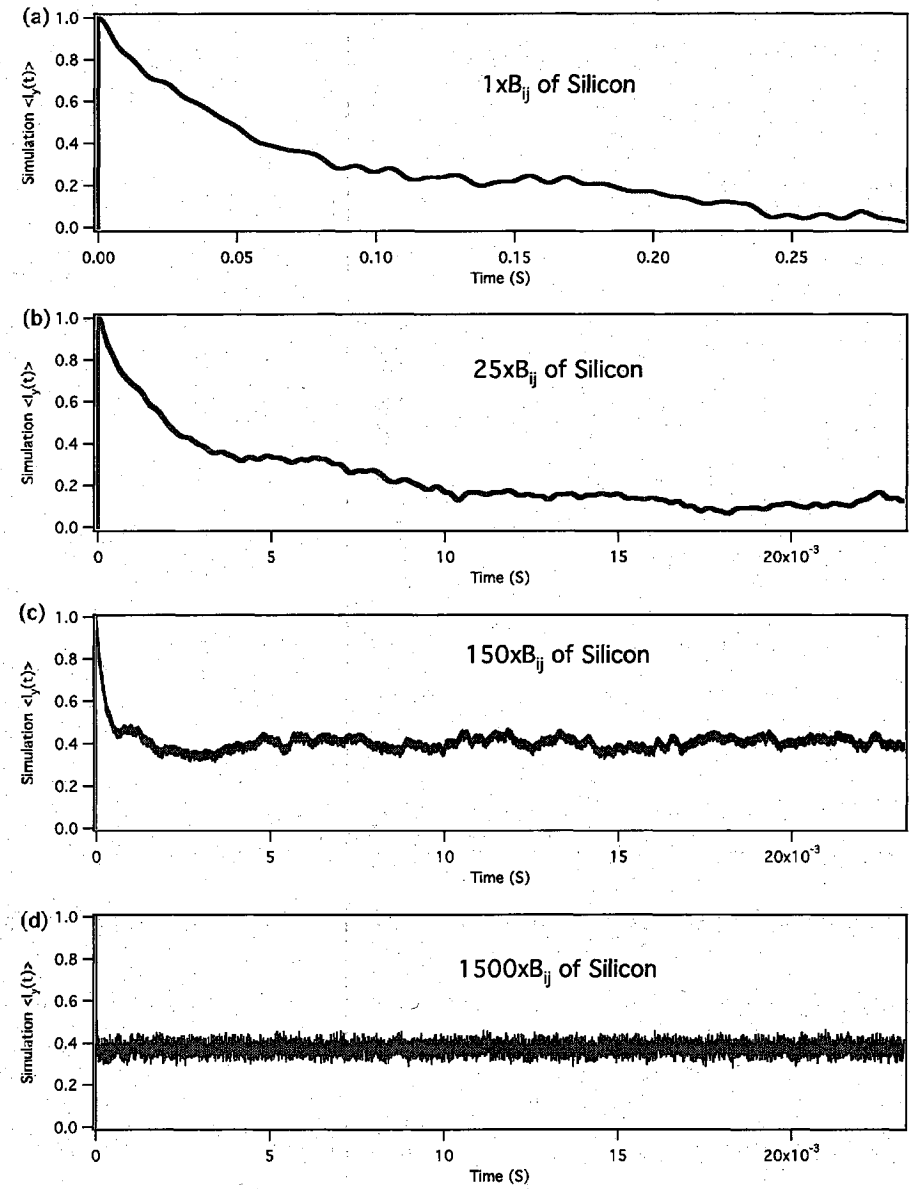

Figure 5.8: Exact CPMG simulations with different dipolar coupling strength. As the dipolar coupling strength is increased, the height of CPMG echo tail increases until it gets saturated at some level. All simulations use $\Omega_z = 0$, $\omega_1/2\pi$=40 kHz, τ=1 μs, and averaged over 100 disorder realizations (DRs) of N=4 spins on a Silicon lattice.

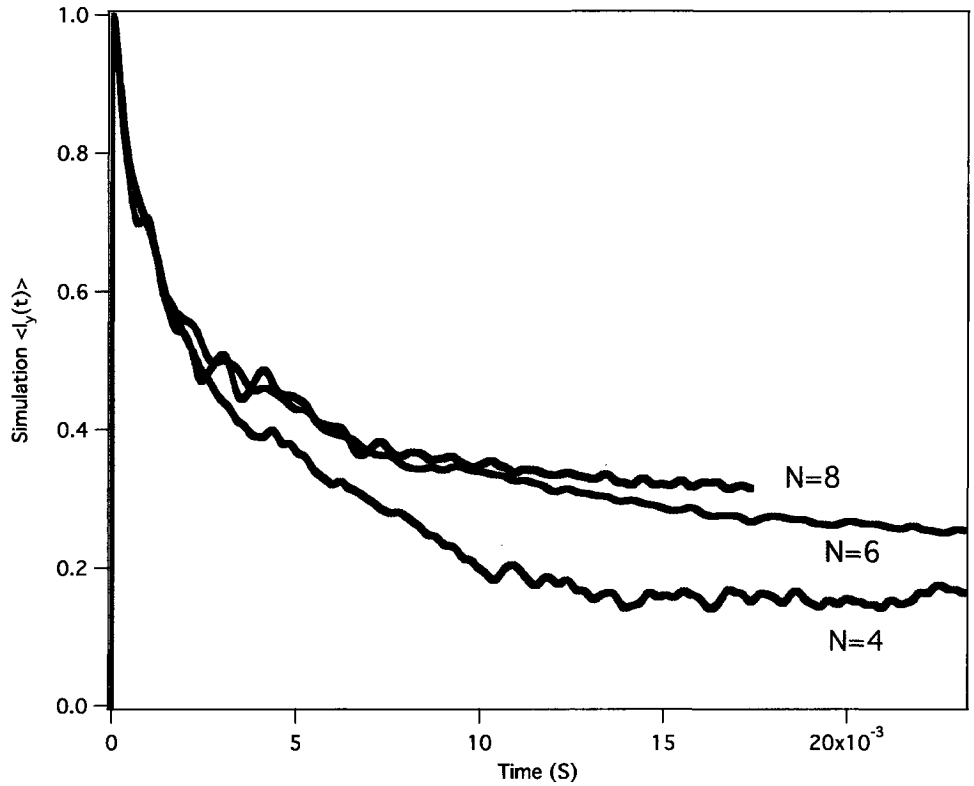

Figure 5.9: The exact simulations of CPMG with dipolar coupling strength $25 \times B_{ij}$ of ^{29}Si, $\Omega_z = 0$, $\omega_1/2\pi$=40 kHz, τ=1 μs, and (a) N=8 (red, 80 DRs), (b) N=6 (blue, 400 DRs), and (c) N=4 (green, 400 DRs).

to the dipolar coupling strength until it gets saturated after reaching a certain limit. For example, $150 \times B_{ij}$ gives a higher echo tail than $25 \times B_{ij}$, but $1500 \times B_{ij}$ and $150 \times B_{ij}$ result in similar tail height. Perhaps this saturation effect is the reason why the CPMG tail of 5CB in the solid phase (a many-spin system, Figure 5.6 (a)) is not noticeably higher than that in the nematic phase (a 19-spin system, Figure 5.7 (a)).

As mentioned before, we proposed that the tiny PSS observed in the $1 \times B_{ij}$

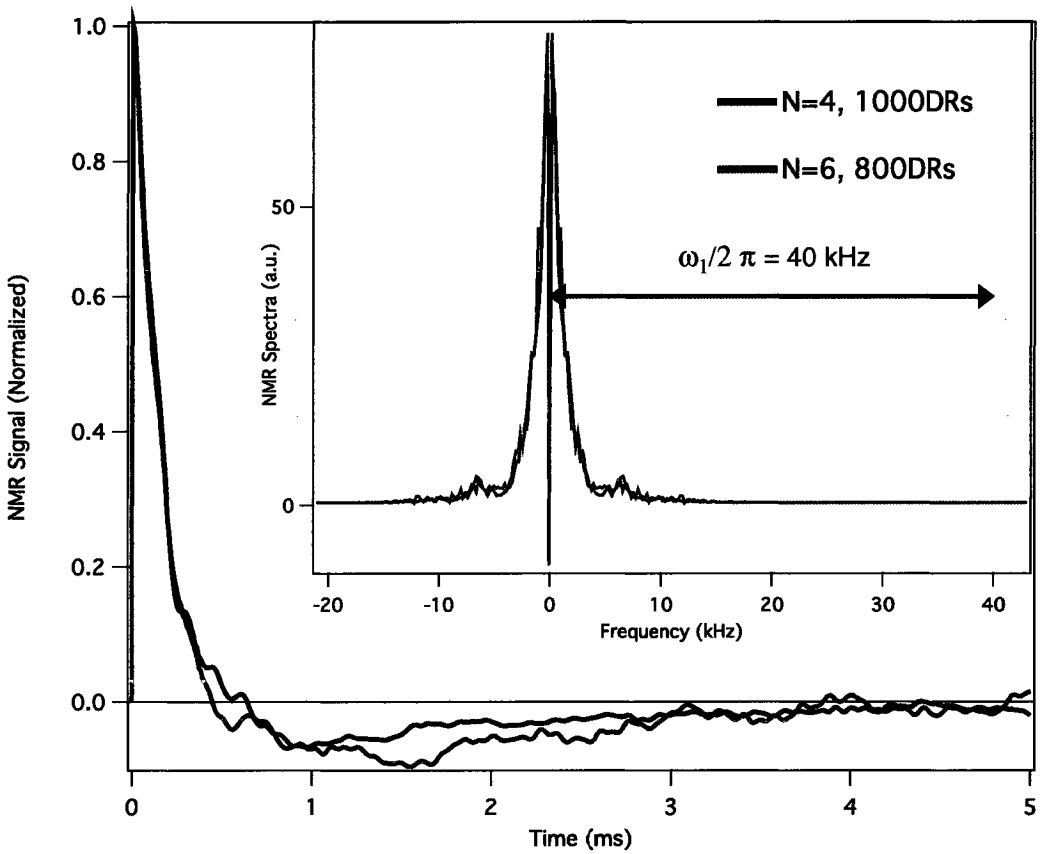

Figure 5.10: (top) Exact calculations of the FID for N=4 (red, 1000 DRs) and N=6 (blue, 800 DRs), with $25 \times B_{ij}$ of ^{29}Si, $\Omega_z = 0$, $\omega_1/2\pi$=40 kHz, and τ=1 μs. These two FID decay curves are in good agreement, as expected for the essentially identical spectra (inset) for N=4 (red) and N=6 (blue), and for the strong ω_1 used.

simulations in Figure 5.4 would be more dramatic if a large enough number of spins could be included. This proposal became more promising after we found that the CPMG tail height actually increased with spin number N in the $25 \times B_{ij}$ simulations, as shown in Figure 5.9. The N=8 simulation takes a long time to complete for each DR, so the red trace for N=8 in Figure 5.9 is only averaged over 80 DRs. Nevertheless, it is clear that the calculation with larger N gives a bigger echo tail. This result makes it more plausible that a CPMG long tail exists in simulations using the actual experimental parameters (i.e. no inflation of dipolar coupling strength), provided that a large enough number of spins can be included. Note that the $25 \times B_{ij}$ simulations with N=4 and N=6 give similar FID decay curves, hence similar FID spectra (Figure 5.10). Similar FID spectra suggest that the dipolar linewidth does not really increase with spin number N, at least for $N \leq 8$. This may explain why the initial decay of the three CPMG simulations in Figure 5.9 all looks very similar, because the initial decay is determined mainly by the dipolar linewidth. The fact that these three curves start to develop an echo tail after the initial decay suggests that the long echo tail is a many-pulse effect, i.e., it only shows up after many phase-coherent π pulses are applied.

Furthermore, a phenomenological scaling rule appears to fit our simulations (Figure 5.11). The CPMG tail height appears to be similar for calculations with different N values, provided that we also adjust the B_{ij} scale to make $||\mathcal{H}_{zz}||^2 \equiv Tr\{\mathcal{H}_{zz}^{\dagger}\mathcal{H}_{zz}\}$ similar. Note that this adjustment of both N and B_{ij} scale means that the local field

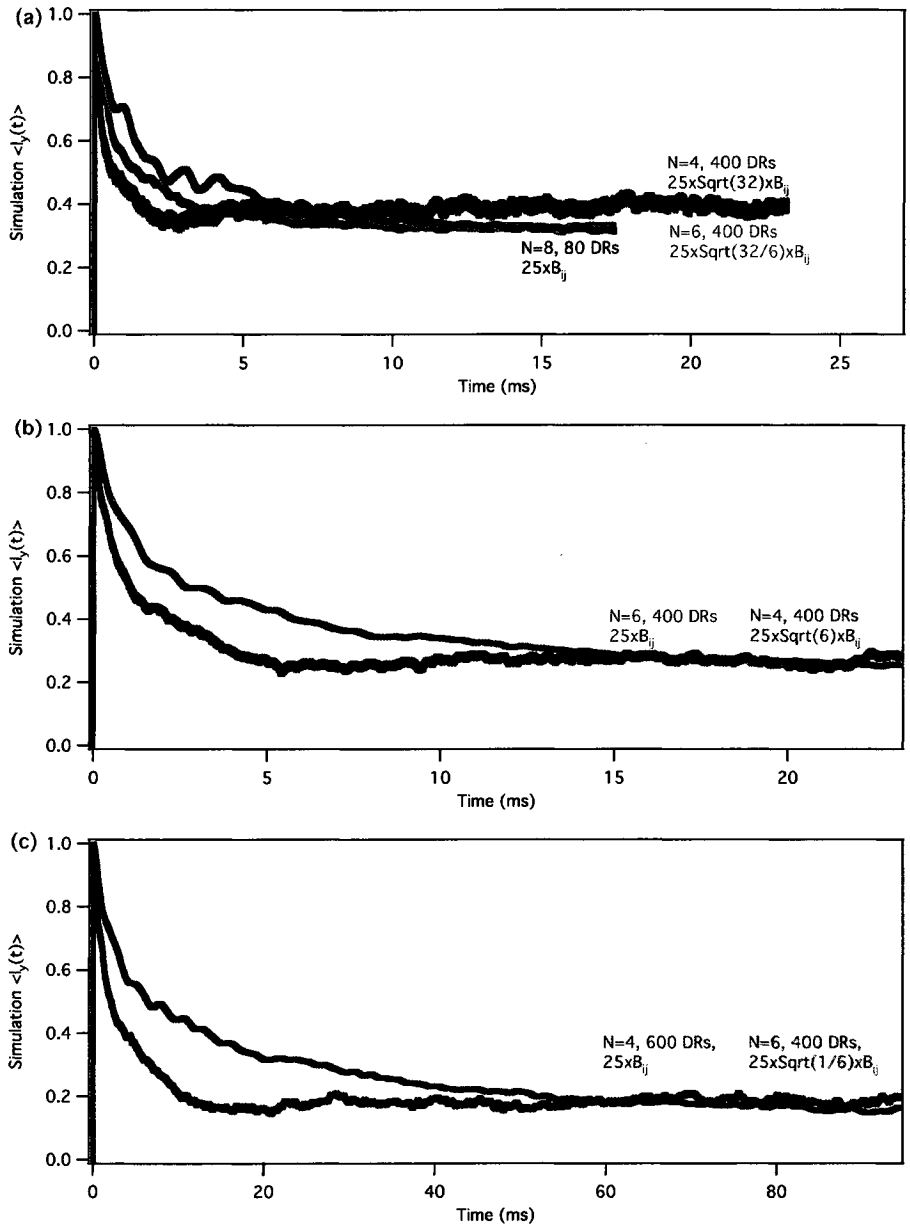

Figure 5.11: The exact simulations of CPMG with $25 \times B_{ij}$ of ^{29}Si, $\Omega_z = 0$, $\omega_1/2\pi$=40 kHz, τ=1 μs, and (a) N=8 (black), (b) N=6 (red), and (c) N=4 (blue). Exact simulations that adjust both N and the B_{ij} scale simultaneously, to keep $||\mathcal{H}_{zz}||^2 \equiv Tr\{\mathcal{H}_{zz}^{\dagger}\mathcal{H}_{zz}\}$ the same, result in a very similar tail height even though the initial decay is quite different (the green and orange curves, 400 DRs each). We don't have a theory for this scaling, but it seems to work over the range that we can test in our simulations.

$\propto ||\mathcal{H}_{zz}||/||I_{z_T}||$ is not the same, which is why the initial decay of the curves in each panel of Figure 5.11 is different. Despite the clear differences at early times, the long tail height is in reasonable agreement for the curves shown in each panel of Figure 5.11. Currently we don't have a theory for this apparent scaling rule. The range of parameters used in the figure is $4 \leq N \leq 8$, and a dipolar coupling strength between 10 and 140 times that of ^{29}Si.

Please be reminded that there is a big difference between the simulations presented so far in this section and the simulations in the weak pulse limit discussed in Section 5.1. Here, the long CPMG echo tail is produced with strong pulses ($\omega_1/2\pi$=40 kHz), zero Zeeman shift ($\Omega_z = 0$), and inflated dipolar coupling constant (e.g. $25 \times B_{ij}$ of ^{29}Si). In this parameter regime the long-lived CPMG echo tail is due to the effect of $\mathcal{H}_{zz}$ during pulses. While in the weak pulse limit ($\omega_1/2\pi$=8.5 kHz), large Zeeman shift (Ω_z=2.5 kHz) and regular dipolar coupling strength ($1\times B_{ij}$ of ^{29}Si) were used. So in that scenario, the CPMG echo tail is caused by $\mathcal{H}_Z$ during the pulses.

With the inflated dipolar coupling strength and a reasonable Zeeman linewidth, the simulations can reproduce the PSS observed in experiments, as shown in Figure 5.12. Note that while the non-zero Zeeman spread is not needed to produce the long echo tail in CPMG, as shown in many of the previous simulations with $\Omega_z = 0$, the APCP simulation does need a non-zero Zeeman spread to show the echo tail. We will discuss this difference in the next Chapter.

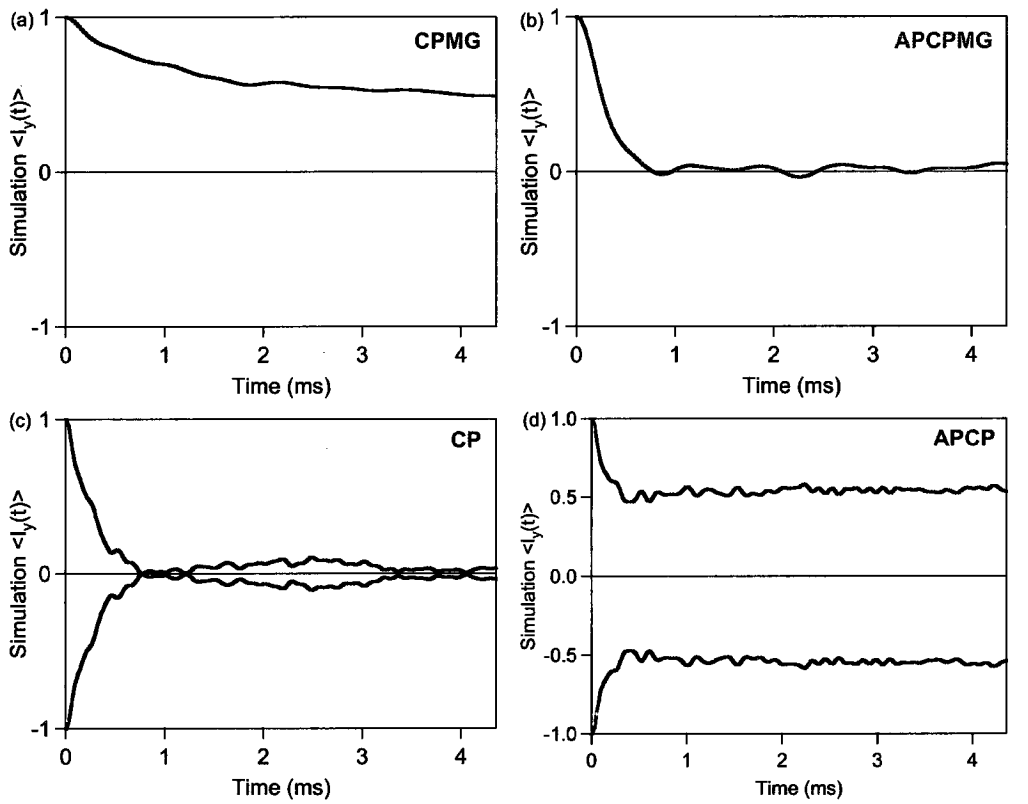

Figure 5.12: Exact simulations using strong but finite (with non-zero duration) π pulses. Simulations are done with N=6 spins, $\omega_1/2\pi = 40$ kHz, τ=1 μs, and $25 \times B_{ij}$ of ^{29}Si, Zeeman shift Ω_z/h drawn from a Gaussian distribution with FWHM=3 kHz for each DR, and averaged over 150 DRs. The full lineshape is 4 kHz, which is a convolution of the pure dipolar line of 2.2 kHz and the Zeeman spread of 3 kHz. These curves reproduce the results observed the experiments in Figure 5.4 that CPMG and APCP show a long-lived echo tail while CP and APCPMG decay quickly to zero.

Chapter 6

Average Hamiltonian Theory for Finite Pulses

In Chapter 5, we showed that the finite-pulse numerical simulations of CPMG could reproduce a long echo tail if we inflated the dipolar coupling above the value for Silicon. To understand the theoretical reason behind this result, we turned to Average Hamiltonian Theory (AHT) or coherent averaging theory [34, 35, 57, 60] to search for the effective Hamiltonian terms arising from the non-zero duration of pulses that may be responsible for the long-lived echo tail we observed in simulations. In this Chapter, we will first give a brief introduction to AHT, then apply AHT to the four pulse sequences discussed in the last two chapters, and finally we will show some interesting simulation results using AHT. This analytical approach is the basis for the advances presented in Chapter 8 and Chapter 9.

6.1 Introduction to Average Hamiltonian Theory

AHT is a systematic way to describe the net effect of a series of events, such as the repeating block of CPMG. The basic idea is that the state of the system at each

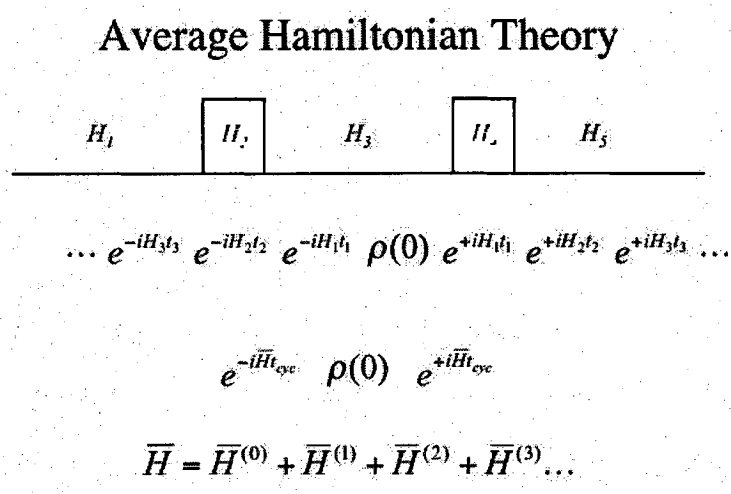

Figure 6.1: A simple demonstration of AHT.

cycle time t_c (not at other times within a cycle) can be described if we replace the cyclic, piecewise Hamiltonian terms by a single constant Hamiltonian, as illustrated in Figure 6.1. The general expression of density matrix $\rho(t)$ involves the product of time evolution operators for a series of piecewise events. In AHT, this product of time evolution operators is replaced by a single time evolution operator. However, the price to pay here is that the Hamiltonian in this single time evolution operator is an infinite sum of correction terms, $\bar{\mathcal{H}}^{(0)} + \bar{\mathcal{H}}^{(1)} + \bar{\mathcal{H}}^{(2)} \ldots$, derived from the Magnus expansion [53]. Fortunately, for our cyclic pulse sequences with the cycle duration t_c very short compared to T_2^* and T_2, keeping just the first few terms (usually $\bar{\mathcal{H}}^{(0)} + \bar{\mathcal{H}}^{(1)}$) is a good approximation [34, 35, 57, 60]. How do we calculate these average Hamiltonian

terms?

For the convenience of notation, we write the total Hamiltonian of a typical spin-$\frac{1}{2}$ system we have used in experiments as,

$$\mathcal{H}_{tot}(t) = \mathcal{H}_Z + \mathcal{H}_{zz} - \hbar\omega(t) I_{\phi_T}, \quad \omega(t) = \begin{cases} \omega_1 & : \text{ during a pulse along } \phi \\ 0 & : \text{ during free evolution} \end{cases} \tag{6.1}$$

Using the Dyson time-ordering operator T [81, 84], the total time-evolution operator can be written as [34, 35, 57, 60],

$$U_{tot}(t) = T\exp\left[-\frac{i}{\hbar}\int_0^t dt' \mathcal{H}_{tot}(t')\right] \tag{6.2}$$

U_{tot} can then be split into the product of two parts, the pulse part U_{rf} and the internal Hamiltonian part U_{int},

$$\begin{aligned} U_{tot}(t) &= U_{rf}(t) U_{int}(t) && (6.3)\\ U_{rf}(t) &= T\exp\left[-\frac{i}{\hbar}\int_0^t dt' \mathcal{H}_{rf}(t')\right] && (6.4)\\ U_{int}(t) &= T\exp\left[-\frac{i}{\hbar}\int_0^t dt' \widetilde{\mathcal{H}_{int}}(t')\right] && (6.5)\\ \widetilde{\mathcal{H}_{int}}(t) &= U_{rf}^{-1}(t) \mathcal{H}_{int} U_{rf}(t) && (6.6) \end{aligned}$$

where $\mathcal{H}_{int} = \mathcal{H}_Z + \mathcal{H}_{zz}$ as given in Equation (4.9), $\mathcal{H}_{rf} = -\hbar\omega(t) I_{\phi_T}$, and $\widetilde{\mathcal{H}_{int}}$ is the internal Hamiltonian in the toggling frame. For a cyclic sequence like CPMG, each cycle includes an overall $i \times 2\pi$ (i=1, 2, 3$\cdots$) rotation, which means $U_{rf}(n \cdot t_c) = 1$ with n being an integer number. The Magnus expansion [53] gives

$$U_{int}(nt_c) = \exp\left[-\frac{i}{\hbar} nt_c (\bar{\mathcal{H}}^{(0)} + \bar{\mathcal{H}}^{(1)} + \bar{\mathcal{H}}^{(2)} + \cdots)\right] \tag{6.7}$$

where the first two terms in the expansion are given by

$$\bar{\mathcal{H}}^{(0)} = \frac{1}{t_c}\int_0^{t_c} dt\widetilde{\mathcal{H}_{int}}(t) \tag{6.8}$$

$$\bar{\mathcal{H}}^{(1)} = -\frac{i}{2t_c\hbar}\int_0^{t_c} dt_2 \int_0^{t_2} dt_1[\widetilde{\mathcal{H}_{int}}(t_2), \widetilde{\mathcal{H}_{int}}(t_1)]. \tag{6.9}$$

Equation (6.7) shows that evaluation of $\bar{\mathcal{H}}^{(i)}$ in a single t_c enables one to describe the system's evolution at all subsequent $n \cdot t_c$ points.

6.2 Applying AHT to Multiple π Pulse Sequences

Now we will apply Equation 6.8 and Equation 6.9 to get $\bar{\mathcal{H}}^{(0)}$ and $\bar{\mathcal{H}}^{(1)}$ for CPMG, APCPMG, CP, and APCP.

The first step is to get $\widetilde{\mathcal{H}_{int}}(t)$ in the toggling frame. Note that we will set the time origin at right after the first tipping pulse 90_X and only consider the following cyclic events after 90_X. For CPMG, we can assign the five events within a cycle as $\mathcal{U}_1$, $\mathcal{P}_2$, $\mathcal{U}_3$, $\mathcal{P}_4$ and $\mathcal{U}_5$, where $\mathcal{U}$ indicates a free evolution period, while $\mathcal{P}$ indicates a pulse event. During $\mathcal{U}_1$,

$$\begin{aligned}\widetilde{\mathcal{H}_{int}}(t_1) &= \{U_{rf}^{-1}(t_1)\}\mathcal{H}_{int}\{inv\} \\ &= \mathcal{H}_Z + \mathcal{H}_{zz}\end{aligned} \tag{6.10}$$

since $U_{rf}^{-1}(t_1) = 1$ due to the fact that $\mathcal{U}_1$ is a free evolution period (i.e., ω_1=0).

For $\mathcal{P}_2$, the calculation is more complicated. To make this easier, we will first

rewrite $\mathcal{H}_{zz}$ as follows,

$$\begin{aligned}
\mathcal{H}_{zz} &= -\frac{1}{2}\mathcal{H}_{yy} - \frac{1}{2}\mathcal{H}_{yy} - \mathcal{H}_{xx} \\
&= -\frac{1}{2}\mathcal{H}_{yy} - \frac{1}{2}\sum_{i=1}^{N}\sum_{j>i}^{N} B_{ij}(3I_{y_i}I_{y_j} - \vec{I}_i\cdot\vec{I}_j) - \sum_{i=1}^{N}\sum_{j>i}^{N} B_{ij}(3I_{x_i}I_{x_j} - \vec{I}_i\cdot\vec{I}_j) \\
&= -\frac{1}{2}\mathcal{H}_{yy} - \sum_{i=1}^{N}\sum_{j>i}^{N} B_{ij}(\frac{3}{2}I_{y_i}I_{y_j} + 3I_{x_i}I_{x_j}) + \sum_{i=1}^{N}\sum_{j>i}^{N}\frac{3}{2}B_{ij}\vec{I}_i\cdot\vec{I}_j \\
&= -\frac{1}{2}\mathcal{H}_{yy} + \sum_{i=1}^{N}\sum_{j>i}^{N}\frac{3}{2}B_{ij}(I_{z_i}I_{z_j} - I_{x_i}I_{x_j}) \qquad (6.11)
\end{aligned}$$

where the first step is based on the relation $\mathcal{H}_{xx}+\mathcal{H}_{yy}+\mathcal{H}_{zz}=0$ [84]. Since $\widetilde{\mathcal{H}_{int}}(t_2) = \widetilde{\mathcal{H}_Z}(t_2) + \widetilde{\mathcal{H}_{zz}}(t_2)$, we will treat the Zeeman term and the dipolar term separately.

$$\begin{aligned}
\widetilde{\mathcal{H}_{zz}}(t_2) &= \{U_{rf}^{-1}(t_1)U_{rf}^{-1}(t_2)\}\mathcal{H}_{zz}\{inv\} \\
&= -\frac{1}{2}\mathcal{H}_{yy} + e^{-\frac{i}{\hbar}\omega_1 I_{y_T} t_2}\left(\sum_{i=1}^{N}\sum_{j>i}^{N}\frac{3}{2}B_{ij}(I_{z_i}I_{z_j} - I_{x_i}I_{x_j})\right)\{inv\} \\
&= -\frac{1}{2}\mathcal{H}_{yy} + \sum_{i=1}^{N}\sum_{j>i}^{N}\frac{3}{2}B_{ij}(I_{z_i}\cos\theta + I_{z_i}\sin\theta)(I_{z_j}\cos\theta + I_{z_j}\sin\theta) \\
&\quad -\sum_{i=1}^{N}\sum_{j>i}^{N}\frac{3}{2}(I_{x_i}\cos\theta - I_{z_i}\sin\theta)(I_{x_j}\cos\theta - I_{z_j}\sin\theta) \\
&= -\frac{1}{2}\mathcal{H}_{yy} + \mathcal{H}_y^S\cos 2\theta + \mathcal{H}_y^A\sin 2\theta \qquad (6.12)
\end{aligned}$$

where t_1 is integrated from 0 to τ (but $U_{rf}(t_1)$=1 due to the fact that event $\mathcal{U}_1$ is a free evolution), $\theta = \omega_1 t_2$ is the rotation angle along the Y-axis, and $\mathcal{H}_y^S$ and $\mathcal{H}_y^A$ are defined as following,

$$\mathcal{H}_y^S = \frac{3}{2}\sum_{i=1}^{N}\sum_{j>i}^{N} B_{ij}(I_{z_i}I_{z_j} - I_{x_i}I_{x_j}) \qquad (6.13)$$

$$\mathcal{H}_y^A = \frac{3}{2}\sum_{i=1}^{N}\sum_{j>i}^{N} B_{ij}(I_{x_i}I_{z_j} + I_{z_i}I_{x_j}) \qquad (6.14)$$

$\widetilde{\mathcal{H}_Z}(t_2)$ has a much simpler form,

$$\begin{aligned}\widetilde{\mathcal{H}_Z}(t_2) &= \{U_{rf}^{-1}(t_1)U_{rf}^{-1}(t_2)\}\mathcal{H}_Z\{inv\} \\ &= e^{-\frac{i}{\hbar}\omega_1 I_{y_T} t_2}\Omega_z I_{z_T}\{inv\} \\ &= \Omega_z(I_{z_T}\cos\theta + I_{x_T}\sin\theta) \end{aligned} \tag{6.15}$$

Therefore, the internal Hamiltonian in the toggling frame during $\mathcal{P}_2$ is,

$$\widetilde{\mathcal{H}_{int}}(t_2) = -\frac{1}{2}\mathcal{H}_{yy} + \mathcal{H}_y^S\cos 2\theta + \mathcal{H}_y^A\sin 2\theta + \Omega_z(I_{z_T}\cos\theta + I_{x_T}\sin\theta) \tag{6.16}$$

For event $\mathcal{U}_3$,

$$\begin{aligned}\widetilde{\mathcal{H}_{int}}(t_3) &= \{U_{rf}^{-1}(t_1)U_{rf}^{-1}(t_2)U_{rf}^{-1}(t_3)\}\mathcal{H}_{int}\{inv\} \\ &= \mathcal{R}_y^{-1}(\Omega_z I_{z_T} + \mathcal{H}_{zz})\mathcal{R}_y \\ &= -\Omega_z I_{z_T} + \mathcal{H}_{zz} \end{aligned} \tag{6.17}$$

where t_1 is integrated from 0 to τ, t_2 from 0 to t_p. Similarly, we can get $\widetilde{\mathcal{H}_{int}}(t_4)$ and $\widetilde{\mathcal{H}_{int}}(t_5)$ for CPMG. All the toggling frame Hamiltonian terms are listed in the following tables for CPMG, APCPMG, CP, and APCP. Here $\mathcal{H}_x^S$ and $\mathcal{H}_x^A$ are defined in a similar way as $\mathcal{H}_y^S$ and $\mathcal{H}_y^A$,

$$\mathcal{H}_x^S = \frac{3}{2}\sum_{i=1}^{N}\sum_{j>i}^{N} B_{ij}(I_{z_i}I_{z_j} - I_{y_i}I_{y_j}) \tag{6.18}$$

$$\mathcal{H}_x^A = \frac{3}{2}\sum_{i=1}^{N}\sum_{j>i}^{N} B_{ij}(I_{y_i}I_{z_j} + I_{z_i}I_{y_j}) \tag{6.19}$$

Event	Duration	$\widetilde{\mathcal{H}_{int}}(t_i)$ for CPMG
$\mathcal{U}_1$	τ	$+\Omega_z I_{z_T} + \mathcal{H}_{zz}$
$\mathcal{P}_2$	t_p	$+\Omega_z(I_{z_T}\cos\theta + I_{x_T}\sin\theta) - \frac{1}{2}\mathcal{H}_{yy} + \mathcal{H}_y^S\cos 2\theta + \mathcal{H}_y^A\sin 2\theta$
$\mathcal{U}_3$	2τ	$-\Omega_z I_{z_T} + \mathcal{H}_{zz}$
$\mathcal{P}_4$	t_p	$-\Omega_z(I_{z_T}\cos\theta + I_{x_T}\sin\theta) - \frac{1}{2}\mathcal{H}_{yy} + \mathcal{H}_y^S\cos 2\theta + \mathcal{H}_y^A\sin 2\theta$
$\mathcal{U}_5$	τ	$+\Omega_z I_{z_T} + \mathcal{H}_{zz}$

Table 6.1: Toggling frame Hamiltonians $\widetilde{\mathcal{H}_{int}}(t_i)$ during each event of the CPMG cycle $\{\tau - 180_Y - 2\tau - 180_Y - \tau\}$ where t_p is the pulse time, τ is the free evolution time, and $\theta = \omega_1 \cdot t_i$ (t_i is the time variable during pulse event $\mathcal{P}_i$).

Event	Duration	$\widetilde{\mathcal{H}_{int}}(t_i)$ for APCPMG
$\mathcal{U}_1$	τ	$+\Omega_z I_{z_T} - \mathcal{H}_{zz}$
$\mathcal{P}_2$	t_p	$+\Omega_z(I_{z_T}\cos\theta - I_{x_T}\sin\theta) - \frac{1}{2}\mathcal{H}_{yy} + \mathcal{H}_y^S\cos 2\theta + \mathcal{H}_y^A\sin 2\theta$
$\mathcal{U}_3$	2τ	$-\Omega_z I_{z_T} + \mathcal{H}_{zz}$
$\mathcal{P}_4$	t_p	$-\Omega_z(I_{z_T}\cos\theta + I_{x_T}\sin\theta) - \frac{1}{2}\mathcal{H}_{yy} + \mathcal{H}_y^S\cos 2\theta + \mathcal{H}_y^A\sin 2\theta$
$\mathcal{U}_5$	τ	$+\Omega_z I_{z_T} + \mathcal{H}_{zz}$

Table 6.2: Toggling frame Hamiltonians $\widetilde{\mathcal{H}_{int}}(t_i)$ during each event of the APCPMG cycle $\{\tau - 180_{-Y} - 2\tau - 180_Y - \tau\}$.

Event	Time	$\widetilde{\mathcal{H}_{int}}(t_i)$ for CP
$\mathcal{U}_1$	τ	$+\Omega_z I_{z_T} + \mathcal{H}_{zz}$
$\mathcal{P}_2$	t_p	$+\Omega_z(I_{z_T}\cos\theta - I_{y_T}\sin\theta) - \frac{1}{2}\mathcal{H}_{xx} + \mathcal{H}_x^S\cos 2\theta - \mathcal{H}_x^A\sin 2\theta$
$\mathcal{U}_3$	2τ	$-\Omega_z I_{z_T} + \mathcal{H}_{zz}$
$\mathcal{P}_4$	t_p	$-\Omega_z(I_{z_T}\cos\theta - I_{y_T}\sin\theta) - \frac{1}{2}\mathcal{H}_{xx} + \mathcal{H}_x^S\cos 2\theta - \mathcal{H}_x^A\sin 2\theta$
$\mathcal{U}_5$	τ	$+\Omega_z I_{z_T} + \mathcal{H}_{zz}$

Table 6.3: Toggling frame Hamiltonians $\widetilde{\mathcal{H}_{int}}(t_i)$ during each event of the CP cycle $\{\tau - 180_X - 2\tau - 180_X - \tau\}$.

Event	Time	$\widetilde{\mathcal{H}_{int}}(t_i)$ for APCP
$\mathcal{U}_1$	τ	$+\Omega_z I_{z_T} + \mathcal{H}_{zz}$
$\mathcal{P}_2$	t_p	$+\Omega_z(I_{z_T}\cos\theta + I_{y_T}\sin\theta) - \frac{1}{2}\mathcal{H}_{xx} + \mathcal{H}_x^S\cos 2\theta + \mathcal{H}_x^A\sin 2\theta$
$\mathcal{U}_3$	2τ	$-\Omega_z I_{z_T} + \mathcal{H}_{zz}$
$\mathcal{P}_4$	t_p	$-\Omega_z(I_{z_T}\cos\theta - I_{y_T}\sin\theta) - \frac{1}{2}\mathcal{H}_{xx} + \mathcal{H}_x^S\cos 2\theta - \mathcal{H}_x^A\sin 2\theta$
$\mathcal{U}_5$	τ	$+\Omega_z I_{z_T} + \mathcal{H}_{zz}$

Table 6.4: Toggling frame Hamiltonians $\widetilde{\mathcal{H}_{int}}(t_i)$ during each event of the APCP cycle $\{\tau - 180_{-X} - 2\tau - 180_X - \tau\}$.

Note that $\mathcal{U}_1$, $\mathcal{U}_3$, and $\mathcal{U}_5$ are identical for all four sequences. The difference among them is entirely due to the toggling frame Hamiltonian during the pulses $\mathcal{P}_2$ and $\mathcal{P}_4$. Having all the $\widetilde{\mathcal{H}_{int}}(t_i)$ at hand, now we can now use Equation (6.8) and Equation (6.9) to calculate the first two average Hamiltonian terms,

CPMG:

$$\bar{\mathcal{H}}^{(0)} = \frac{1}{t_c}(4\tau\mathcal{H}_{zz} - t_p\mathcal{H}_{yy}) \tag{6.20}$$

$$\begin{aligned}\bar{\mathcal{H}}^{(1)} = {} & \frac{-i}{2t_c\hbar}\frac{t_p}{\pi}\Big(t_p[\mathcal{H}_y^A, \mathcal{H}_y^S + \mathcal{H}_{yy}] \\ & +(8\tau + 2t_p)[\Omega_z I_{x_T}, \Omega_z I_{z_T} + \mathcal{H}_{yy}]\Big)\end{aligned} \tag{6.21}$$

APCPMG:

$$\bar{\mathcal{H}}^{(0)} = \frac{1}{t_c}(4\tau\mathcal{H}_{zz} - t_p\mathcal{H}_{yy} - \frac{4\Omega_z t_p}{\pi}I_{x_T}) \tag{6.22}$$

$$\bar{\mathcal{H}}^{(1)} = 0 \tag{6.23}$$

CP:

$$\bar{\mathcal{H}}^{(0)} = \frac{1}{t_c}(4\tau\mathcal{H}_{zz} - t_p\mathcal{H}_{xx}) \tag{6.24}$$

$$\begin{aligned}\bar{\mathcal{H}}^{(1)} = {} & \frac{+i}{2t_c\hbar}\frac{t_p}{\pi}\Big(t_p[\mathcal{H}_x^A, \mathcal{H}_x^S + \mathcal{H}_{xx}] \\ & +(8\tau + 2t_p)[\Omega_z I_{y_T}, \Omega_z I_{z_T} + \mathcal{H}_{xx}]\Big)\end{aligned} \tag{6.25}$$

APCP:

$$\bar{\mathcal{H}}^{(0)} = \frac{1}{t_c}(4\tau\mathcal{H}_{zz} - t_p\mathcal{H}_{xx} + \frac{4\Omega_z t_p}{\pi}I_{y_T}) \quad (6.26)$$

$$\bar{\mathcal{H}}^{(1)} = 0 \quad (6.27)$$

Note that for "symmetric" pulse sequences like APCPMG and APCP, all the odd number average Hamiltonian terms ($\bar{\mathcal{H}}^{(1)}$, $\bar{\mathcal{H}}^{(3)}\ldots$) are zero [34, 35, 57, 60]. Terms involving the pulse duration t_p arise from the finite pulses, and are absent in the δ-pulse approximation. From the above average Hamiltonian expressions, we can see that the non-zero duration of pulses introduces terms that are unique to each pulse sequence.

6.3 Simulations with Average Hamiltonian Terms

We can now use these average Hamiltonian terms in simulations to study the effects arising from the non-zero duration of pulses. In the δ-pulse approximation, the full average Hamiltonian $\bar{\mathcal{H}}$ of CPMG, APCPMG, CP, and APCP is just $\mathcal{H}_{zz}$, valid to all orders (which can be verified by taking $t_p \rightarrow 0$ in Equation (6.20) - Equation (6.27)). However, when taking into account the non-zero duration of π pulses, terms other than $\mathcal{H}_{zz}$ and $\mathcal{H}_Z$ appear in $\bar{\mathcal{H}}^{(0)}$ and $\bar{\mathcal{H}}^{(1)}$. Furthermore, in the conventional way of developing a new pulse sequence, understanding $\bar{\mathcal{H}}^{(0)}$ is often enough. However, our simulations show that for multiple-π-pulse sequences, keeping $\bar{\mathcal{H}}^{(0)}$ alone may not be good enough to predict the spin echo behavior.

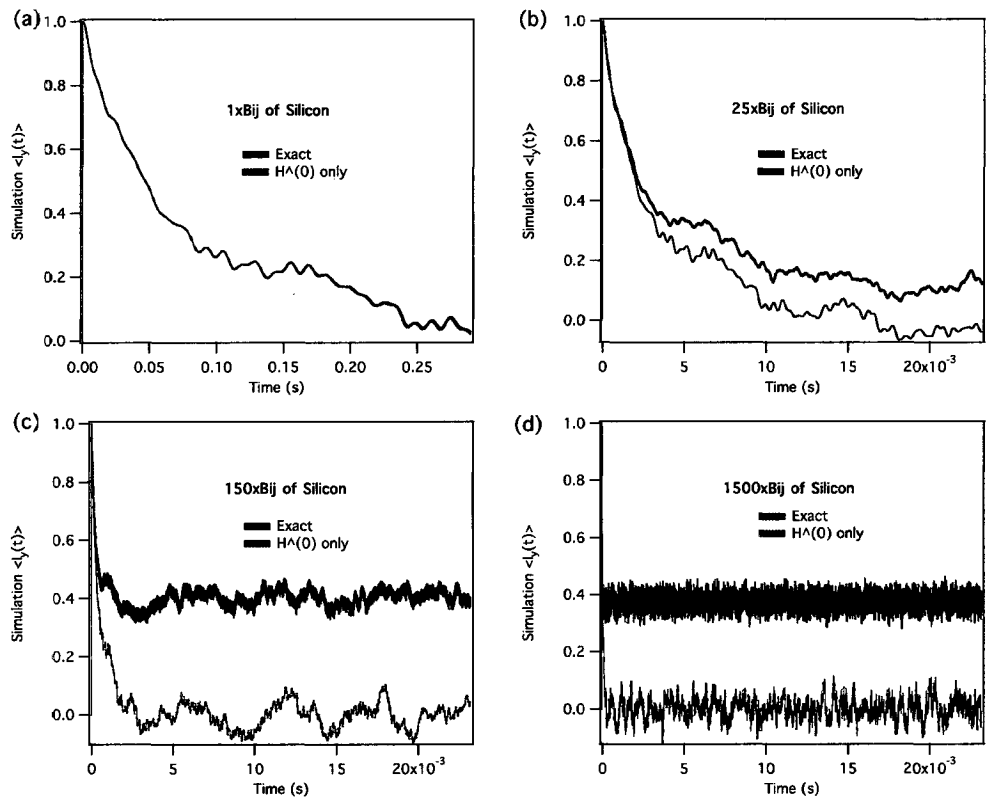

Figure 6.2: As the B_{ij} scale is increased, exact CPMG calculations (blue) separate from the approximate calculations using just $\bar{\mathcal{H}}^{(0)}_{\mathrm{CPMG}}$ (red). All simulations use $\Omega_z = 0$, $\omega_1/2\pi = 40$ kHz, τ=1 μs, and averaged over 100 DRs of N=4 spins on a Silicon lattice.

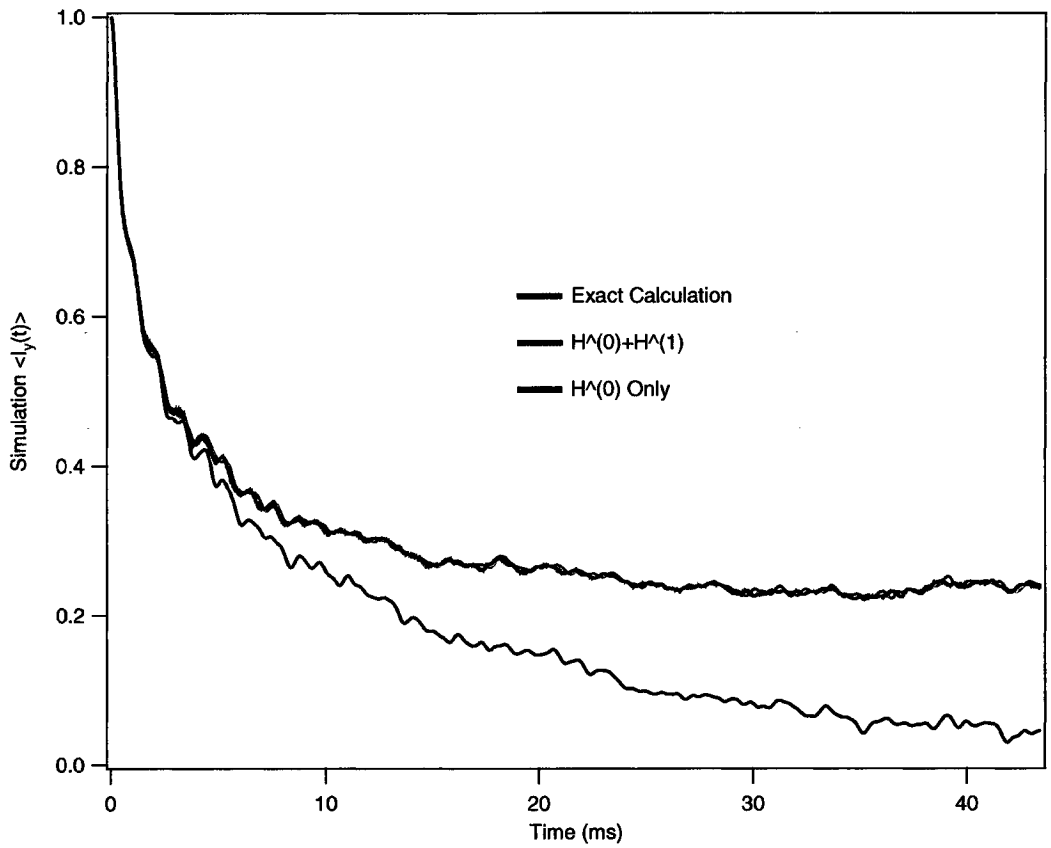

Figure 6.3: Comparison of the exact simulation and the average Hamiltonian simulations. $\bar{\mathcal{H}}^{(0)} + \bar{\mathcal{H}}^{(1)}$ produces a CPMG long echo tail (blue) that is almost identical to that of the exact simulation (red), while $\bar{\mathcal{H}}^{(0)}$-only simulation (black) decays toward zero. All simulations use $\Omega_z = 0$, $\frac{\omega_1}{2\pi} = 40$ kHz, τ=1 μs, and averaged over 200 DRs of N=6 spins on a Silicon lattice with $25 \times B_{ij}$ of ^{29}Si.

Figure 6.2 shows the comparison of the finite-pulse simulations using the exact Hamiltonian and $\bar{\mathcal{H}}^{(0)}$ only, as the dipolar coupling strength is varied. When the realistic ^{29}Si dipolar coupling constant is used, these two simulation methods show very little difference. However, as the dipolar coupling strength is increased, the difference between the two calculations becomes more pronounced. The exact calculation gives a long echo tail, and the echo tail height increases with the dipolar coupling strength until it saturates with $\sim 150 \times B_{ij}$ of ^{29}Si. This increasing difference between the exact simulation and $\bar{\mathcal{H}}^{(0)}$-only simulation clearly shows that $\bar{\mathcal{H}}^{(1)}$ and higher order terms are major contributors to the long echo tail observed in the exact simulations with inflated dipolar coupling. On the other hand, as it shows in Figure 6.3 that the simulation using $\bar{\mathcal{H}}^{(0)} + \bar{\mathcal{H}}^{(1)}$ is almost identical to the exact calculation, suggesting that $\bar{\mathcal{H}}^{(2)}$, $\bar{\mathcal{H}}^{(3)}$ etc. are not required for the long echo tail in this parameter regime (inflated dipolar coupling and finite pulses).

Surprisingly, even when only $\bar{\mathcal{H}}^{0}$ is included, the average Hamiltonian simulations of CPMG show a dependence on the spin number N, just as the exact simulations described in Chapter 5. As shown in Figure 6.4, the CPMG curve of a 6-spin system decays slower that of a 4-spin system, both using dipolar coupling strength $25 \times B_{ij}$ of ^{29}Si.

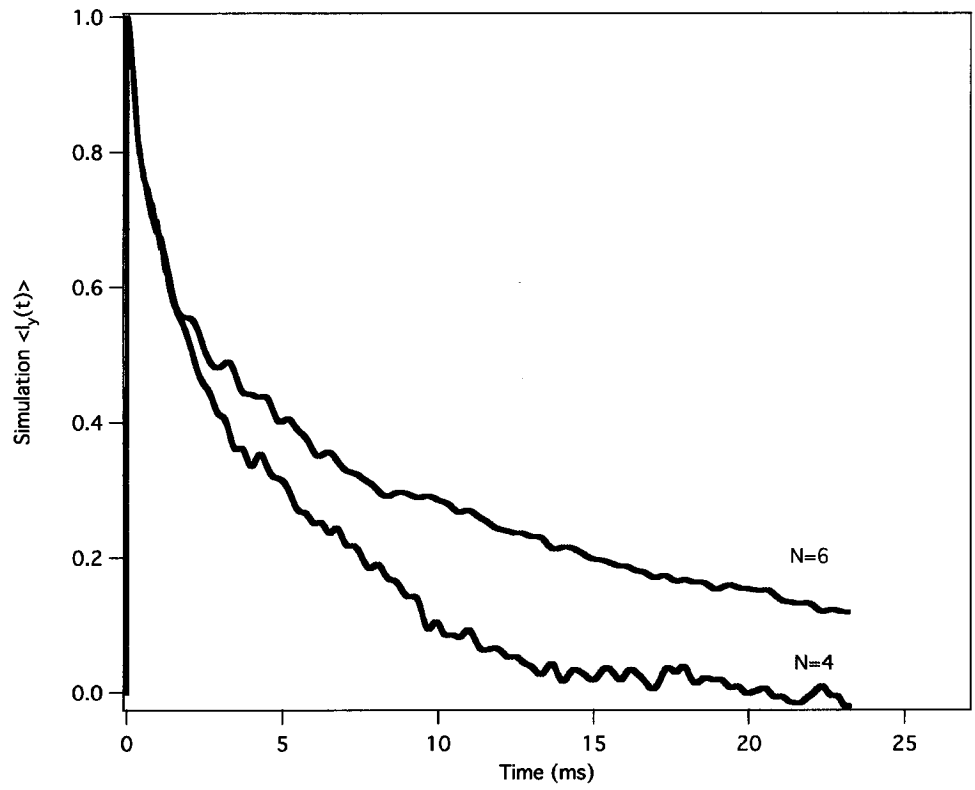

Figure 6.4: Approximate CPMG simulations for N=4 and N=6 using just $\bar{\mathcal{H}}^{(0)}_{\mathrm{CPMG}}$, and $25 \times B_{ij}$ of ^{29}Si. All simulations use $\Omega_z = 0$, $\frac{\omega_1}{2\pi} = 40$ kHz, τ=1 μs, and averaged over 400 DRs on a Silicon lattice. While they agree at early times, the approach to zero is more gradual for larger N.

6.4 More Complicated Pulse Sequences

By just looking at the pulse sequence itself, it is very hard, if not impossible, to decide which one gives a long echo tail, which does not. With the help of the leading order average Hamiltonian, we can make very useful predictions. A big difference for APCPMG and CPMG is that $\bar{\mathcal{H}}^{(1)}_{\text{APCPMG}} = 0$ while $\bar{\mathcal{H}}^{(1)}_{\text{CPMG}} \neq 0$. For CPMG, the nonzero $\bar{\mathcal{H}}^{(1)}$ plays an important role in producing the long-lived echo tail. Based on this idea, we construct two much more complicated pulse sequences, as shown in Figure 6.5, in analogy of CPMG and APCPMG. Type 1 pulse sequence has π_Y pulses inserted between two APCPMG blocks, while type 2 has alternating π_Y and π_{-Y} inserted. These two pulse sequences only have one π pulse out of ten that is different from each other. Applying average Hamiltonian theory reveals that Type 1 sequence has a non-zero $\bar{\mathcal{H}}^{(1)}$, like CPMG; while the "symmetric" [60] Type 2 sequence has $\bar{\mathcal{H}}^{(1)} = 0$, like APCPMG. Based on our results of CPMG and APCPMG, we proposed that Type 1 sequence would give a long echo tail, while Type 2 would not. Both our experiments and simulations (Figure 6.6) confirmed this prediction. These two pulse sequences also serve as a proof that our experimental observation of the long echo tail is not due to pulse imperfections. The pulse imperfections will be very similar for sequence Type 1 and Type 2 since they have 9 out of 10 pulses that are exactly the same, and it is hard to see how the imperfection of just one pulse out of ten can be responsible for the difference observed in experiments.

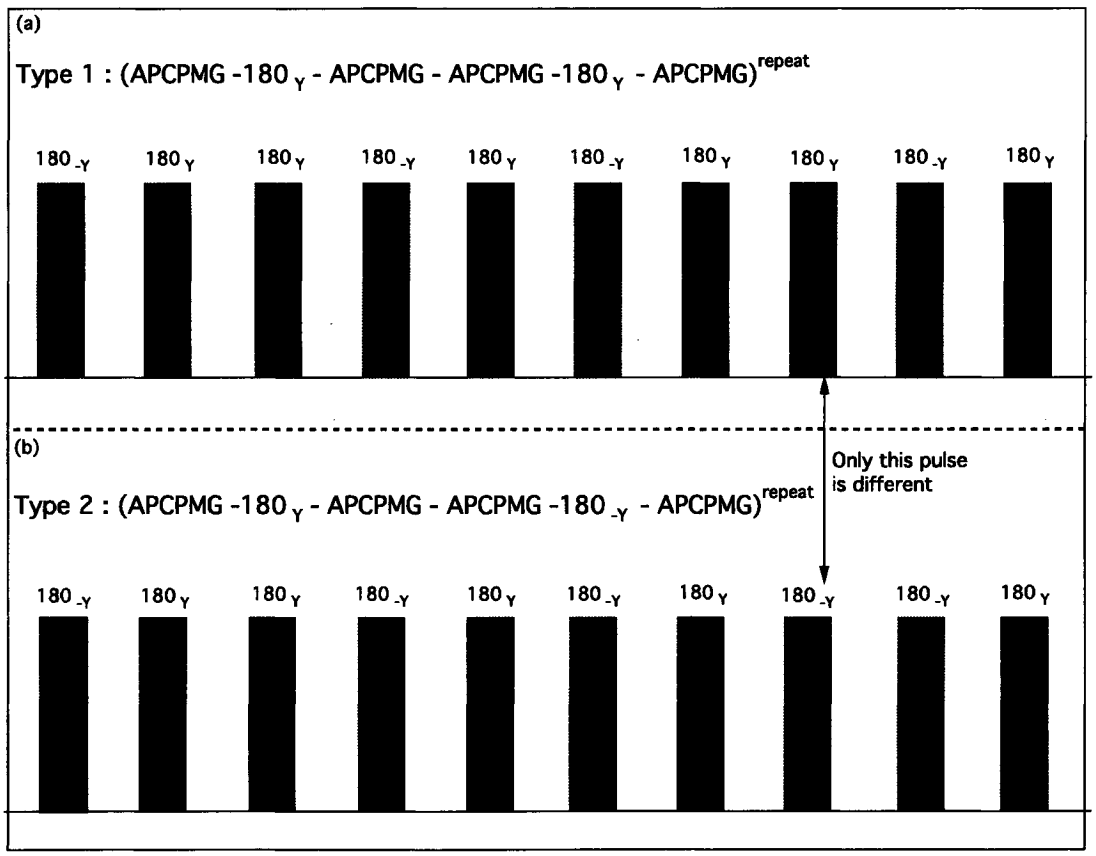

Figure 6.5: Simulations and experiments shown in Figure 6.6 use a repeating π-pulse cycle Type 1 (a) and Type 2 (b), where the building block APCPMG = $\{\tau\text{-}180_{-Y}\text{-}2\tau\text{-}180_{+Y}\text{-}\tau\}$. The only difference between these two pulse sequences is the $+Y$ (red) or $-Y$ (blue) phase choice in just one out of ten pulses in the repeating block.

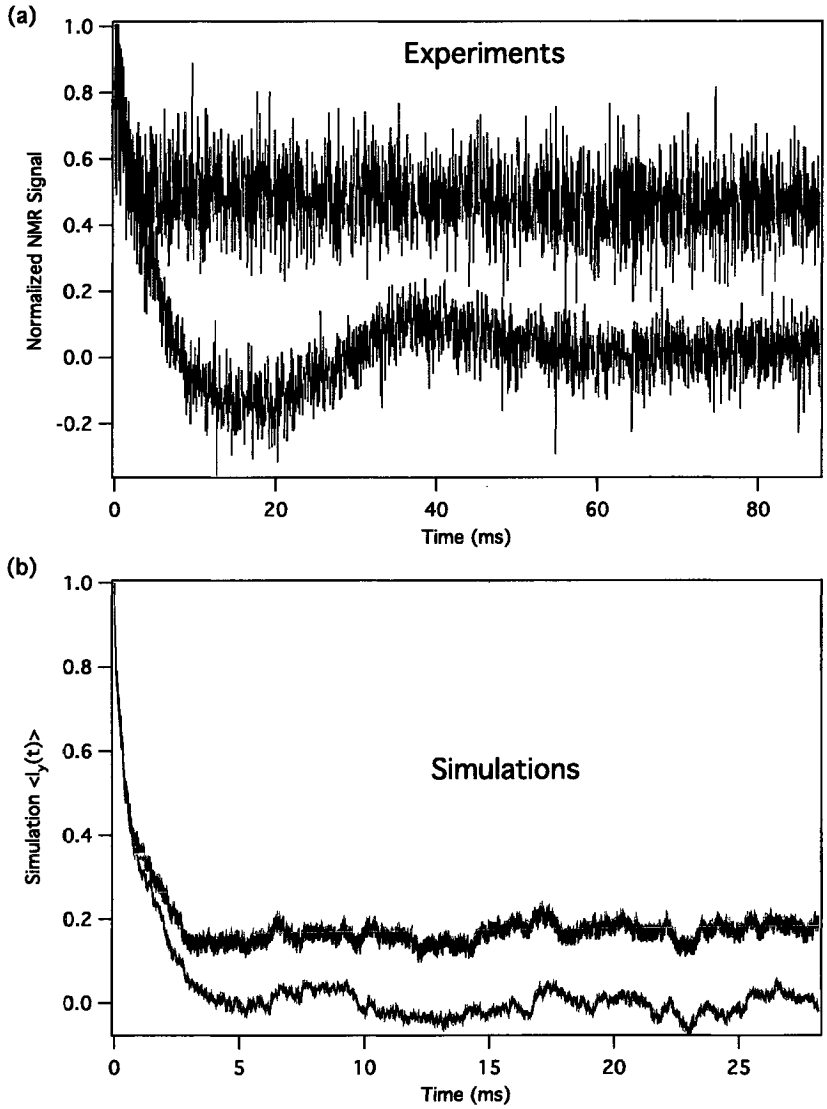

Figure 6.6: (a) Experiments on a small sample of Si:Sb (10^{17} Sb/cm^3), using the repeating π-pulse cycles defined in Figure 6.5, with $\omega_1/2\pi$ = 40 kHz and τ=36 μs. (b) Simulations using the repeating π-pulse cycles defined in Figure 6.5, with N=4 spins, $\omega_1/2\pi$ = 40 kHz, τ=1 μs, Ω_z = 0, 100 DRs, and for 125 $\times$ B_{ij} of ^{29}Si. In both experiments and simulations, the sequence 90_X-$\{\text{Type 1}\}^{repeat}$ (red) produces a long echo tail, while 90_X-$\{\text{Type 2}\}^{repeat}$ (blue) does not.

Chapter 7

Extra Coherence Pathways

In Chapter 5, our exact numerical simulations showed that the non-zero duration of π pulses was non-negligible and it could be responsible for the PSS observed in experiments. In Chapter 6, we calculated the leading order terms of the average Hamiltonian ($\bar{\mathcal{H}}^{(0)}$ and $\bar{\mathcal{H}}^{(1)}$) for the four pulse sequences used in our experiments, and showed that the non-zero pulse duration introduced new effective Hamiltonian terms that were not in the δ-pulse approximation. In this Chapter, we will investigate the effects of those new terms introduced by the non-zero pulse duration.

To facilitate our discussion, let us first introduce the notation of quantum coherence (QC) levels in a density matrix [84]. For the following density matrix element,

$$\langle M'\alpha', \mid \rho(t) \mid M, \alpha\rangle, \quad \text{and} \quad I_{z_T} \mid M, \alpha\rangle = M \mid M, \alpha\rangle$$

where α represents all other quantum numbers needed to describe the quantum state [81]), it is called p-order QC with $p = M' - M$. Figure 7.1 (a) shows the example of a 2-spin, $2^2 \times 2^2$ density matrix with all QC orders identified, and Figure 7.1 (b) shows all the $p = \pm 1$ QC elements in a 6-spin, $2^6 \times 2^6$ density matrix. Since the NMR

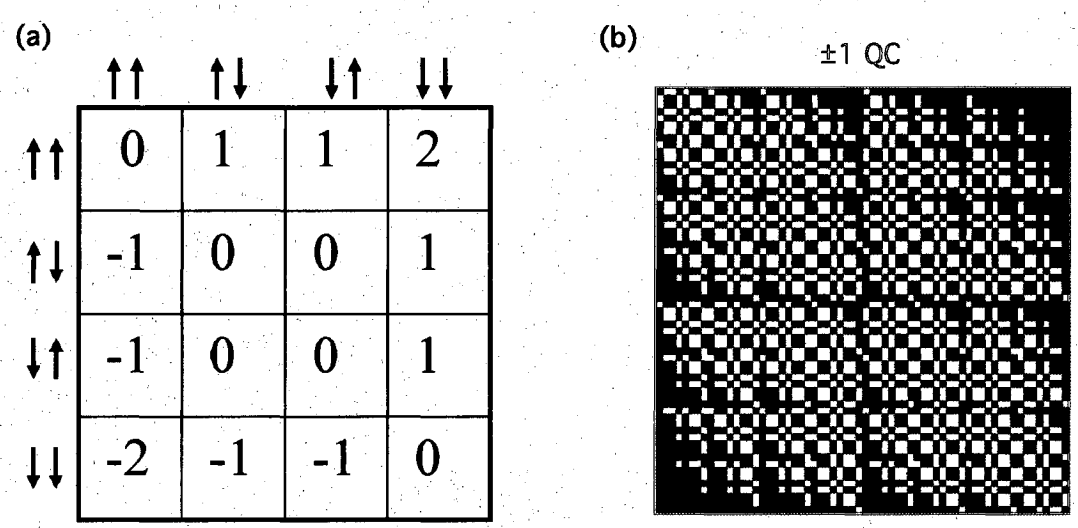

Figure 7.1: (a) QC levels in a 2-spin density matrix in I_z basis. (b) All the ± 1 QC elements (red) in a 6-spin 64×64 density matrix in I_z basis.

signal that we actually measure is given by $Tr\{I_{y_T}\rho\}$, only one-spin, $p = \pm 1$QC cells in the density matrix are directly measurable [84]. For example, the one-spin term I_1^+ is a measurable $p = +1$QC, while the three-spin term $I_1^+ I_2^- I_3^+$ is not (it is still $p = +1$QC, but not measurable) .

In the δ-pulse approximation, the Hamiltonian of our homonuclear dipolar sample is the sum of $\mathcal{H}_{zz}$ and $\mathcal{H}_Z$, both are composed of purely zeroth order quantum operators [84]. Treating the very first $\frac{\pi}{2}$ tipping pulse as an instantaneous rotation, the initial density matrix of the system is I_{y_T} in the high temperature and high field approximation [60, 84]. The matrix representation of I_{y_T} has nonzero cells only in the observable ± 1 QC levels [84]. In between pulses, the zeroth quantum operator in $\mathcal{H}_{int}$ does not change the coherence levels. Furthermore, in the δ-pulse approximation

a π pulse flips the QC $p \rightarrow -p$. So within this approximation, the CPMG sequence should result in coherence flow that is restricted within ± 1 QC levels. However, when the non-zero duration of the π pulses is taken into account, Hamiltonian terms with non-zeroth order quantum operators are introduced, and the coherence is no longer restricted within ± 1 QC levels in the density matrix.

7.1 The Weak Pulse Limit with Big Ω_z

As discussed in Section 5.1 in Chapter 5, the simulations using a big Ω_z relative to the pulse strength and a short τ give a long echo tail in CPMG. Because of the big Ω_z during the finite pulses, an intended 180° rotation about the Y-axis is no longer perfect and will leave the magnetization partially along the Z-axis. Therefore, coherence starting as I_{y_T}, an observable ± 1 QC, will partially change to I_{z_T}, an zero QC, as each π pulse is applied. If these zero QC cells act as pure signal "sinks," and do not contribute to the signal in any way, then this effect should simply make the echo tail height decrease as more and more observable ± 1 QC is lost to zero QC. Instead, CPMG signal refuses to decay after many π pulses, which suggests that the coherence that gets pumped to zero QC during π pulses is not getting lost. On the contrary, it seems to flow back to the measurable ± 1 cells and contribute constructively to the signal.

To see if we could understand how the details of complicated coherence pathways resulted in NMR observable signal, we designed and implemented so-called knock-out

simulations. The term knock-out is based on knock-out mice in which one or more genes are turned off to see the effects. In our knock-out simulations, we set certain QC cells to be zero at certain time in the evolution of $\rho(t)$ and look for the effects in $< I_{y_1}(t) >$. If the QC cells being zeroed are not involved in the coherence transfer pathways that contribute to the measured signal, then the knock-out manipulation should not affect the signal.

Our simulations show that in this weak pulse limit, zero QC cells play a particularly important role in the long-lived echo tail of CPMG (Figure 7.2). When all the ± 2 QC cells are set to zero after each π pulse, there is barely any change in the tail height compared to the full calculation without knock-out manipulation. This indicates that ± 2 QC cells are not actively involved in the quantum coherence pathways that contribute to the signal. However, when all the zero QC cells are knocked out in the same manner, a dramatic drop in the tail height is observed, indicating the particularly important role of zero QC cells in the quantum coherence pathways that result in the measured signal. When only ± 1 is left untouched and all other QC cells (including $0, \pm 2, \pm 3, \pm 4, \pm 5$, and ± 6) are zeroed after each π pulse, the CPMG tail decays to zero. The last knock-out case is in a way mimicking the δ-pulse approximation, in which case, all the QC cells other than ± 1 will remain zero all the time.

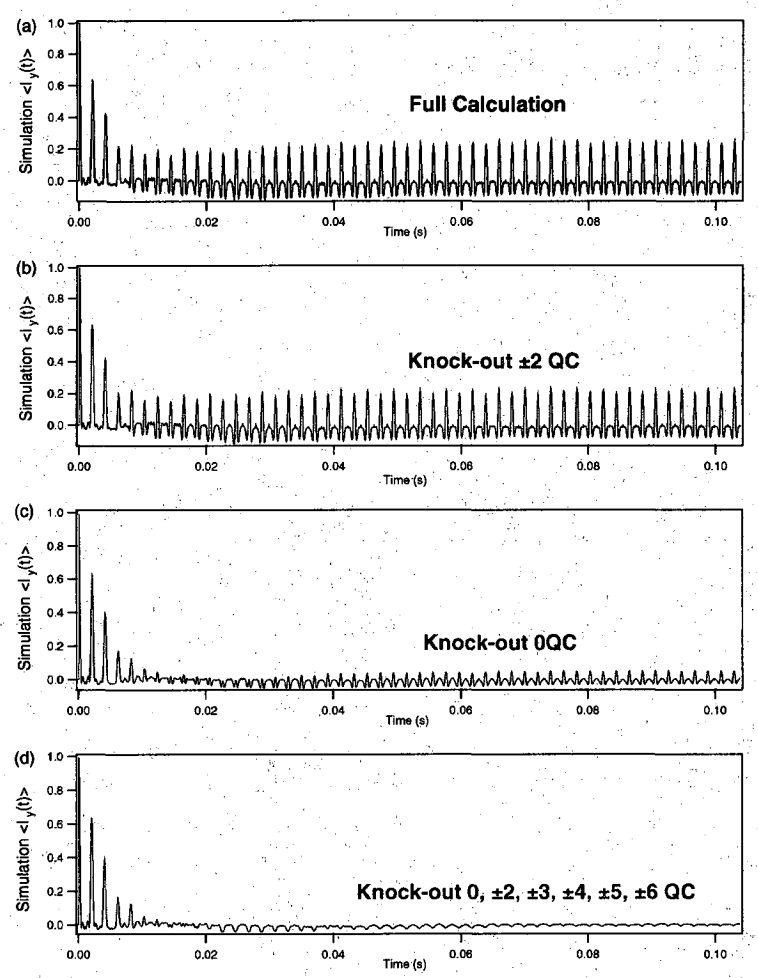

Figure 7.2: CPMG simulations using N=6, $\omega_1/2\pi$ = 8.5kHz, $\Omega_z/2\pi$ = 2.5kHz, τ=1ms, and averaged over 400 DRs. The full, exact calculation (black) exhibits a pronounced long tail. For each "knock-out" curve, the density matrix cells corresponding to the p-quantum coherence have been artificially set to zero after each π pulse of the exact simulation. Knocking out all ± 2 QC shows little influence in the CPMG tail height (b), while knocking out all 0 QC leads to a dramatic drop in the tail height(c). The curve in (d) shows that the coherence transfer pathways that involve ONLY p=± 1 cells do not make an important contribution to the long echo tail found the in the full, exact calculation.

7.2 The Strong Pulse Limit with Inflated Dipolar Coupling

In the simulations with strong but finite pulses and inflated dipolar couplings (with $\Omega_z = 0$), there are also extra coherence pathways that are not found in the δ-pulse approximation. However, these extra coherence pathways are different from those in the weak pulse limit with big Ω_z. Even with $\Omega_z = 0$, there are non-zeroth order quantum operators in the leading average Hamiltonian terms as long as the non-zero duration of pulses is taken into account. These non-zeroth order QC operators enable the coherence flow between ± 1 and all other coherence levels [60, 84]. We can gain some insight of these non-zeroth order QC operators from the average Hamiltonian $\bar{\mathcal{H}}^{(1)}$. For example, $[\mathcal{H}_y^A, \mathcal{H}_y^S]$ contains ± 1 QC operators, which can pump coherence from $+1$ to 0 and $+2$, from $+2$ to $+1$ and $+3$, and so on. As we show below, unlike in the weak pulse limit, the extra coherence pathways involved in this scenario are no longer restricted to mainly zero QC, but can involve all QC levels. What is amazing about these complicated extra coherence pathways is that so much of the coherence pumped to 0, ± 2, etc., manages to flow back to measurable ± 1 and contributes constructively to the signal [48].

Again, this point can be demonstrated using our knock-out manipulations of the density matrix. As shown in Figure 7.3, when all the ± 2 cells are set to zero after each π pulse, the tail height drops by about 50%, indicating the important role of $p = \pm 2$ in the coherence pathways contributing to the measured signal. In this strong

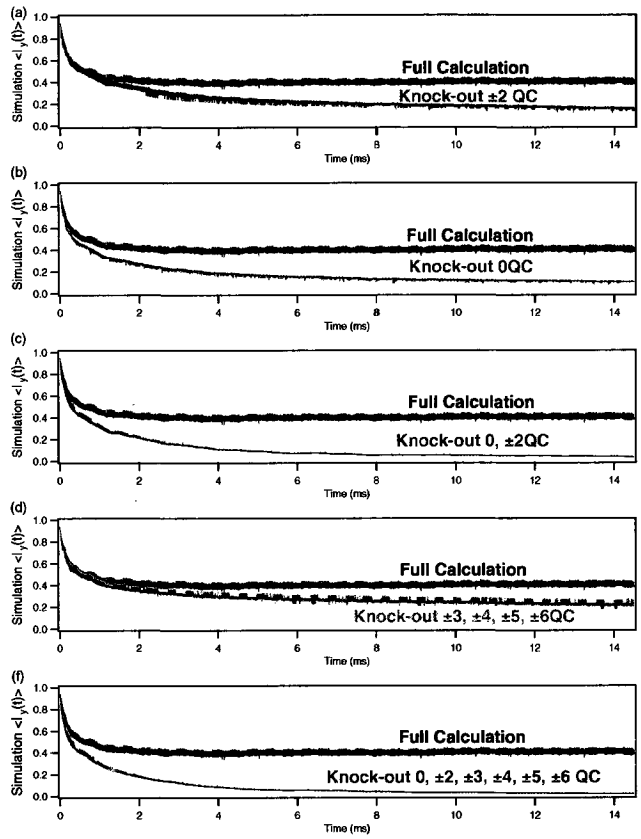

Figure 7.3: CPMG simulations using N=6, $\Omega_z = 0$, $\omega_1/2\pi$=40 kHz, τ=1 μs, 400 DRs, and 150 $\times$ B_{ij} of ^{29}Si. The full, exact π pulse calculation (black) exhibits a pronounced long echo tail. Knocking out ± 2 QC (a) results in a drop in echo tail height, and knocking out 0 QC (b) gives an even lower echo tail. When both 0 and ± 2 QC cells are knocked out (c), the echo tail goes to close to zero. (d) shows that even the higher order QC cells, $\pm 3, \pm 4, \ldots$, contribute to the signal. The red curve in the bottom panel (e) shows that the coherence transfer pathways involving ONLY $p = \pm 1$ cells do not make an important contribution to the long tail found the in the full, exact calculation.

pulse limit, the role of higher QC levels, such as ± 2, ± 3, is different from that in the weak pulse limit. For example, we've already seen in Figure 7.2 that ± 2 QC levels are not important to the measured signal in the weak pulse limit. Figure 7.3 shows that this is clearly no longer true in the case of strong pulses with inflated dipolar coupling strength. Furthermore, in the strong pulse limit, even $\pm 3, \pm 4, \pm 5, \pm 6$ have non-negligible roles. When these QC cells are all zeroed after each π pulse, there is a drop in the signal (Figure7.3 (d)). The zero QC elements are still important, as indicated by a more than 50% decrease of tail height in the knock-out curve. By zeroing all the 0 and ± 2 QC cells all together, the CPMG tail is brought to close to zero, and knocking out all but ± 1 makes the tail even closer to zero.

At first glance, the dynamics in $\rho(t)$ allowed by the extra quantum coherence pathways may seem to be inconsistent with the "static" long tail observed in CPMG. We propose a handwaving way to think about the coherence pathways. The measured signal in the simulations is determined by two types of pathways–outflow pathways that let QC flow out of observable ± 1 levels, and inflow pathways that let QC flow back into observable ± 1. The rather smooth and constant CPMG tail of the full calculation seems to suggest a balance between the inflow and outflow.

Another type of density manipulation seems to support this inflow-outflow picture. Instead of knocking out certain QC cells after each π pulse, we can instead manipulate $\rho(t)$ only once, after a certain π pulse. In Figure 7.4, all the ± 1 cells are either set to zero or uniformly increased to 1.5 times of their original values, right after the

300^{th} π pulse. When all the ± 1 cells are set to zero, the signal goes straight to zero because there is nothing left to measure (only measurable ± 1 QC cells contribute to the measured signal). At the same time, the outflow from ± 1 should also be zero because there is no coherence left in ± 1 to provide the flow. On the other hand, the inflow should still be present. As more and more coherence flow back into ± 1, the measured signal starts to build up. After a while the rate of inflow should decrease since the coherence stored in $0, \pm 2, \pm 3$, etc., becomes fewer as it flows back to ± 1. Meanwhile, as the coherence builds up on ± 1 levels, the outflow from ± 1 begins to increase, which serves to increase the coherence on 0, ± 2, ± 3 etc. At some point, a new balance between the inflow and outflow may be reached, giving a rather constant signal tail at a lower height. Similar analysis can be applied to the second case when ± 1 cells are uniformly increased 1.5 times after the 300^{th} π pulse. Right after the density manipulation, the signal is increased 1.5 times. At the same time, the outflow from ± 1 is also increased due to the increased value of ± 1 cells, which results in the initial decrease in measured signal after the density manipulation. The big outflow, on the other hand, leads to an increase in the coherence on other levels such as 0, ± 2, ± 3, etc., which in turn increases the inflow back to ± 1 levels. Therefore, a new balance between the outflow and inflow will form, giving another rather constant signal tail.

All of the simulations shown above are averaged over many DRs. But, if you just look at the density matrix of a single DR, you will not see any clue of measurable

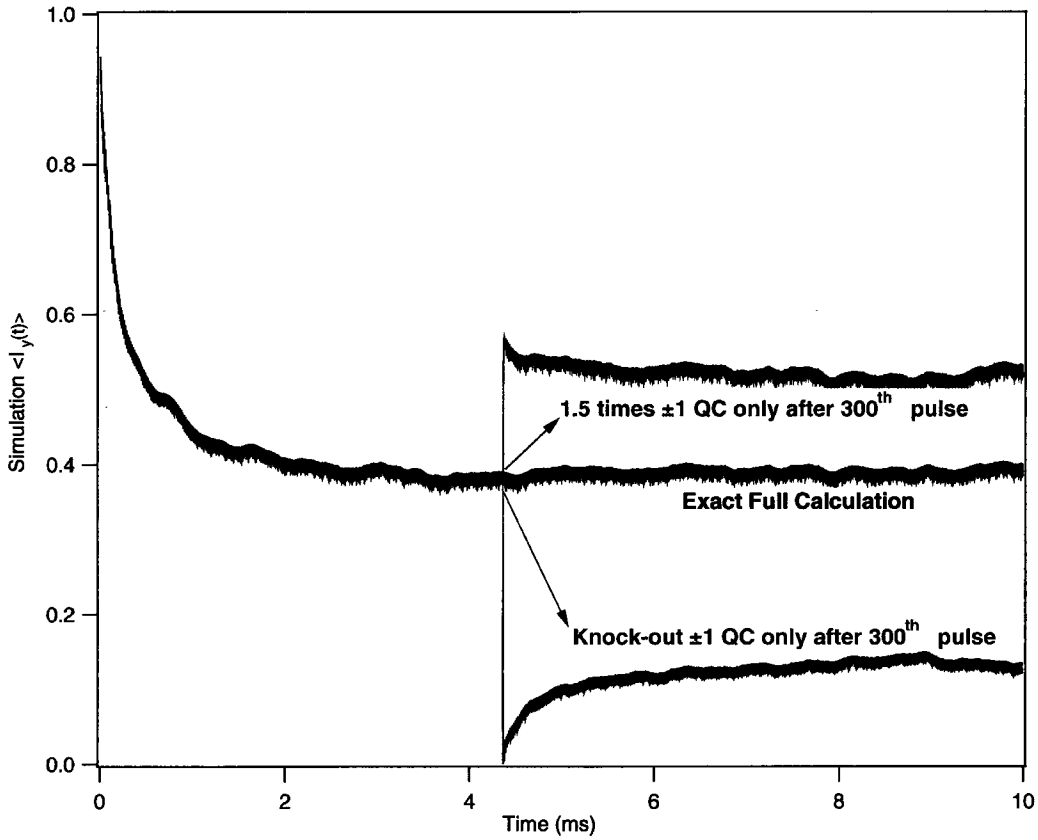

Figure 7.4: CPMG simulations calculated with the same parameters as those in Figure 7.3. The black curve is the full, exact calculation without any density matrix manipulation. The ±1 QC cells are either zeroed (red curve) or uniformly increased 1.5 times (blue curve) just after the 300^{th} π pulse.

signal. For example, the DR-averaged simulations in Figure 7.5 show a long tail in CPMG and a fast decay in APCPMG, just like what we observed in experiments [47, 48]. However, the snap shot of the density matrix generated by a single DR simulation seems to tell another story (Figure 7.6, the first and third row). Starting from I_{yT} right after the first tipping $\frac{\pi}{2}$ pulse, the density matrix of both CPMG and APCPMG shows barely any change after just two π pulses, suggesting the normalized signal is still close to 1. As more and more pulses are applied, the coherence starting from measurable ± 1 goes to almost everywhere, making both density matrices appear hopelessly scrambled. Based on these single-DR density matrices, it looks that CPMG does not do a better job than APCPMG in preserving the signal. It is true that neither gives a simple echo tail after thousands of pulses in a single-DR simulation. However, once an average is made over many density matrices calculated in separate DRs (Figure 7.6, the second and fourth row), both density matrices look very different from the single-DR case. The averaged density matrix for CPMG looks a lot like the initial density matrix I_{yT}, even after 2800 π pulses, indicating the potential of an echo tail. This is confirmed by the echo tail of CPMG simulation in Figure 7.5. On the other hand, after 2800 π pulses, the averaged density matrix for APCPMG looks black or close to black everywhere, indicating all the cells have either zero or close to zero values. Therefore, the simulation of APCPMG, averaged over 200 DRs, shows a spin echo curve decaying from 1 to nearly zero (Figure 7.5).

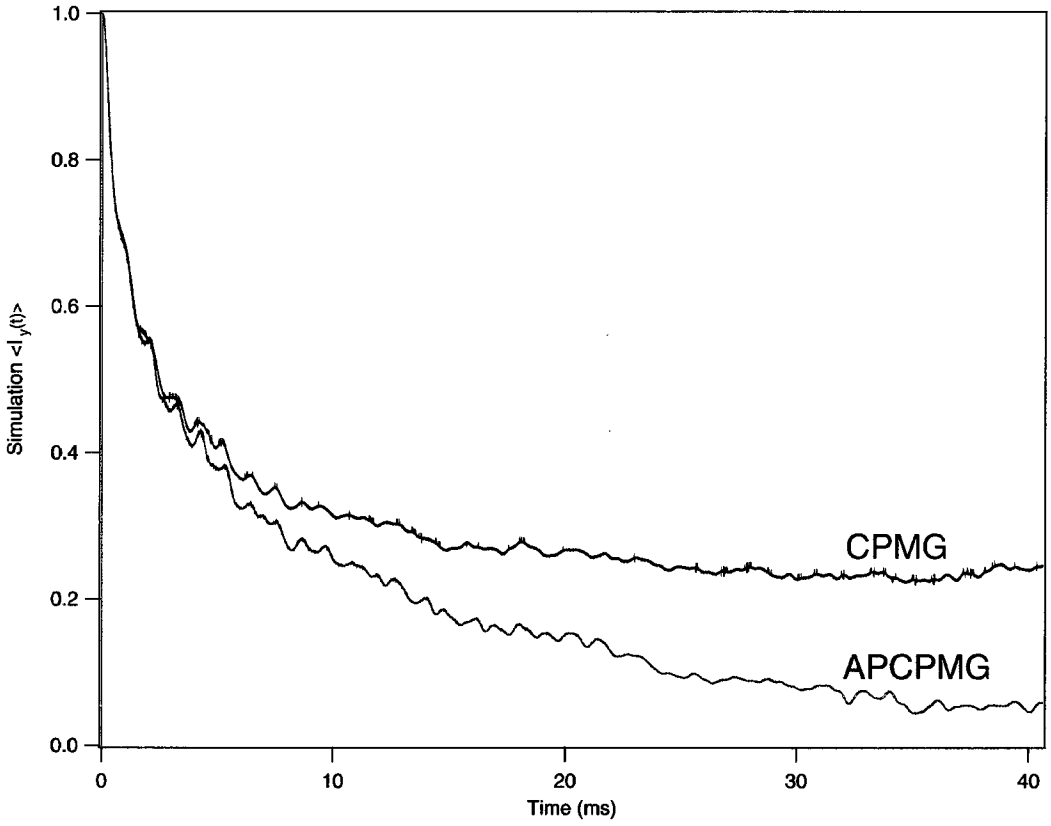

Figure 7.5: Exact calculations of CPMG and APCPMG, for pure dipolar decay with $\Omega_z = 0$, $\omega_1/2\pi = 40$ kHz, and τ=1 μs. Each curve is calculated with 200 DRs of N=6 spins on a Silicon lattice with 25 $\times$ B_{ij} of ^{29}Si. While $\bar{\mathcal{H}}^{(0)}_{\mathrm{APCPMG}} = \bar{\mathcal{H}}^{(0)}_{\mathrm{CPMG}}$, a difference between APCPMG and CPMG appears in the next term of the expansion, since $\bar{\mathcal{H}}^{(1)}_{\mathrm{APCPMG}} = 0$

.

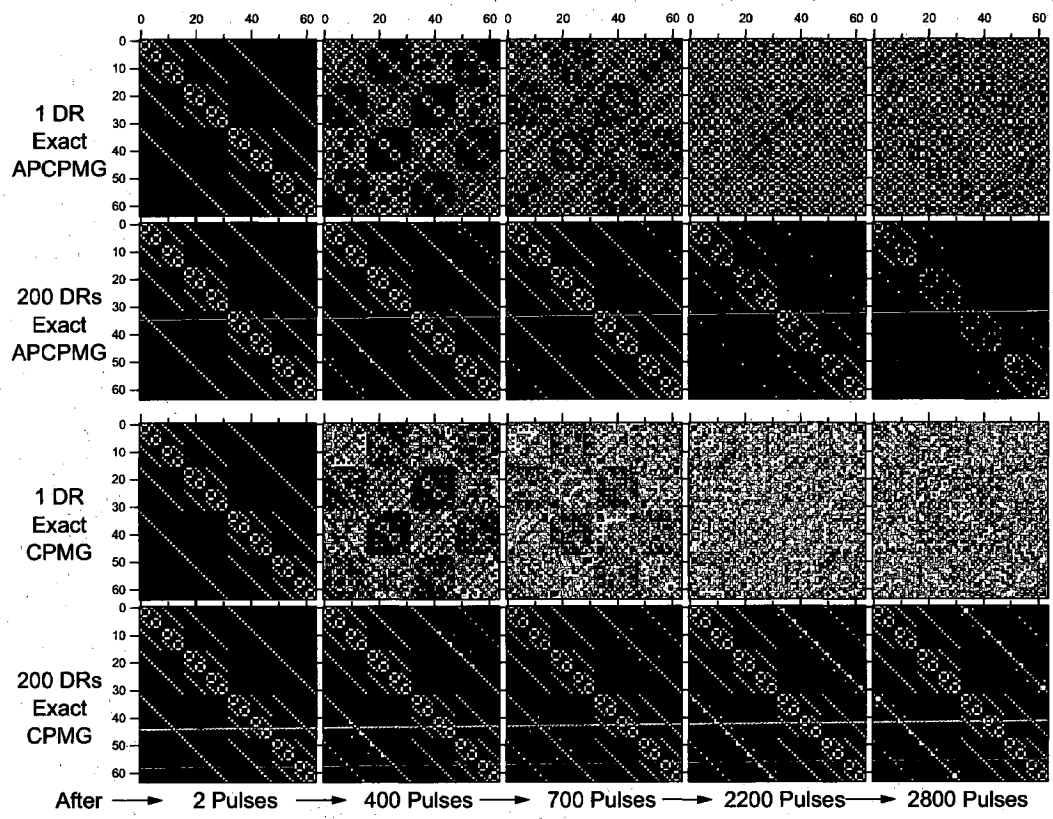

Figure 7.6: Calculated snapshots of a 6 spin ($2^6 \times 2^6$) density matrix evolving during either CPMG or APCPMG with conditions as in Figure 7.5. The red-white-blue color scale shows the phase angle, and black cells have negligible magnitude. All four rows use exact π pulses with non-zero durations. The top two rows use the APCPMG sequence. The bottom two rows use the CPMG sequence. Note that averaging over 200 DRs has very different effect for APCPMG (second row) versus CPMG (fourth row), despite the fact that $\bar{\mathcal{H}}^{(0)}_{\mathrm{APCPMG}} = \bar{\mathcal{H}}^{(0)}_{\mathrm{CPMG}}$.

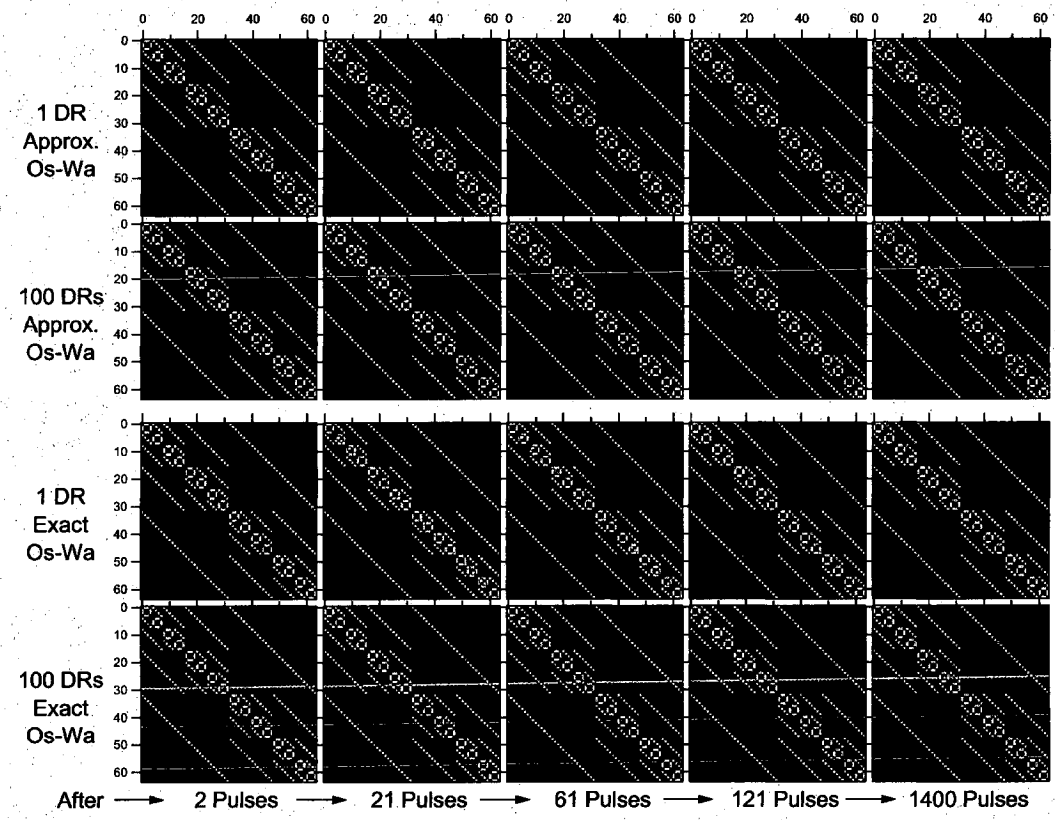

Figure 7.7: Calculated snapshots of a 6 spin ($2^6 \times 2^6$) density matrix evolving during Ostroff-Waugh sequence, using exact calculations with non-zero pulse duration (the bottom two rows) or the δ-pulse approximation by setting $\mathcal{H}_{zz} = 0$ during pulses (the top two rows).The red-white-blue color scale shows the phase angle, black cells have negligible magnitude.

Recall that in the δ-pulse approximation, coherence is restricted within the ± 1 cells. So, when making pulses act as instantaneous rotations, the CPMG and APCPMG simulations with $\Omega_z = 0$ collapse into one. This degenerate curve decays from 1 to 0, purely due to the dipolar term $\mathcal{H}_{zz}$. The presence of $\mathcal{H}_{zz}$ during the non-zero duration of pulses makes APCPMG decay while gives CPMG an echo tail (Figure 7.5), just as we observed in experiments. This clearly shows that the presence of $\mathcal{H}_{zz}$ during the finite pulses is an intrinsic reason for the difference between CPMG and APCPMG. Our average Hamiltonian simulations show that the nonzero $\bar{\mathcal{H}}^{(1)}$ is very important in producing the CPMG tail as seen in Figure 7.5. On the other hand, APCPMG has $\bar{\mathcal{H}}^{(1)} = 0$, and no long echo tail.

The long echo tail in CPMG emerges in a way very different from the Ostroff-Waugh sequence: $90_X - \{\tau - 90_Y - \tau\}^n$ [67]. For the Ostroff-Waugh, the leading order average Hamiltonian is $\bar{\mathcal{H}}^{(0)} = -\frac{1}{2}\mathcal{H}_{yy}$ for both instantaneous and non-zero duration $\frac{\pi}{2}$ pulses. Including the pulse durations in the simulation does not produce a big difference, compared to the δ-pulse approximation. As it shows in Figure 7.7, no matter using instantaneous or finite pulses, the density matrix of Ostroff-Waugh sequence all resembles the initial density matrix, for a single-DR calculation or averaging over 100 DRs. Comparing Figure 7.6 and Figure 7.7, the biggest difference is that for Ostroff-Waugh sequence, the coherence never seems to leave the measurable ± 1 cells; while for CPMG, the coherence spreads from ± 1 to all other QC levels, and later is brought back to measurable ± 1 QC and contribute to the measured signal.

Chapter 8

New Classes of Spin Echoes

In the last few Chapters, we reached the conclusion that the non-zero duration of π pulses may be responsible for the PSS observed in experiments: CPMG and APCP produce a long echo tail, while APCPMG and CP decay quickly to zero. The non-zero duration of pulses introduces extra average Hamiltonian terms that are not present in the δ-pulse approximation. These extra terms contain non-zeroth order quantum operators that can open extra coherence pathways in the density matrix, which may lead to the long echo tail observed in experiments. Even though pulse sequences like CPMG use a very simple pulse pattern, the zeroth- and first-order correction terms arising from the finite pulses are quite complicated. At this point in our analysis, we could not prove quantitatively that these terms were responsible for the long echo tail. So we were left wondering if the finite pulse terms explained $\sim$100% of the observed long echo tail, or just a small part of it with other factors explaining the rest?

In this Chapter, building upon our earlier understanding, we design more complicated pulse sequences, and show that much simpler approximate Hamiltonians can

quantitatively explain the experiments. The effective Hamiltonian terms exploited in this Chapter arise from the non-zero duration of pulses. Therefore, the experiments described in this Chapter cannot be explained by the δ-pulse approximation. The quantitative agreement between our theory and experiments suggests that the finite pulse effects are dominant at least for our experimental conditions.

All the experiments presented in the Chapter were conducted by Rona G. Ramos, with a powder sample of C_{60} in a 12 Tesla magnetic field at room temperature. At room temperature, C_{60} molecules form an fcc lattice [37], and each C_{60} ball undergoes rapid isotropic rotation about its lattice point [37, 88, 94]. This sample is well approximated as a single species of spin-$\frac{1}{2}$ nuclei (^{13}C), coupled together by the like-spin dipolar interaction [3, 48, 84]. For a mesoscopic cluster of N-spins, the Hamiltonian in the rotating frame is $\mathcal{H}_{int} = \mathcal{H}_Z + \mathcal{H}_{zz}$. Here we define the generalized Zeeman term $\mathcal{H}_Z = \Omega_z^{net} I_{z_T}$, with $\Omega_z^{net} = \Omega_{offset}^{global} + \Omega_z^{loc}$, where Ω_{offset}^{global} is from an intentional global resoance offset, and Ω_z^{loc} is due to the local Zeeman shift in the sample. Our macroscopic powders are similar to an ensemble of N-spin clusters, with different Ω_z^{loc} values in different clusters due to bulk diamagnetism [48]. The resulting Zeeman line broadening dominates the spectrum's FWHM, which was only $\sim$2 ppm (e.g., the ^{13}C spectrum has measured FWHM = 260 Hz, while the calculated dipolar FWHM=38 Hz). The RF pulses used were very hard (e.g., the pulse strength $\omega_1/2\pi \approx 25$ kHz) was $\sim$100 times the ^{13}C linewidth, with a 128.56 MHz Larmor frequency [84]). A Low coil filling factor [27, 84] (<8% for ^{13}C data) was used to make the RF pulses

uniform across the sample.

8.1 FID of Echo Train and Echo of Echo Train

The open grey squares in Figure 8.1(A) show the amplitude of each peak in a long-lived train of spin echoes [36, 84] generated by the CPMG experiment, $90_X - \{Y, Y\}^n$. The block $\{Y, Y\}$, which is repeated n times, represents the sequence $(\tau - 180_Y - 2\tau - 180_Y - \tau)$, and echoes are acquired in the 2τ time interval after every 180° (or π) pulse [23, 60, 84]. If we reverse the phase of the first π pulse in the repeating block to implement APCPMG, $90_X - \{-Y, Y\}^n$, the train of spin echoes quickly decays to zero (Figure 8.1(A), blue). Inserting a single 180_Y pulse into the APCPMG sequence, $90_X - \{-Y, Y\}^{n_1} - 180_Y - \{-Y, Y\}^{n_2}$, produces a striking echo in the envelope of the individual spin echo peaks, or an "echo of the echo train" (Figure 8.1(A), green). Although this echo of the echo train looks like a conventional Hahn echo [36], the signal actually extends over more than 800 individual spin echo peaks.

To understand this dramatic difference, we apply AHT [34, 60] to the repeating block $\{\phi_1, \phi_2\}$, with 180° pulses of duration t_p about the ϕ_1 or ϕ_2 axis, and cycle time $t_c = 4\tau + 2t_p$. Short t_c is used throughout this paper, so it is a good approximation to keep just the first two terms $\bar{\mathcal{H}}^{(0)} + \bar{\mathcal{H}}^{(1)}$ in the Magnus expansion [34, 60]. The $\{Y, Y\}$ block has [48]

$$\bar{\mathcal{H}}^{(0)}_{\{Y,Y\}} = \alpha\mathcal{H}_{zz} - \beta\mathcal{H}_{yy} \equiv \mathrm{H} \tag{8.1}$$

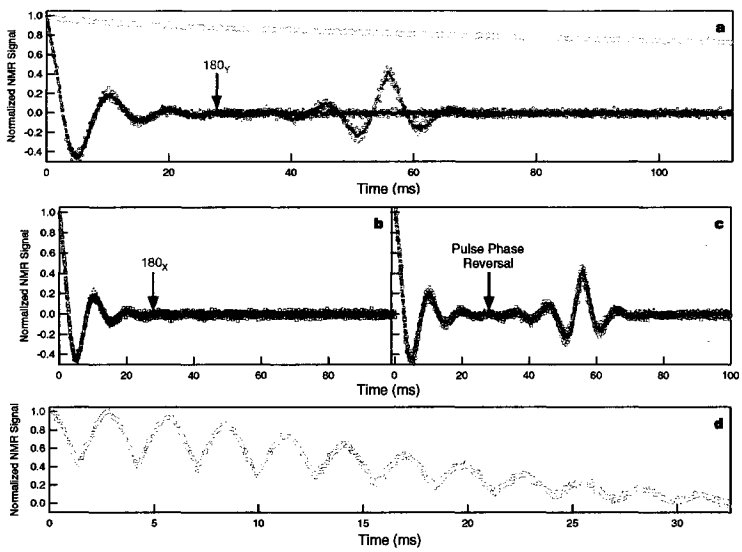

Figure 8.1: (a) Comparison of CPMG (grey) to APCPMG (blue). Inserting a single flip-180_Y pulse into APCPMG induces an echo of the echo train (green). (b) Inserting a single 180_X (red) has no effect compared to the blue trace. (c) Reversing the APCPMG phase pattern, $90_X - \{-Y,Y\}^{200} - \{Y,-Y\}^{600}$, at the point indicated has the same effect (black) as inserting a single 180_Y pulse (green). (d) A CPMG of the echo train is induced by using $90_X - \{-Y,Y\}^{10} - (\{Y,-Y\}^{20} - \{-Y,Y\}^{20})_{repeat}$. For (a-d), τ=25 μs, $\Omega_{offset}^{global} = 0$, $\alpha \approx 0.71$, and only the peak of each echo is shown. The signals in Figure 8.1-8.3 are normalized to the amplitude of the C_{60} FID signal.

while the $\{-Y, Y\}$ block has a slightly different form:

$$\bar{\mathcal{H}}^{(0)}_{\{-Y,Y\}} = \mathrm{H} - \lambda\Omega_z I_{x_T} \tag{8.2}$$

where $\alpha = \frac{4\tau}{t_c}$, $\beta = \frac{t_p}{t_c}$, $\lambda = \frac{4t_p}{\pi t_c}$, and

$$\mathcal{H}_{\sigma\sigma} = \sum_{j>i}^{N} B_{ij}(3I_{\sigma_i}I_{\sigma_j} - \vec{I}_i \cdot \vec{I}_j), \quad \text{for} \quad \sigma = x, y, z \tag{8.3}$$

The extra term $-\lambda\Omega_z^{net} I_{x_T}$ looks like a constant transverse field in the X-direction, which, when acting alone, causes spins to nutate [84] in the Y-Z plane in a manner we define as clockwise (CW). Variation in Ω_z^{net} values across the macroscopic sample leads to a spread in precession angles that causes signal decay. In the well known FID, $T_2^\star$ arises from a spread in Ω_z^{net} of the original Zeeman Hamiltonian. By analogy, the rapid decay of the spin echoes produced by $90_X - \{-Y, Y\}^n$ (Figure 8.1(a), blue) can be thought of as an "FID of the echo train."

Attempting to undo this $T_2^\star$-like decay, we insert a single 180_Y pulse into the APCPMG sequence, $90_X - \{-Y, Y\}^{n_1} - 180_Y - \{-Y, Y\}^{n_2}$, which produces a striking echo of the echo train (Figure 8.1(a), green). The dephasing caused by $-\lambda\Omega_z^{net} I_{x_T}$ (CW precession) during the $n_1 t_c$ is followed by counter-clockwise (CCW) precession caused by $+\lambda\Omega_z^{net} I_{x_T}$, and this rephasing leads to the echo of the echo train when $n_2 = n_1$. When a single flip-180_X is used instead, no echo of the echo train (Figure 8.1(b) red) is seen, as predicted by our model, because a perfect rotation along the X-axis does not change the sign of the $-\lambda\Omega_z^{net} I_{x_T}$ term. On the other hand, the echo of the echo train (Figure 8.1(c) black) is recovered if the flip-180_X is removed and

the phase pattern in the second repeating block is reversed from $\{-Y, Y\}$to $\{Y, -Y\}$, since [48] $\bar{\mathcal{H}}^{(0)}_{\{Y,-Y\}} = \mathrm{H}+\lambda\Omega_z I_{x_T}$, compared to $\bar{\mathcal{H}}^{(0)}_{\{-Y,Y\}} = \mathrm{H}-\lambda\Omega_z I_{x_T}$. In Figure 8.1(c), the phase reversal of 1200 hard π pulses yields a signal indistinguishable from that induced by the single flip-180_Y, as predicted by our model. In contrast to this model, taking the limit of δ-function pulses ($t_p \to 0$) would kill [47, 48] the transverse field terms in $\bar{\mathcal{H}}^{(0)} + \bar{\mathcal{H}}^{(1)}$ exploited here and throughout the rest of this chapter. Figure 8.1(D) shows that the echo of of the echo train in Figure 8.1(C) can be repeated, creating multiple echoes in the envelope of individual spin echo peaks, or a "CPMG of the echo train." However, the signal does decay, since the sign of the term H is never reversed in Figure 8.1, which contributes to the observed decay of the CPMG of the echo train. To recover more coherence, it is necessary to refocus all terms in the effective Hamiltonian, which we shall discuss in the next section.

This treatment of the flip-180_Y as a δ-function pulse may seem inconsistent, since we are exploiting effects of the repeating block that come from the non-zero duration of the π pulses. While the internal structure of the π pulses adds non-zero quantum coherence operators [47, 48] to $\bar{\mathcal{H}}^{(0)} + \bar{\mathcal{H}}^{(1)}$, and they only manifest large effects after the coherent repetition of many $\{\phi_1, \phi_2\}$ blocks. Therefore, treating the single 180° pulse outside of the repeating block as a δ-function rotation is a good approximation for our purposes.

8.2 New Analogs of Magic Echo

In the magic echo [42, 78, 79, 77, 86], a continuous RF field along X (such as $-\hbar\omega_1 I_{x_T}$) picks out the part of the dipolar coupling that is secular in the strong transverse field [84], i.e.$\mathcal{H}_{zz} \rightarrow -\frac{1}{2}\mathcal{H}_{xx}$, which is then rotated to $-\frac{1}{2}\mathcal{H}_{zz}$, leading to a negative dipolar evolution. For the $\{-X, X\}$ block [48]

$$\bar{\mathcal{H}}^{(0)}_{\{-X,X\}} = \alpha\mathcal{H}_{zz} - \beta\mathcal{H}_{xx} + \lambda\Omega_z^{net} I_{y_T} \tag{8.4}$$

$$\bar{\mathcal{H}}^{(1)}_{\{-X,X\}} = 0 \tag{8.5}$$

the weak effective field $\lambda\Omega_z^{net} I_{y_T}$ in $\bar{\mathcal{H}}^{(0)}_{\{-X,X\}}$ could play the same role, as first proposed by Piness and Waugh [69] for a single value of Ω_z^{net}. Figure 8.2 provides experimental support for their prediction, even though the weak effective transverse field scale makes it hard to justify their second averaging analysis [33, 69]. In addition, there is a spread in Ω_z^{net} across our macroscopic sample, and this Ω_z^{net} has non-trivial consequences, as shown by the different effects (Figure 8.2) of the two bursts, $\{-X, X\}^n - 90_{\pm X}$, followed by a free evolution of duration t_{free}.

To understand Figure 8.2, we rewrite $\bar{\mathcal{H}}^{(0)}$ as,

$$\begin{aligned} \bar{\mathcal{H}}^{(0)}_{\{-X,X\}} &= \alpha\mathcal{H}_{zz} - \beta\mathcal{H}_{xx} + \lambda\Omega_z^{net} I_{y_T} \\ &= -\frac{\alpha-\beta}{2}\mathcal{H}_{yy} + \lambda\Omega_z^{net} I_{y_T} + \bar{\mathcal{H}}^{(0)}_{Nonsucular} \end{aligned} \tag{8.6}$$

For simplicity, we drop the nonsecular term $\bar{\mathcal{H}}^{(0)}_{Nonsucular}$ altogether, as in second averaging [33, 61, 69]. This second averaging approximation is hard to justify here, since

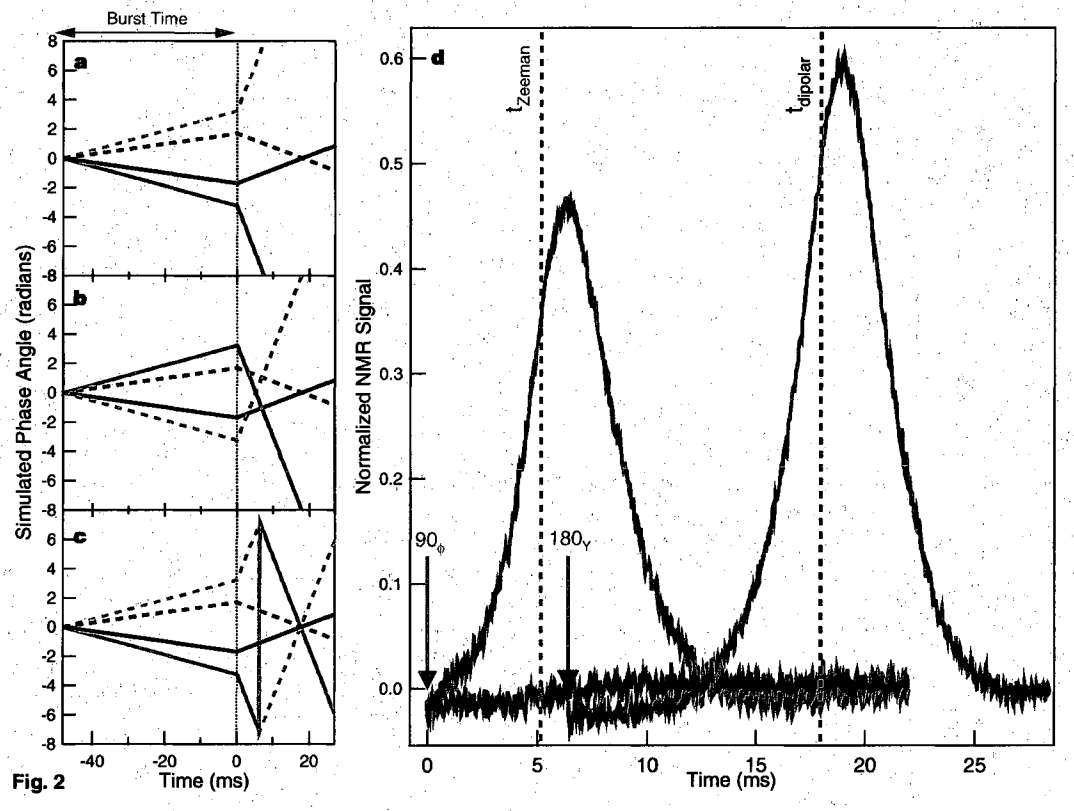

Figure 8.2: The three experiments inspired by the original magic echo [42, 79, 77], which all start with $\{-X, X\}^n$, have distinctly different results. This can be understood by simulating the evolution of the Zeeman phase angle $\Phi_Z(t)$ and the dipolar phase angle $\Phi_D(t)$ for each experiment. (a-c) Representative values $\Omega_z/h = +/-100$ Hz and $\Omega_D/h = +/-15$ Hz are shown (solid/dashed), with $\Phi_D(t)$ in black, and $\Phi_Z(t)$ in the color of the experimental trace. The end of the burst time is t = 0 ms. The crossing of $\Phi_Z(t)$ lines (at $t \geq 0$) sets the Zeeman refocusing time t_{Zeeman}; the crossing of $\Phi_D(t)$ lines determines $t_{dipolar}$. In (a) with 90_{-X} following the repeating block, the $\Phi_Z(t)$ lines fail to cross, and the large Zeeman dephasing spoils the dipolar echo (red in d). In (b) with 90_{+X} following the repeating block, the $\Phi_Z(t)$ lines do cross, and an echo (blue in d) is observed close to t_{Zeeman} (blue dashed line in d). A dipolar echo as suggested by the crossing of $\Phi_D(t)$ lines at $t_{dipolar}$ (black dashed line in d) is not seen, because the Zeeman dephasing is large enough to spoil it. In (c), the failed sequence in (a) is repaired by applying a 180_Y pulse at time t_{f_1} after the burst, which forces the $\Phi_Z(t)$ and $\Phi_D(t)$ lines to cross simultaneously, resulting in the optimized echo (green in d). τ=50 μs and n=200.

$\lambda\Omega_z^{net}I_{y_T}$ is not typically the largest term in $\bar{\mathcal{H}}^{(0)}_{\{-X,X\}}$, but the resulting theory works surprisingly well. The first two sequences start with the burst $\{-X,X\}^n - 90_{\pm X}$, followed by a free evolution of duration t_{free}. The $\pm X$ phase choice for the 90° pulse corresponds to the time evolution operator

$$e^{-\frac{i}{\hbar}\left(\mathcal{H}_{zz}+\Omega_z^{net}I_{z_T}\right)t_{free}}e^{-\frac{i}{\hbar}\left(-\frac{(\alpha-\beta)}{2}\mathcal{H}_{zz}\mp\lambda\Omega_z^{net}I_{z_T}\right)nt_c}\mathcal{U}_{90_{\pm X}}$$

where $\alpha > \beta$ for our experiments. To help explain our data, we will introduce the tool of dipolar phase angle Φ_D and Zeeman phase angle Φ_Z. The above time evolution operator can be rewritten as

$$e^{i\Phi_D(t^*)\tilde{\mathcal{H}}_{zz}}e^{i\Phi_Z(t^*)\tilde{\mathcal{H}}_Z} \tag{8.7}$$

We define dimensionless operators $\tilde{\mathcal{H}}_{zz} = \mathcal{H}_{zz}/\Omega_D$ and $\tilde{\mathcal{H}}_Z = \mathcal{H}_Z/\Omega_Z$, where Ω_D is a typical dipolar energy scale and Ω_Z is a typical Zeeman shift scale. At time $t^* = t_{free} + nt_c$, we define the dipolar phase angle,

$$\Phi_D(t^*) = \frac{-\Omega_D}{\hbar}\left(t_{free} - \frac{\alpha-\beta}{2}\right)nt_c \tag{8.8}$$

and the Zeeman phase angle,

$$\Phi_Z(t^*) = \frac{-\Omega_Z}{\hbar}(t_{free} \mp \lambda nt_c) \tag{8.9}$$

Figure 8.2 (a-c) show the evolution of $\Phi_D(t)$ and $\Phi_Z(t)$ during the corresponding experiments using $\Omega_D/h = \pm 15$Hz and $\Omega_Z/h = \pm 100$Hz.

For the X choice the Zeeman phase wraps in a CCW manner both during and after the burst (Figure 8.2(a) red), which spoils the magic echo that would otherwise

form during the free evolution period (Figure 8.2(d) red). For the +X choice both Zeeman and dipolar terms switch from CW phase wrapping in the burst to CCW phase unwrapping during the free evolution period (Figure 8.2(b)), resulting in a large echo (Figure 8.2(d) blue). Note that if the $\{-X, X\}^n$ used δ-function pulses, then the 90_X (or 90_{-X}) would produce an FID [84], instead of the echo (or no echo) in the real experiments.

However, this echo (Figure 8.2(d) blue) is not optimized, since the refocusing time is different (Figure 8.2(b)) for the dipolar and Zeeman phases ($t_{\text{dipolar}} = (\alpha - \beta)\, nt_c/2$ and $t_{\text{Zeeman}} = \lambda n t_c$). An optimized echo (Figure 8.2(d) green) is generated if we apply a 180_Y at time t_{f_1} after the failed sequence $\{-X, X\}^n - 90_{-X}$(Figure 8.2(d) red). This sequence aims to synchronize the refocusing times of the dipolar and Zeeman phases (Figure 8.2(c)). The corresponding unitary operator is,

$$
\begin{aligned}
& e^{-\frac{i}{\hbar}\left(\mathcal{H}_{zz}+\Omega_z^{net} I_{z_T}\right) t_{f_2}} \mathcal{U}_{180_Y} e^{-\frac{i}{\hbar}\left(\mathcal{H}_{zz}+\Omega_z^{net} I_{z_T}\right) t_{f_1}} e^{-\frac{i}{\hbar}\left(-\frac{(\alpha-\beta)}{2}\mathcal{H}_{zz}+\lambda\Omega_z^{net} I_{z_T}\right) n t_c} \mathcal{U}_{90_{-X}} \\
= \; & \mathcal{U}_{180_Y}\mathcal{U}_{180_Y}^{-1} e^{-\frac{i}{\hbar}\left(\mathcal{H}_{zz}+\Omega_z^{net} I_{z_T}\right) t_{f_2}} \mathcal{U}_{180_Y} e^{-\frac{i}{\hbar}\left(\mathcal{H}_{zz}+\Omega_z^{net} I_{z_T}\right) t_{f_1}} e^{-\frac{i}{\hbar}\left(-\frac{(\alpha-\beta)}{2}\mathcal{H}_{zz}+\lambda\Omega_z^{net} I_{z_T}\right) n t_c} \mathcal{U}_{90_{-X}} \\
= \; & \mathcal{U}_{180_Y} e^{-\frac{i}{\hbar}\left(\mathcal{H}_{zz}-\Omega_z^{net} I_{z_T}\right) t_{f_2}} e^{-\frac{i}{\hbar}\left(\mathcal{H}_{zz}+\Omega_z I_{z_T}\right) t_{f_1}} e^{-\frac{i}{\hbar}\left(-\frac{(\alpha-\beta)}{2}\mathcal{H}_{zz}+\lambda\Omega_z^{net} I_{z_T}\right) n t_c} \mathcal{U}_{90_{-X}} \\
= \; & \mathcal{U}_{180_Y} e^{-\frac{i}{\hbar}\left(t_{f_1}+t_{f_2}-\frac{\alpha-\beta}{2} n t_c\right)\mathcal{H}_{zz}} e^{-\frac{i}{\hbar}\left(t_{f_1}-t_{f_2}-\lambda n t_c\right)\Omega_z^{net} I_{z_T}} \mathcal{U}_{90_{-X}}
\end{aligned}
\tag{8.10}
$$

which shows that the optimized echo should happen at

$$
t_{Zeeman} = t_{dipolar} = t_{f_1} + t_{f_2} = \frac{\alpha - \beta}{2} n t_c \tag{8.11}
$$

for $t_{f_1} = \left(\frac{\alpha-\beta-2\lambda}{4}\right)$. The measured echo happens at a slightly different time, due to the terms ignored in this model.

Compared to the original magic echo [42, 79, 77], sequences based on the $\{-X, X\}^n$ block have several clear differences: both Zeeman and dipolar phases are wrapped during the burst (Figure 8.2(a-c)), a $90_{\pm X}$ is used instead of the 90_Y, and the 2τ gaps in between the π pulses of the {-X,X} block simplify implementation.

8.3 Quadratic Echoes

So far, the experiments have been designed using only $\bar{\mathcal{H}}^{(0)}_{\{\phi_1,\phi_2\}}$. However, repeating blocks with non-zero $\bar{\mathcal{H}}^{(1)}_{\{\phi_1,\phi_2\}}$ are also very useful, despite their more complicated form. For the {X,X} block [48]

$$\bar{\mathcal{H}}^{(0)}_{\{X,X\}} = \alpha\mathcal{H}_{zz} - \beta\mathcal{H}_{xx} \tag{8.12}$$

$$\bar{\mathcal{H}}^{(1)}_{\{X,X\}} = -\left(\kappa\Omega_z^{net}\right)^2 I_{x_T} + \bar{\mathcal{H}}^{(1),non-I_{x_T}}_{\{X,X\}} \tag{8.13}$$

where $\kappa = \sqrt{t_p\left(8\tau + 2t_p\right)/\left(2t_c\hbar\pi\right)}$, and $\bar{\mathcal{H}}^{(1),non-I_{x_T}}_{\{X,X\}}$ contains terms in $\bar{\mathcal{H}}^{(1)}_{\{X,X\}}$ not proportional to I_{x_T}. By analogy, we had hoped to use $-\left(\kappa\Omega_z\right)^2 I_{x_T}$ in the same way that $\lambda\Omega_z I_{y_T}$ was used in the experiments of Figure 8.2. This was unsuccessful, however, since the terms in $\bar{\mathcal{H}}^{(1),non-I_{x_T}}_{\{X,X\}}$ have a big impact as {X,X} is repeated. Fortunately, the block {-X,-X} has [48] $\bar{\mathcal{H}}^{(0)}_{\{-X,-X\}} = \bar{\mathcal{H}}^{(0)}_{\{X,X\}}$ and $\bar{\mathcal{H}}^{(1)}_{\{-X,-X\}} = -\bar{\mathcal{H}}^{(1)}_{\{X,X\}}$, so we improve upon $\{X, X\}^n$ by switching to the composite block $\{X, X\}^{\frac{n}{2}}\{-X, -X\}^{\frac{n}{2}}$, which appears to be well approximated by the unitary operator

$$e^{-\frac{i}{\hbar}\left(-\frac{1}{2}\mathcal{H}_{xx}+\left(\kappa\Omega_z^{net,-}\right)^2 I_{x_T}\right)\frac{nt_c}{2}} e^{-\frac{i}{\hbar}\left(-\frac{1}{2}\mathcal{H}_{xx}-\left(\kappa\Omega_z^{net,+}\right)^2 I_{x_T}\right)\frac{nt_c}{2}} \tag{8.14}$$

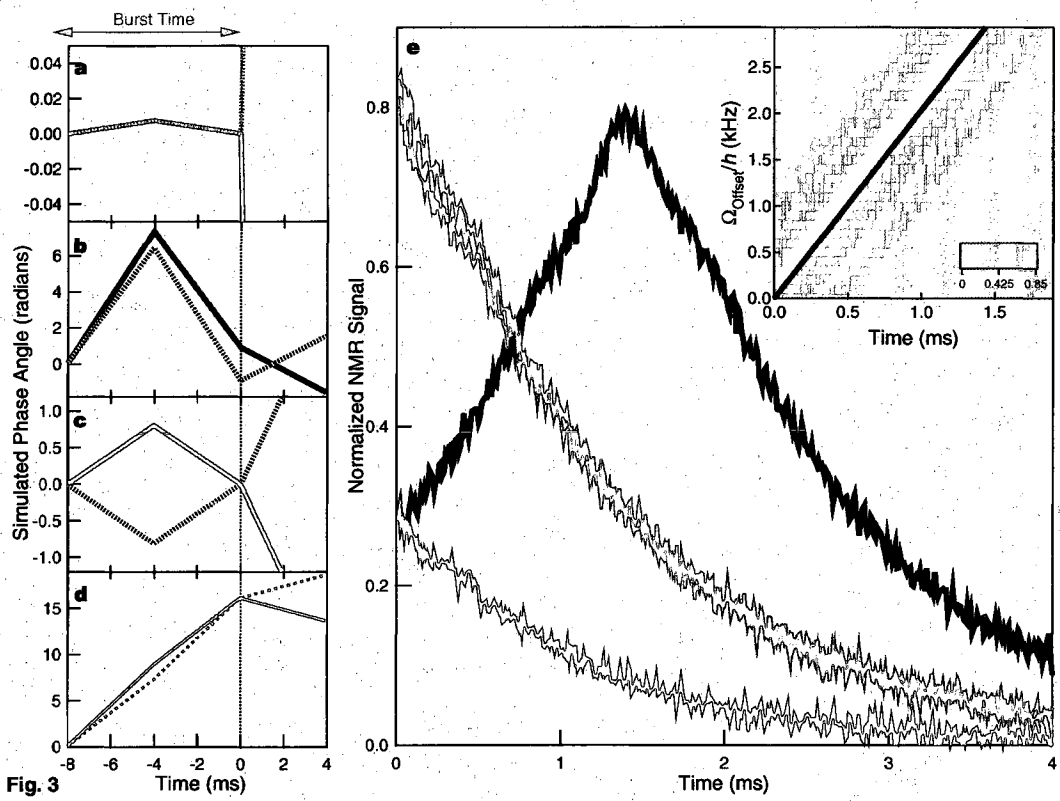

Figure 8.3: Quadratic echoes produced by $\{X,X\}^{\frac{n}{2}}\{-X,-X\}^{\frac{n}{2}} - 90_Y - t_{free}$ and linear echoes produced by $\{-X,X\}^{\frac{n}{2}}\{X,-X\}^{\frac{n}{2}} - 90_X - t_{free}$ have distinctly different behavior, for $\Omega_z^{net,\pm} = \Omega_z^{loc} \pm \Omega_{offset}^{global}$ (see text). The simulated Zeeman phase angle $\Phi_Z(t)$ during and after the quadratic burst for (a) $\nu_{offset}^{global} = 0$ Hz (green) and (b) $\nu_{offset}^{global} = -3$ kHz (black) evolves differently than the linear burst for (c) $\nu_{offset}^{global} = 0$ Hz (blue) and (d) $\nu_{offset}^{global} = -1$ kHz (red). Representative $\Omega_z/h = +/-100$ Hz values are shown (solid/dashed). The Zeeman refocusing time occurs when the two lines cross at t = 0 (a, c-d) or $t > 0$ (b). Signal measurement begins at the end of the burst (t = 0 ms) and is shown in pane (e) with trace colors corresponding to the ν_{offset}^{global} and sequences of (a-d). Note that only the black echo is shifted to the right. Inset (e) is an image plot of 31 quadratic echoes as a function of Ω_{offset}^{global}, for 0 Hz $\leq \Omega_{offset}^{global}/h \leq 3$ kHz, in steps of 100 Hz. The black trend line indicates the Zeeman refocusing time predicted by our model. τ=10 μs and n=100.

For the most general case, we define $\Omega_z^{net,+}$ (or $\Omega_z^{net,-}$) to be the net Zeeman shift during the $\{X,X\}^{\frac{n}{2}}$ (or $\{-X,-X\}^{\frac{n}{2}}$) block.

To demonstrate the unusual effects of the quadratic transverse field term $-(\kappa\Omega_z)^2 I_{x_T}$, we used phase-corehent frequency jumping $\Omega_z^{net,\pm} = \Omega_z^{loc} \pm \Omega_{offset}^{global}$ ($\Omega_{offset}^{global} \geq 0$) during the burst $\{X,X\}^{\frac{n}{2}}\{-X,-X\}^{\frac{n}{2}} - 90_Y$, followed by a free evolution period with $\Omega_{offset}^{global} = 0$. Here, $\Omega_{offset}^{global} \equiv -h\nu_{offset}^{global}$ and ν_{offset}^{global} is the pulse frequency offset relative to the Larmor frequency. The phase-coherent frequency jumping for this quadratic echo was implemented on a Tecmag Apollo spectrometer. The unitary operator for this experiment is

$$e^{-\frac{i}{\hbar}\left(\mathcal{H}_{zz}+\Omega_z^{loc}I_{z_T}\right)t_{free}}e^{-\frac{i}{\hbar}\left(-\frac{1}{2}\mathcal{H}_{zz}-\left(2\kappa^2\Omega_z\Omega_{offset}^{global}\right)I_{z_T}\right)nt_c}\mathcal{U}_{90_Y}$$

which shows that the rate of Zeeman dephasing in the burst, due to a spread in Ω_z^{loc}, grows with Ω_{offset}^{global}. Thus, increasing Ω_{offset}^{global} pushes the quadratic echo peak out to a later time after the burst as demonstrated both in simulations (Figure 8.3(a, b)) and experiments (Figure 8.3(e) green, black). More specifically, the inset of Figure 8.3(e) shows the strong agreement between the Zeeman refocusing time predicted by our model (black trend line) and the quadratic echo peak measured in our experiments over a range of Ω_{offset}^{global}. In contrast, the corresponding linear sequence $\{-X,X\}^{\frac{n}{2}}\{X,-X\}^{\frac{n}{2}} - 90_X$ exhibits completely different behavior. The unitary operator for this experiment is

$$e^{-\frac{i}{\hbar}\left(\mathcal{H}_{zz}+\Omega_z I_{z_T}\right)t_{free}}e^{-\frac{i}{\hbar}\left(-\frac{(\alpha-\beta)}{2}\mathcal{H}_{zz}-\lambda\Omega_{offset}^{global}I_{z_T}\right)nt_c}\mathcal{U}_{90_X} \qquad (8.15)$$

Since the uniform Ω_{offset}^{global} contributes only a trivial global phase factor and the dominant Zeeman dephasing takes place during t_{free}, the largest signal should occur just after the burst, for all Ω_{offset}^{global}. This is seen in both simulations (Figure 8.3(c,d)) and experiments (Figure 8.3(e) blue, red).

Chapter 9

Line Narrowing and MRI of Solids

So far we have shown that the non-zero duration of strong pulses leads to extra terms in the average Hamiltonian $\bar{\mathcal{H}}^{(0)}$ and $\bar{\mathcal{H}}^{(1)}$, and these terms can have large, non-trivial effects. Using the internal structure of strong π pulses, we designed analogs of the original free induction decay (FID of the echo train), Hahn echo (echo of the echo train), and CPMG echoes (CPMG of the echo train). Variants on the original magic echo was also demonstrated using the zeroth- and first-order average Hamiltonian expressions. Those interesting new echo phenomena presented in the last chapter proved that our model of finite pulse effects was quantitative. At that point, we wondered if these effects had any useful application. In this chapter, we will demonstrate how the internal structure of strong π pulses can be used to design alternative approaches to line-narrowing and magnetic resonance imaging (MRI) of solids.

The experiments reported in this Chapter were done on the same C_{60} sample with the same experimental conditions as described in the last Chapter, and another

powder sample Silicon doped with Sb (10^{17} Sb/cm^3) with the experimental conditions described below. This Silicon sample is also well-approximated as a a single species of spin-$\frac{1}{2}$ nuclei, coupled together by the like-spin dipolar interaction [47, 48]. The Zeeman line broadening of the Silicon sample dominates the spectrum linewidth (^{29}Si spectrum's measured FWHM = 200 Hz, the calculated dipolar FWHM = 88 Hz). Like the C_{60} experiments, the RF pulses used for ^{29}Si were also hard (e.g., the pulse strength $\omega_1/2\pi \approx 16.4$ kHz was $\sim$ 82 times the ^{29}Si linewidth, with a 101.56 MHz Larmor frequency [84]). The coil filling factor for ^{29}Si sample was [84] $\sim$40% to make the RF pulses uniform across the sample. All the experiments in this Chapter were carried out in a 12 Tesla field at room temperature except as otherwise noted.

9.1 Application: Line Narrowing of Solids

In the last chapter, we introduced the quadratic echo. Controlling both dipolar and Zeeman phase wrapping using non-zero $\bar{\mathcal{H}}^{(1)}_{\{\phi_1,\phi_2\}}$ is an unusual aspect of the quadratic echo. This favorable property motivated our design of the larger composite block $(\Delta+\delta)-90_{\psi_1}-\{-X,X\}^{\frac{n}{2}}\{X,-X\}^{\frac{n}{2}}-90_{\psi_2}-(\Delta-\delta)$, where the time interval $\Delta = nt_c/4$, $|\delta| \leq \Delta$ and $\psi_i = \pm Y$ for i=1, 2. We will refer to this block as $\{n, \delta, \psi_1, \psi_2\}$. If we hold $\Omega_z^{net} = \Omega_z^{loc} + \Omega_{offset}^{global}$ constant during the whole block, the corresponding unitary operator can be approximated as

$$\mathcal{U}_{180_Y} e^{-\frac{i}{\hbar}\left(\Omega_z^{net} I_{z_T}\right)(+2\delta)} \quad : \quad \text{for} \quad \psi_1 = \psi_2 \tag{9.1}$$

$$e^{-\frac{i}{\hbar}\left(\Omega_z^{net} I_{z_T}\right)(+2\Delta)} \quad : \quad \text{for} \quad \psi_1 \neq \psi_2 \tag{9.2}$$

These two equations show that over the composite block of duration 6Δ, there is no net dipolar evolution, only a net Zeeman phase wrapping of either $+2\Omega_z^{net}\Delta$ or $+2\Omega_z^{net}\delta$, depending upon the choice of ψ_i.

Equation (9.1) suggests that both the dipolar and Zeeman dephasing will be completely refocused to give a narrowed spectrum, provided that $\psi_1 = \psi_2$, $\delta = 0$, and the signal is acquired at the end of each $\{n, 0, \psi_1, \psi_2\}$ block. Indeed, as it shows in Figure 9.1 our line-narrowing sequence with $n = 2$ and ν_{offset}^{global} =-3.5 kHz ($\Omega_{offset}^{global} \equiv -h\nu_{offset}^{global}$) reduces the normal linewidth from 260 Hz (Figure 9.1, Inset red) to about 0.3 Hz (Figure 9.1, Inset blue).

Note that the narrowed spectrum produced by our line-narrowing sequence (Figure 9.1, Inset blue) is centered at the pulse frequency offset ν_{offset}^{global}=-3.5 kHz, and $|\nu_{offset}^{global}|$ is much larger than the original spectral linewidth (260 Hz). In fact, the slow signal decay observed with our line-narrowing sequence is similar over a large range of $|\nu_{offset}^{global}|$, as well as over a range of n (Figure 9.2). The fact that the decay constant is nearly uniform when measured with different experimental parameters suggests that the observed signal decay is due to some intrinsic decay process. So far we have approximated the internal Hamiltonian of the spin system as the sum of the Zeeman term and the secular dipolar term ($\mathcal{H}_{int} = \mathcal{H}_Z + \mathcal{H}_{zz}$), but there is actually another term due to the fluctuating field caused by the fast spinning of buckyball molecules. This fluctuating field term is much smaller than both $\mathcal{H}_Z$ and $\mathcal{H}_{zz}$, so we normally

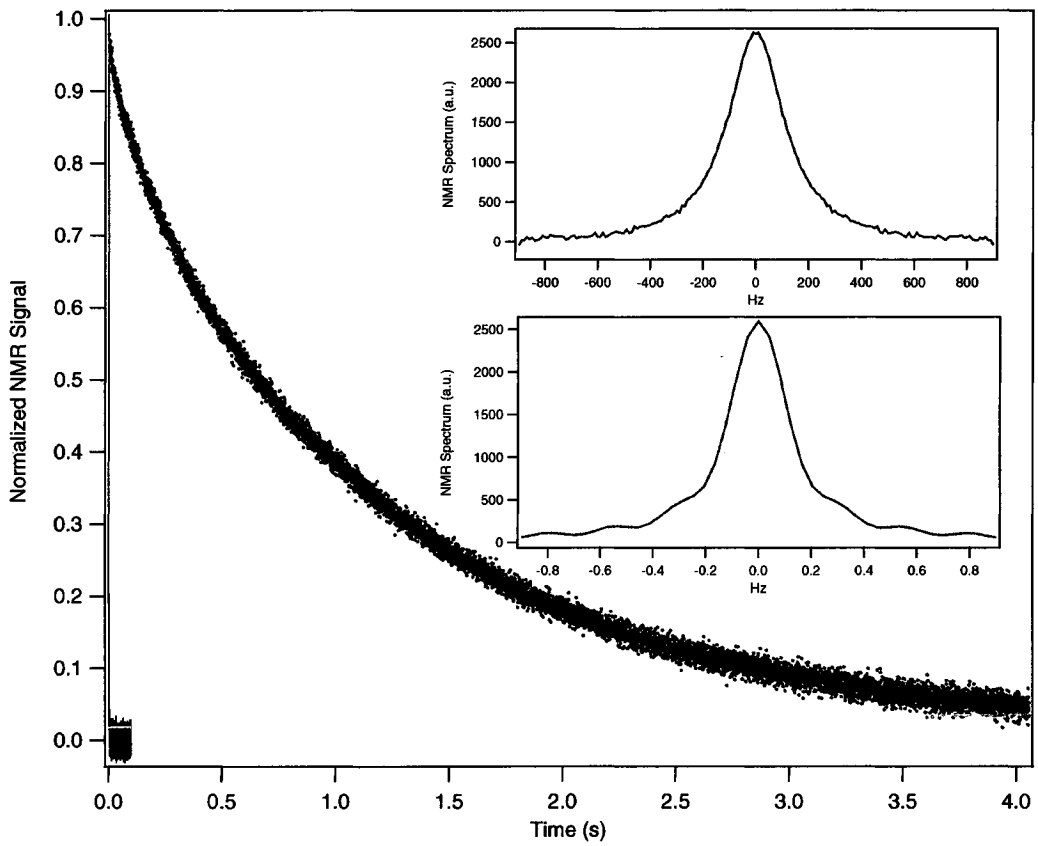

Figure 9.1: Experiments on C_{60} using the Apollo. The time-suspension data using the line-narrowing sequence $90_X - \{2, 0, -Y, -Y\}^m$ (blue) extend far beyond the normal ^{13}C FID (red). (Inset) The 200 Hz normal spectrum (red) is narrowed to 0.3 Hz centered at ν_{offset}^{global} (blue). The line-narrowing sequence was performed with m=10000, $\omega_1/2\pi \approx$25 kHz, τ=22 μs, and ν_{offset}^{global}= -3.5 kHz, while the FID was done with ν_{offset}^{global}= 0 Hz.

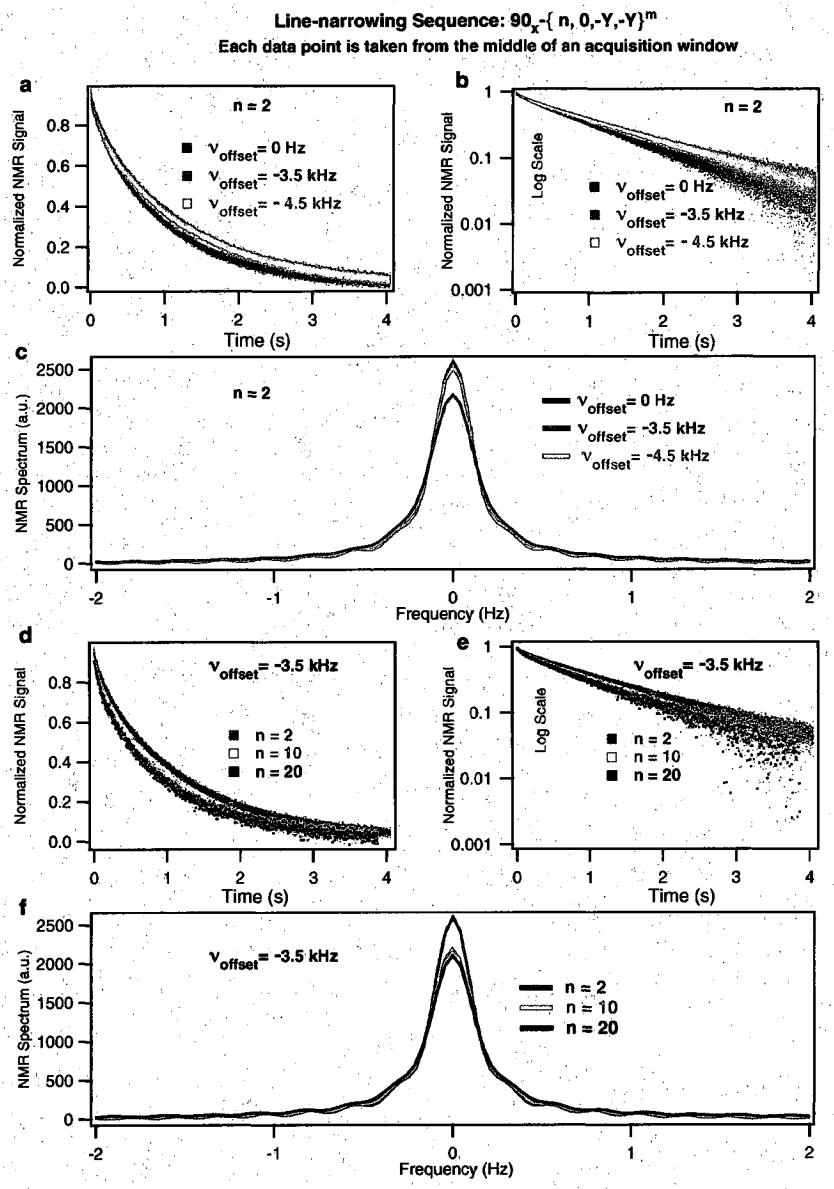

Figure 9.2: Sample C_{60}. The line-narrowing sequence gives similar performance for different value of n ($2 \leq n \leq 20$) and ν_{offset}^{global} ($2\pi|\nu_{offset}^{global}|/\omega_1 \leq 20\%$). Note that for simplicity, ν_{offset}^{global} is labeled as ν_{offset} in the figure legend. Other experimental parameters are the same as in Figure 9.1.

safely ignore it. But with our line-narrowing sequence, we managed to get rid of the coherence decay caused by both $\mathcal{H}_Z$ and $\mathcal{H}_{zz}$, so the previously obscured effect caused by the small fluctuating field may be detected. For buckballs, the spin lattice relaxation time T_1 [39, 87] is primarily due to the fluctuating magnetic fields arising from rapidly rotating buckyballs and the chemical shift anisotropy [23, 60, 84]. These effects also give rise to a T_2, which should be about 25 seconds if a single correlation time describes the buckyball motion [39, 84, 87]. However, our measured 1 second decay constant seems to be too short compared to the expected 25 seconds. In these line-narrowing experiments, the question is what is the limiting factor for the 1 second decay constant that we measured?

Later we learned from Tecmag, the manufacture of our spectrometer the Apollo, that the pulse synthesizer of the Apollo has a random phase drift which has an effect over a long pulse sequence, such as our line-narrowing sequence which lasts more than one second. Therefore, the 1 second decay constant we had measured in the line-narrowing sequence could be limited by the phase drift of the spectrometer. At that point, Tecmag loaned us a newer generation spectrometer, the LapNMR, which has longer phase coherence time in the synthesizer. Using the LapNMR, we repeated the line-narrowing experiments as shown in Figure 9.1 and Figure 9.2, and the decay constant was increased to about 12 seconds.

As it shows in Figure 9.3, the line-narrowing sequence with $n = 2$ and ν_{offset}^{global} =-3.5

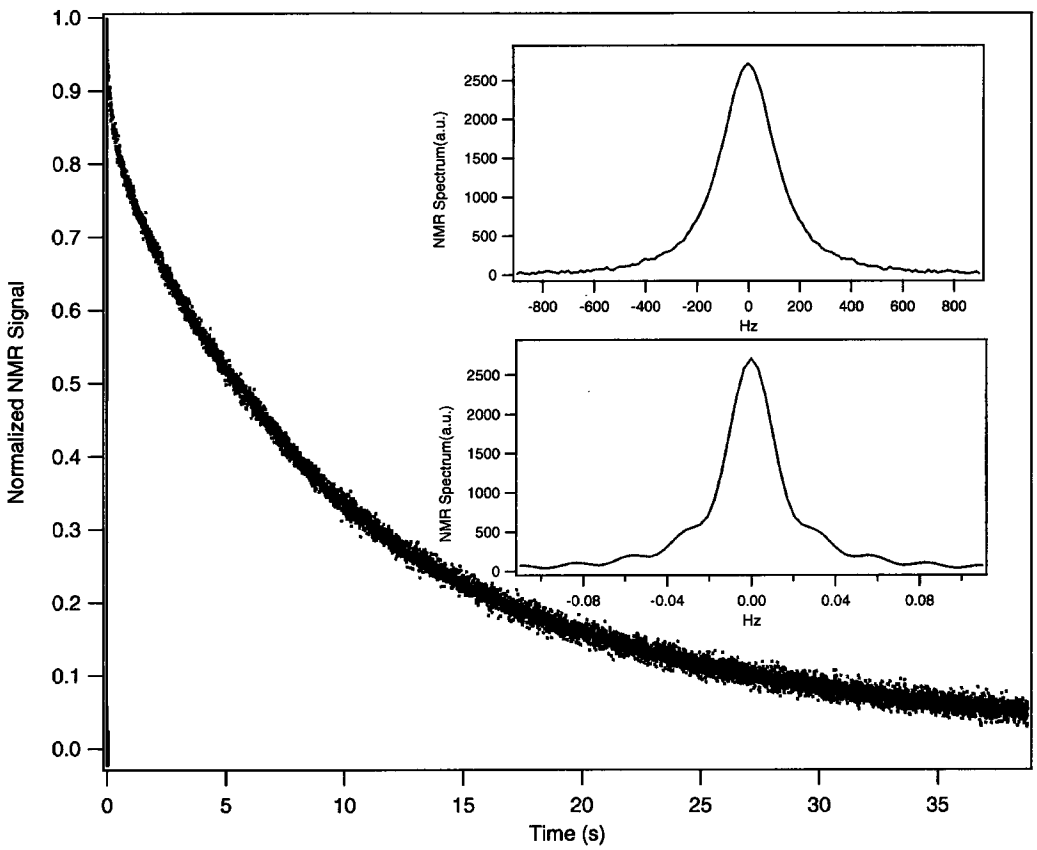

Figure 9.3: Repetition of the experiments in Figure 9.1 using the new spectrometer LapNMR with the same experimental parameters except m=96000. (Inset) The 260 Hz normal spectrum (red) is narrowed to approximately 0.03 Hz (blue).

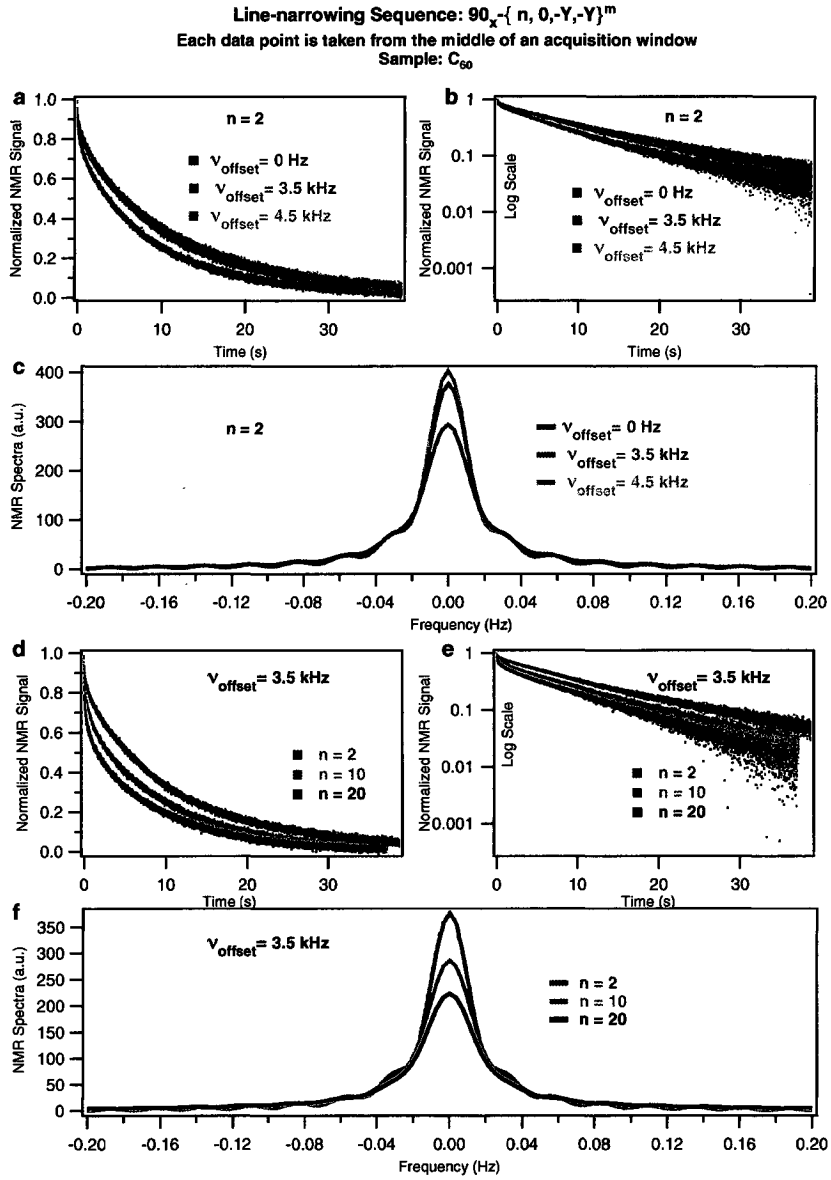

Figure 9.4: Repetition of the experiments in Figure 9.2 using the new spectrometer LapNMR with the same experimental parameters except m=96000. Experiments with different n and different ν_{offset}^{global} yield similar decay curves with a decay constant of 12 s. Note that for simplicity, ν_{offset}^{global} is labeled as ν_{offset} in the figure legend.

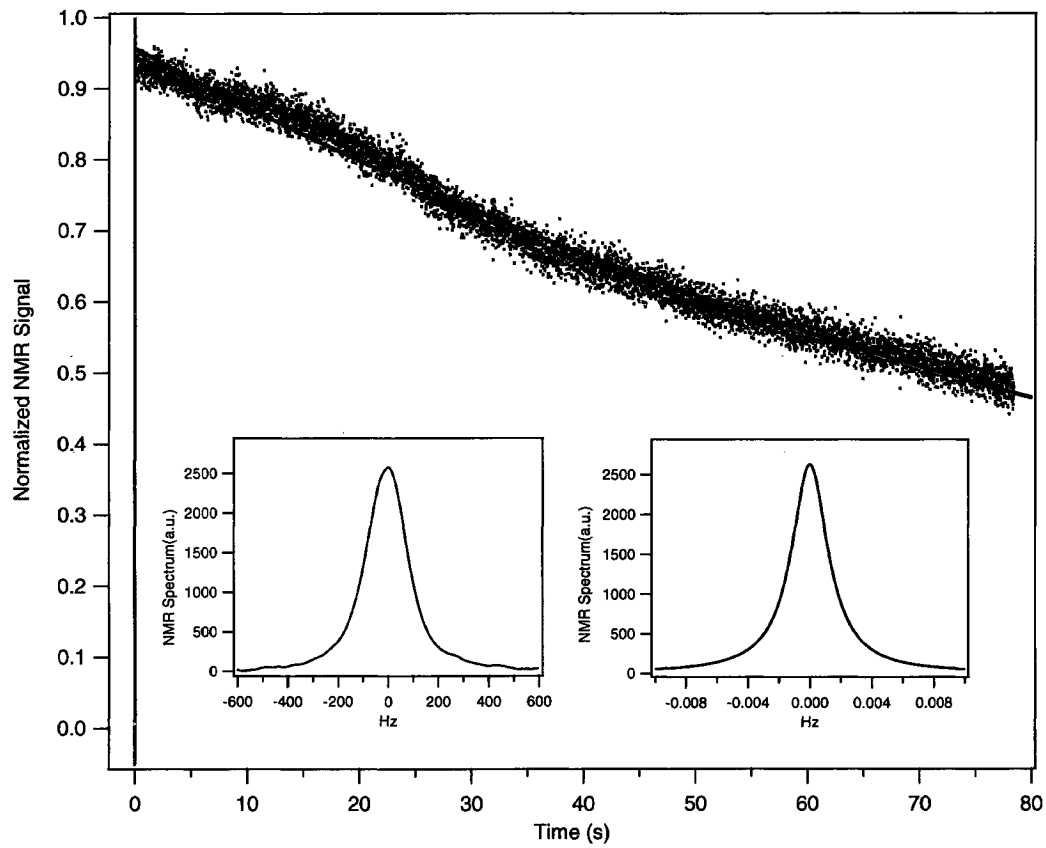

Figure 9.5: Experiments on Si:Sb (10^{17} Sb/cm^3) using the LapNMR. Comparison of the ^{29}Si time-suspension data using the sequence $90_X - \{2, 0, -Y, -Y\}^{84000}$ with $\omega_1/2\pi \approx$16.4 kHz, τ=60 μs, and ν_{offset}^{global}= 2.5 kHz (blue) and the normal ^{29}Si FID with ν_{offset}^{global}= 0 (red). The black curve is the corresponding fitting curve for the blue data, (a, Inset) The 200 Hz normal spectrum (red) is narrowed to 0.003 Hz (black, Fourier transformation of the fitting curve), centered at ν_{offset}^{global}.

kHz reduces the linewidth of the bullkyball sample from 260 Hz (Figure9.3, Inset red) to only about 0.03 Hz (Figure 9.1, Inset blue), a reduction of nearly 10,000, which is about fifty times better than the reduction that has been reported using magic angle spinning [82]. And again, different n ($2 \leq n \leq 20$) and different ν_{offset}^{global} yielded similar decay curves (Figure 9.4) with the decay constant of $\sim$ 12 seconds. This long decay constant is reasonably close to the 25 seconds decay constant caused by the T_1 relaxation time. These line-narrowing experiments demonstrate the potential use of this sequence to measure the very weak dephasing due the environment of the spin system which is normally obscured by $\mathcal{H}_Z$ and $\mathcal{H}_{zz}$.

We realized that if the line-narrowing experiments of C_{60} are limited by its T_1 relaxation, then this pulse sequence should give even better performance if it is applied to a similar sample but with a longer T_1. Indeed, when the line-narrowing sequence is applied to a Silicon sample (Si:Sb 10^{17} Sb/cm^3) with a comparable linewidth (200 Hz) but a longer T_1 =290 seconds, the measured decay time is 110 seconds (Figure 9.5), which is 10^{10} periods of Larmor precession. The normal linewidth has been narrowed by a factor of $\sim$70,000.

It is also important to point out the factors that need to be considered before using our line-narrowing approach. Our line-narrowing sequence applies many phase coherent and strong π pulses over a long time period. For example, the actual line-narrowing pulse sequence applied to Silicon in Figure 9.5 lasted longer than 75 seconds with more than 3×10^6 π pulses. This enormous number of strong, phase coherent

pulses presents two new problems that we do not need to worry about in typical NMR experiments. The first is the ability of the spectrometer to provide pulses of coherent phases and consistent magnitude over an anomalously long time. As discussed above, the slow phase drafting of Apollo turned out be the reason that limited the line-narrowing performance on C_{60}. This limitation of the Apollo was not a factor in more typical NMR experiments, including those presented in Dr. Dale Li's thesis [46] and Dr. Anatoly Dementyev's thesis [18]. Another new problem caused by the giant number of pulses is the RF pulse heating at room temperature. During the line-narrowing experiments, we used an oscilloscope to monitor the heating since significant heat in the RF tank circuit would affect its tuning property and a poor tuning will be observed on the oscilloscope. We always maintained good tuning (less than 10% reflected RF power [27]) during a line-narrowing experiment by reducing the pulse power and increasing the delay between two pulses if necessary. This is also the reason why the τ value of the Silicon line-narrowing experiment is larger than that used in other experiments.

Note that all the line-narrowing experiments presented above were using 90_X as the first tipping pulse, followed by the repeating block $\{2, 0, -Y, -Y\}$. Based on Equation (9.1), which was derived with approximations such as dropping the non-secular dipolar terms in $\bar{\mathcal{H}}^{(0)}$ and combining $\{X, X\}$ and $\{-X, -X\}$ to cancel out $\bar{\mathcal{H}}^{(1),non-I_{x_T}}_{\{X,X\}}$ in $\bar{\mathcal{H}}^{(1)}$, 90_X and 90_Y should lead to the same line-narrowing performance. However, in experiments only 90_X works well and 90_Y would lead to a fast decay, as

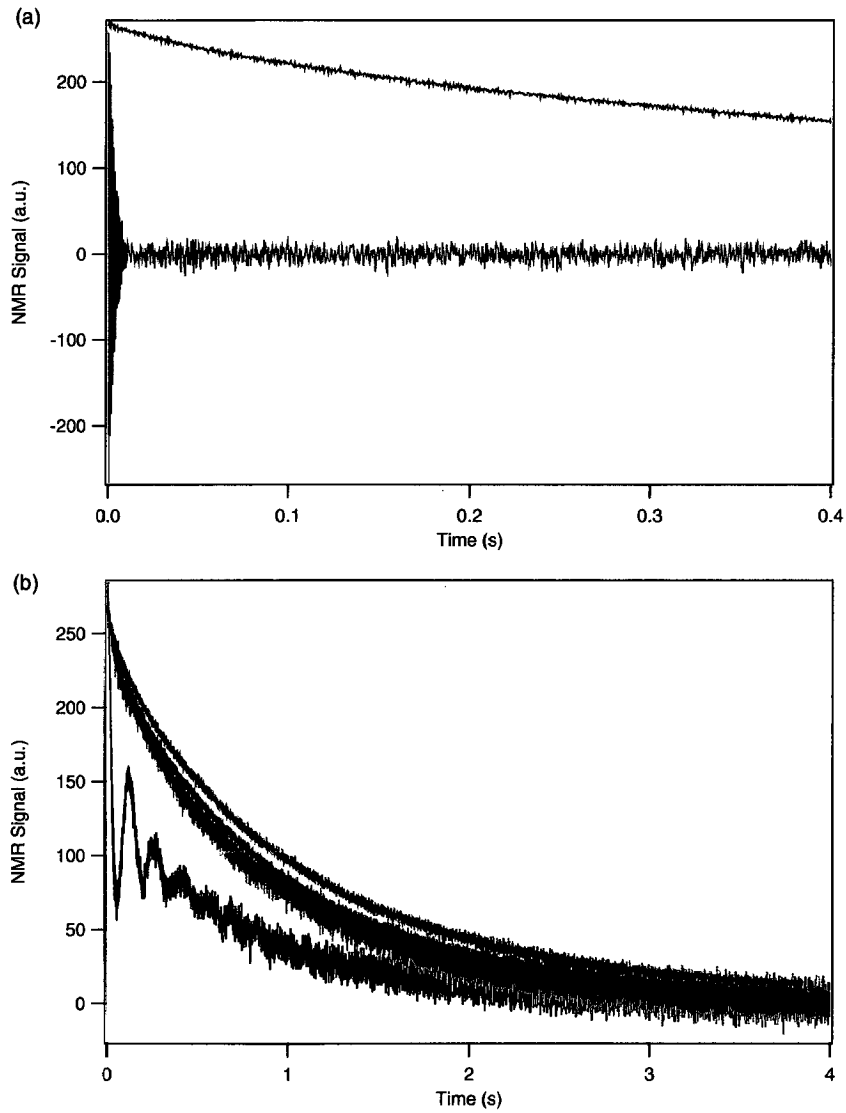

Figure 9.6: Sample: C_{60}. (a) The comparison of experiments using sequence $90_X - \{2,0,-Y,-Y\}^m$ (red) and $90_Y - \{2,0,-Y,-Y\}^m$ (grey), with ν_{offset}^{global}= 0 Hz. (b) The comparison of experiments using $90_Y - (\{2,0,-Y,-Y\} - \{2,0,+Y,+Y\})^m$ (black trace for ν_{offset}^{global}= 0 Hz, and purple trace for ν_{offset}^{global}=-3.5 kHz) and $90_X - \{2,0,-Y,-Y\}^m$ (red trace for ν_{offset}^{global}= 0 Hz, and blue trace for ν_{offset}^{global}=-3.5 kHz). Experiments were performed on the spectrometer Apollo, with $\omega_1/2\pi \approx$25 kHz, τ=22 μs.

shown in Figure 9.6 (a) (only ν_{offset}^{global}=0 is shown here. The result is the same for $|\nu_{offset}^{global}| \leq$3.5 kHz). This discrepancy is due to the limitations of the approximation we have made to reach Equation (9.1). For example, in $\bar{\mathcal{H}}^{(1)}$ of the repeating block $\{2, 0, -Y, -Y\}$, there is a term proportional to I_{y_T}, which may help preserve the signal when the initial density matrix is I_{y_T} after the first tippling pulse 90_X is applied. Furthermore, the non-secular terms in $\bar{\mathcal{H}}^{(0)}$ may also contribute to the selection of the first tipping pulse.

Moreover, Equation (9.1) suggests that $\{2, 0, +Y, +Y\}$ should behave just like $\{2, 0, -Y, -Y\}$. However, experiments using the sequence $90_X - (\{2, 0, -Y, -Y\} - \{2, 0, +Y, +Y\})^m$ gives a fast decay curve, instead of the excellent line-narrowing effect achieved with sequence $90_X - \{2, 0, -Y, -Y\}^m$ as shown in Figure 9.3 and Figure 9.5. Trying to understand these discrepancies with our first model (Equation (9.1)), we realized that the non-zero duration of the 90° wrapper pulses plays a non-negligiable role. Including the duration of the 90° wrapper pulses, the average Hamiltonian calculation shows that these wrapper pulses contribute to a term $\mathcal{H}' = \frac{2}{\omega_1}\Omega_z^{net} I_{x_T}(1 + p)$ in $\bar{\mathcal{H}}^{(0)}$, where $p = -1$ for repeating block $\{2, 0, -Y, -Y\}$ (hence $\mathcal{H}' = 0$) and $p = 1$ for repeating block $\{2, 0, -Y, -Y\} - \{2, 0, +Y, +Y\}$. This extra term $\frac{4}{\omega_1}\Omega_z^{net} I_{x_T}$ for repeating block $\{2, 0, -Y, -Y\} - \{2, 0, +Y, +Y\}$ favors the choice of 90_Y because it helps preserve the initial density matrix I_{x_T} right after the tipping pulse, while make I_{y_T} nutate in the Y-Z plane [84]. Figure 9.6 (b) shows the comparison of experiments using $90_Y - (\{2, 0, -Y, -Y\} - \{2, 0, +Y, +Y\})^m$ and

$90_X - \{2, 0, -Y, -Y\}^m$. For ν_{offset}^{global}=0, the $\mathcal{H}'$ term is small since $\Omega_z^{net} = \Omega_z^{loc}$; therefore the curve generated by $90_Y - (\{2, 0, -Y, -Y\} - \{2, 0, +Y, +Y\})^m$ (black) is not as good as that generated by $90_X - \{2, 0, -Y, -Y\}^m$ (red). But it is still much better than the fast decay generated by $90_Y - \{2, 0, -Y, -Y\}^m$ in Figure 9.6 (grey). Please note the different time scale in Figure 9.6 (a) and (b). For ν_{offset}^{global}=-3.5 kHz, sequence $90_Y - (\{2, 0, -Y, -Y\} - \{2, 0, +Y, +Y\})^m$ (purple) has almost as good performance as sequence $90_X - \{2, 0, -Y, -Y\}^m$ (blue), because the term $\mathcal{H}'$ is much bigger and can effectively help preserve I_{x_T}. Note that all the experiments presented in Figure 9.6 were done on the Apollo.

For the design of the sequences for MRI of solids in the next section, the non-zero duration of the 90° wrapper pulses were taken into account in the AHT analysis and data-processing.

9.2 Application: MRI of Solids

One of the important applications of NMR technique is magnetic resonance imaging (MRI), which was first proposed by Lauterbur [45], and by Mansfield and Grannell [56]. The basic concept of MRI is transforming the spacial information into frequency domain, and the image is obtained through measuring the Zeeman shifts on a fine spatial scale using the back-projection technique [45, 56]. A simple illustration of the back-projection technique can be found in Figure 9.7, which is borrowed from Lauterbur's original publication [45].

MRI: Back Projection

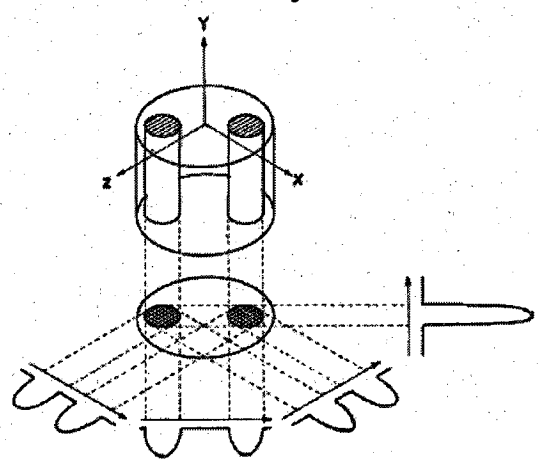

Fig. 1 Relationship between a three-dimensional object, its two-dimensional projection along the Y-axis, and four one-dimensional projections at 45° intervals in the XZ-plane. The arrows indicate the gradient directions.

P.C.Lauterbur Nature Vol.242 1973

Figure 9.7: A simple illustration of the technique of back projection in MRI, proposed by P. C. Lauterbure [45].

Our theory of the $\{n, \delta, \psi_1, \psi_2\}$ block suggests that the Zeeman shift can be directly measured, provided that $\psi_1 = \psi_2$, $\delta \neq 0$. This property indicates that this block can be used in the MRI [16, 58, 65] or microscopy [29] of solids , since we can measure pure Zeeman shift information without dipolar dephasing. MRI of solids has been accomplished in several ways [16, 58, 65]. Typically, the burst used to eliminate the dipolar dephasing requires $\nu_{offset}^{global} = 0$ Hz for optimum performance, which constrains the timing and magnitude of gradient pulses in these experiments [16]. Sequences based on the quadratic echo offer another solution to this problem, since they work well over a wide range of $|\nu_{offset}^{global}|$ values.

A constant linear magnetic field gradient across a uniform test sample produces a spread in Ω_z^{net}, which results in a Zeeman spectrum with a top-hat shape. Measuring this spectrum is the first step toward imaging, using the back-projection technique [45, 56, 84]. To mimic the top-hat shape, we used a discrete set of ν_{offset}^{global} values to move the narrow C_{60} spectrum to particular off-resonance positions.

Our first try of the experimental implementation of the MRI sequence $\{n, \delta, \psi_1, \psi_2\}$ with n=10 and $\psi_1 = \psi_2 = -Y$ was not successful. It looked like the terms that we neglected in our model had non-negligible effects, which distorted the spectrum.

Using the big repeating block $\{2, \delta, -Y, -Y\}\{2, -\delta, Y, Y\}$ we get a fairly good top-hat spectrum as it is shown in Figure 9.8. Ideally, every spectrum in Figure 9.8 should have the same line shape and magnitude at the targeted frequency. For the

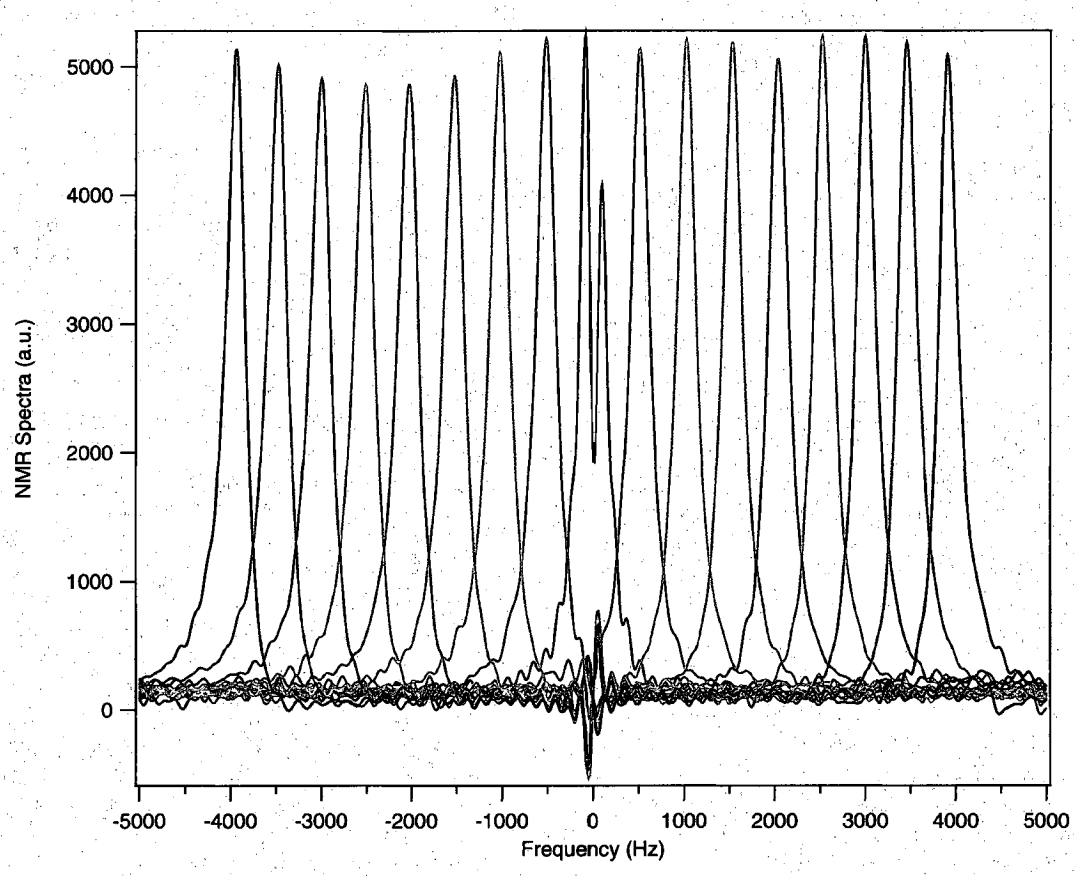

Figure 9.8: Experiments on C_{60} using the Apollo. The Reproduction of a top-hat lineshape produced by the sequence $90_X - \{2, 0, -Y, -Y\} - \{\{2, -\delta, -Y, -Y\}\{2, +\delta, Y, Y\}\}^m$, with m=29, $\omega_1/2\pi \approx$25 kHz, τ=22 μs, and δ=30 μs. Each trace is the measured spectrum of a pseudo-FID with different ν_{offset}^{global}, for -4 kHz$\leq \nu_{offset}^{global} \leq$+4 kHz in steps of 500 Hz.

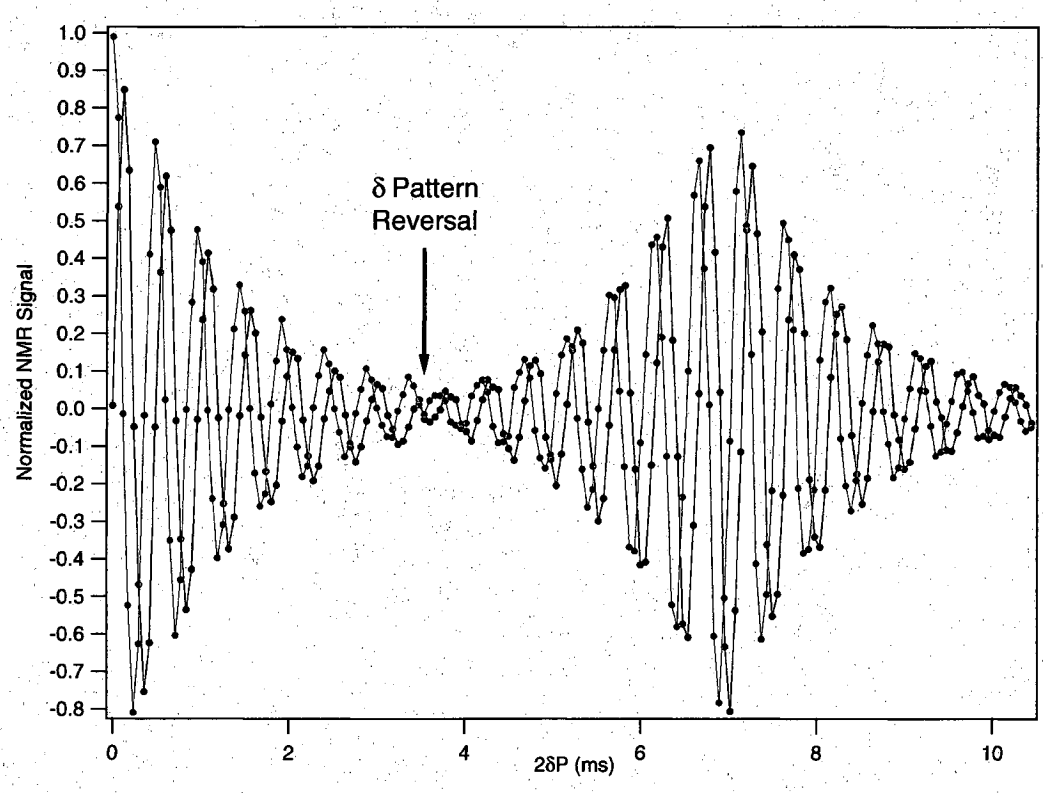

Figure 9.9: The pseudo-Hahn echo experiment on C_{60} using the Apollo. The pulse sequence is $90_X - \{2, 0, -Y, -Y\} - \{\{2, -\delta, -Y, -Y\}\{2, +\delta, Y, Y\}\}^{m_1} - \{\{2, +\delta, -Y, -Y\}\{2, -\delta, Y, Y\}\}^{m_2}$, with m_1=29, m_2=58, ν_{offset}^{global}=-2 kHz, $\omega_1/2\pi \approx$25 kHz, τ=22 μs and δ=30 μs. The $\langle I_{y_T} \rangle$ (red) and $\langle I_{x_T} \rangle$ (black) signals acquired after each block are plotted versus the net Zeeman phase wrapping time 2δP, where P=0,1,2,3... The pseudo-Hahn echo is induced by a reversal of the δ-pattern in the m_2 blocks, after the initial pseudo-FID in the m_1 blocks.

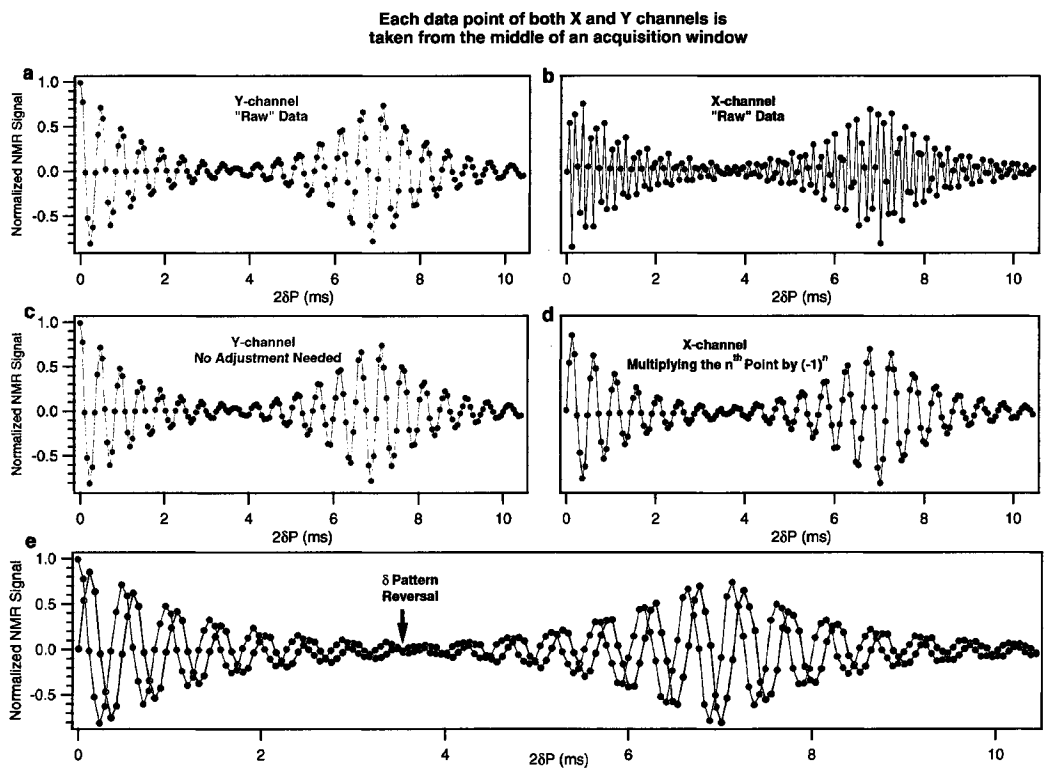

Figure 9.10: The data-processing steps to obtain the Pseudo-Hahn echo in Figure 9.9

actually data, every spectrum (except the red trace with ν_{offset}^{global}=0 Hz) in Figure 9.8 has reasonably similar line shape and magnitude. However, this sequence still did not work as desired for ν_{offset}^{global}=0 Hz because with ν_{offset}^{global}=0 Hz, the transverse field term that we use in our model to make the second averaging approximation goes to zero.

Each spectrum in Figure 9.8 is the Fourier transformation of a pseudo-FID, which is acquired at a particular ν_{offset}^{global}. In a similar manner of generating a Hahn echo, the decay of the pseudo-FID can also be reversed, generating a pseudo-Hahn ehco. This is demonstrated in Figure 9.9. The signals oscillate as expected for ν_{offset}^{global}=-2 kHz, and decay to zero during the first m_1 blocks, which we refer to as a pseudo-FID. This may be understood using our theory, since the $\{n, +\delta, \psi_1, \psi_2\}$ block has the unitary operator $\mathcal{U}_{180_Y} e^{-\frac{i}{\hbar}(\Omega_z^{net} I_{z_T})(+2\delta)}$ (Equation (9.1)), where the $\mathcal{U}_{180_Y}$ inverts both I_{x_T} and I_{z_T}. To account for the effect of $\mathcal{U}_{180_Y}$, we multiply the n^{th} echo in the X-channel by $(-1)^n$, and use the pattern of a $+\delta$ block followed by a $-\delta$ block (Figure 9.10). Then, we reverse that δ pattern, which causes a pseudo-Hahn echo to emerge and decay away during the m_2 blocks, just as our theory predicts. This is a new kind of echo, since it is not induced by a π pulse (as in the normal Hahn echo [36]), or even by a pulse phase pattern reversal (as in the echo of the echo train in Figure 8.1(C)).

To improve upon the MRI sequence used in Figure 9.8, we computed the average Hamiltonian of this composite block $\{2, \delta, -Y, -Y\}\{2, -\delta, Y, Y\}$ including the non-zero duration of the 90° wrapper pulses. We found that repeating block $\{2, 0, -Y, Y\}$

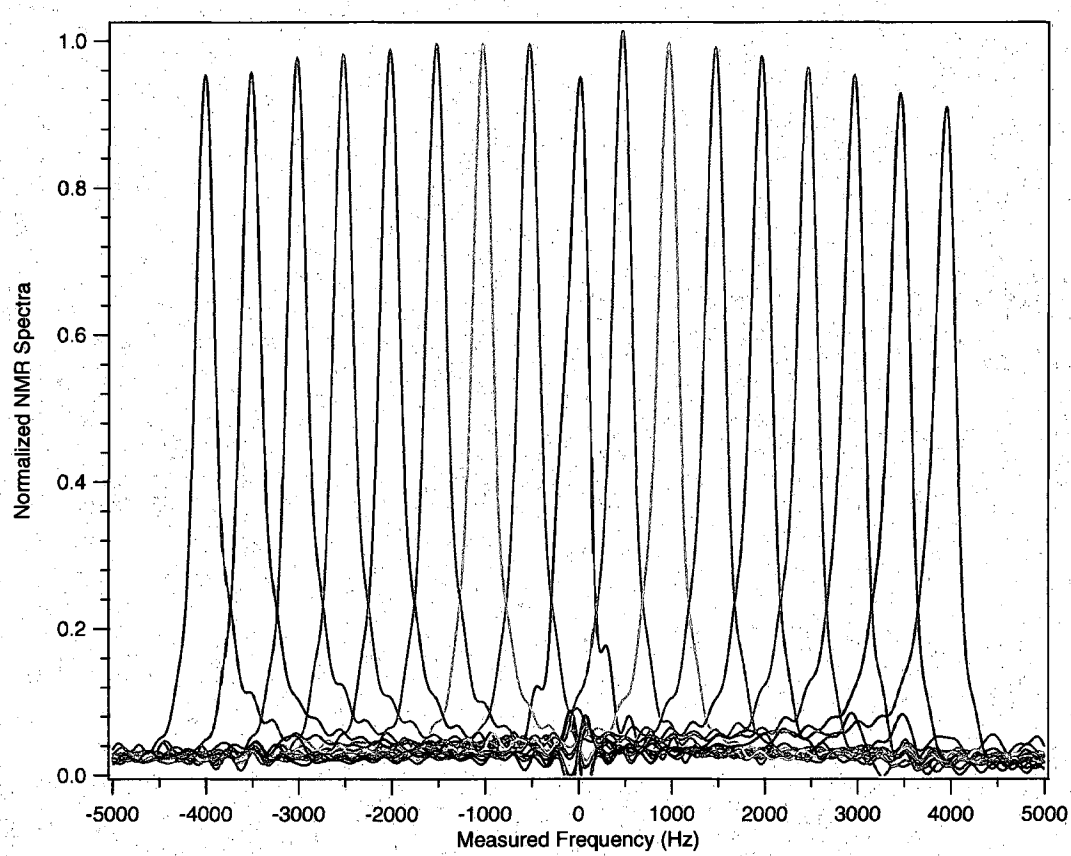

Figure 9.11: Experiments on C_{60} using the Apollo. Reproduction of a top-hat lineshape using sequence $90_X - \{2, t_0, -Y, -Y\} - \{2, 0, -Y, Y\}^{30}$ with $\omega_1/2\pi \approx 25$ kHz, τ=22 μs, and t_0=0. Each trace is the measured spectrum of a pseudo-FID with different ν_{offset}^{global}, for -4 kHz$\leq \nu_{offset}^{global} \leq$+4 kHz in steps of 500 Hz, covering the range $2\pi|\nu_{offset}^{global}|/\omega_1 \leq 16\%$. To obtain this full bandwidth, the pseudo-FID interleaves a second data set using the same sequence, but with $t_0 = -(\frac{\Delta}{2} + \frac{1}{2\omega_1})$.

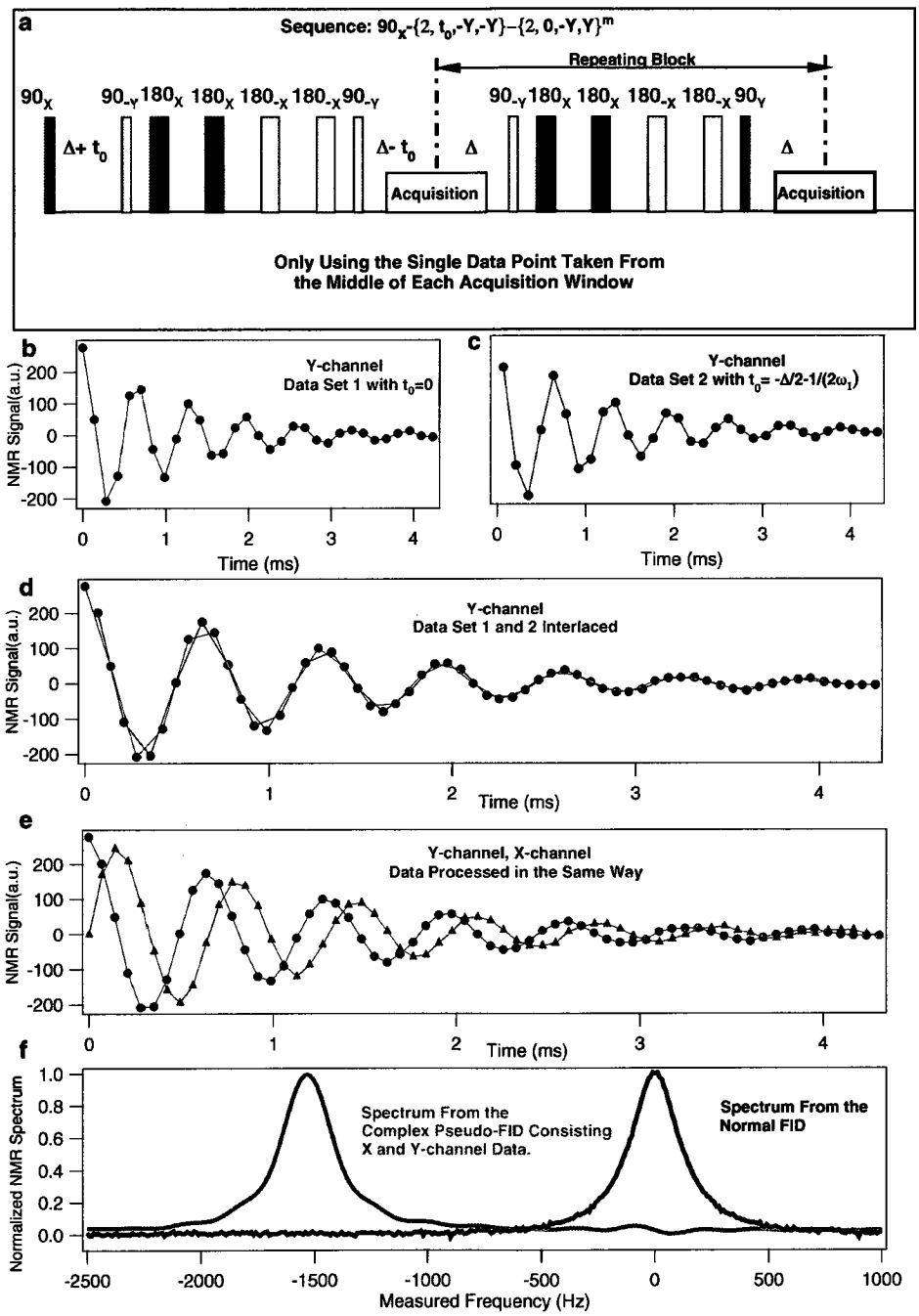

Figure 9.12: The data-processing steps to obtain one spectrum for the MRI top-hat lineshape in Figure 9.11.

may give better performance since the phase pair Y and -Y for the 90° pulses can actually contribute a transverse field term that helps in the second averaging approximation for ν_{offset}^{global}=0 Hz, improving on the "hole" at ν_{offset}^{global}=0 in Figure 9.8.

Indeed, the experiment confirmed our prediction. Figure 9.11 shows a more faithful reproduction of the input top-hat spectrum, including ν_{offset}^{global}=0 Hz [59]. Each spectrum is the Fourier transformation of the pseudo-FID resulting from two interlaced data sets. We had to use two interlaced data sets to achieve the desired frequency resolution because of the relatively large time step in the pseudo-FID. The details in processing the data are shown in Figure 9.12. Note that for the pseudo-FID in Figure 9.12 (b) and (c), the time spacing between two adjacent points is set to be $2\Delta + 2/\omega_1$, where $2/\omega_1$ is due to the non-zero duration of the 90° wrapper pulses as derived from the average Hamiltonian $\bar{\mathcal{H}}^{(0)}$. For our experimental conditions, $\Delta \approx$64 μs and $2/\omega_1 \approx$13 μs. Therefore, if the duration of the 90° wrapper pulses was ignored, the frequency reproduced in Figure.9.11 would be about 10% off. When the duration of the 90° wrapper pulses are taken into account, Figure.9.11 shows that both the signal amplitude and the ν_{offset}^{global} values have been quite accurately reconstructed in this approach.

The MRI block $\{2, 0, -Y, Y\}$ used in Figure 9.11 looks a lot like the "magic sandwich echo" demonstrated by S. Matsui [58]. But these two approaches are different despite that they are both designed to work as dipolar decoupling blocks. The magic sandwich echo uses continuous long pulses within the burst, while we use discrete π

pulses. Moreover, the magic sandwich echo works the best with Ω_z=0, which requires the filed gradient to be turned off during the decoupling block; while our approach works the best with $\mathcal{H}_z \geq \mathcal{H}_{zz}$ and hence the field gradient can be left on all the time, which enables the application of large field gradients at moderate cost. It should also be possible to implement standard frequency- and phase-encoding methods using this approach [16, 84].

9.3 Towards 3D Imaging: Slice Selection

The technique of slice selection is a critical step to achieve 3D nuclear magnetic imaging. In this section, our efforts towards slice selection will be presented.

One method to achieve selective excitation in Fourier Transform NMR is called Delays Alternating with Nutations for Tailored Excitation (DANTE) [66]. This pulse sequence consists of n identical short pulses (e.g., along the X direction in the rotating frame) with each flip angle $\alpha \ll \pi/2$ radians and $n\alpha = \pi/2$, separated by a delay τ'. To understand how the DANTE sequence works, let us follow the motion of a macroscopic magnetization vector M at a frequency offset $\delta\nu$ from the transmitter. In the absence of dipolar coupling, each short α pulse can be approximated as a pure rotation and each delay τ' can be approximated as a precession around the effective field $\delta\nu/\gamma$ along the Z-axis in the rotating frame. Therefore, magnetization M nutates α radians about the X-axis during each short pulse, and precesses about the Z-axis with an angle of $2\pi\delta\nu\tau'$. It can be seen that if M precesses an integral

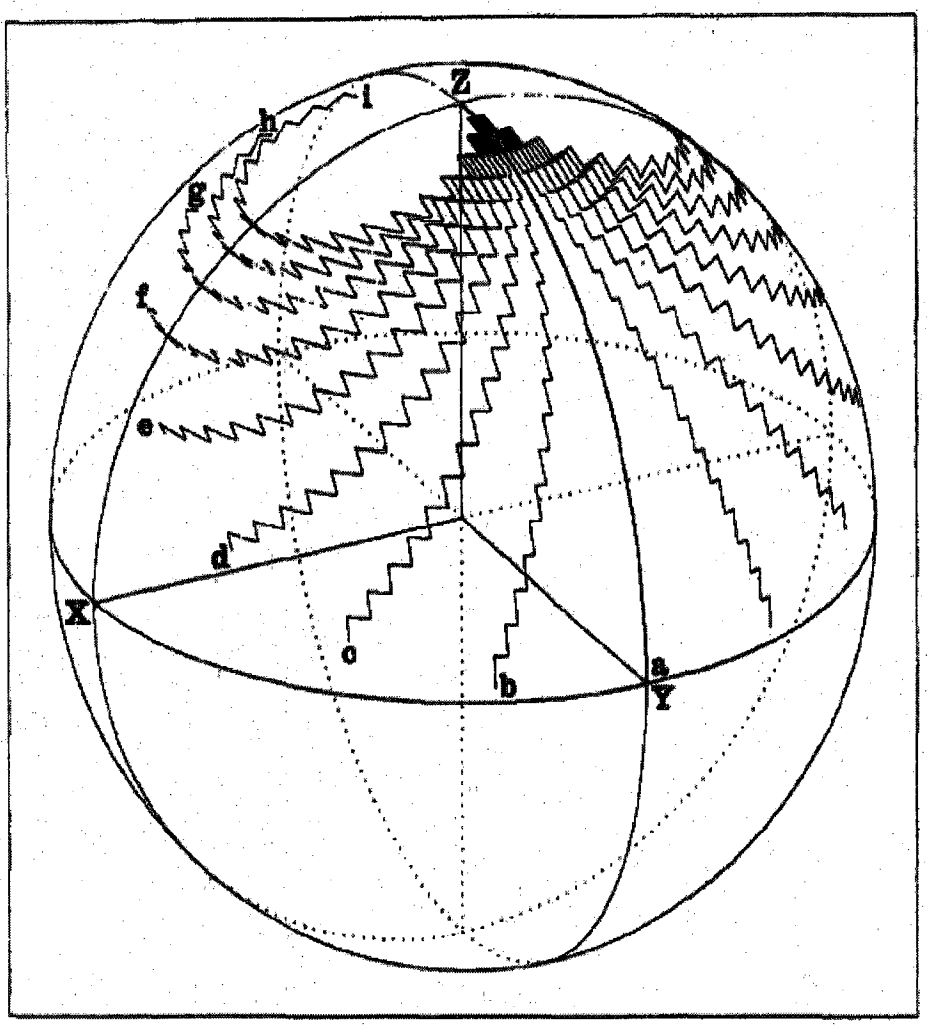

Figure 9.13: Figure and Caption from the reference [66]. Trajectories of magnetization vectors computed according to the Bloch equations and viewed in a frame of reference rotating at the "first sideband" frequency, $\nu_0 + 500$ Hz. The excitation was a train of twenty pulses of flip angle $\pi/40$ radians each, spaced 2 msec apart. Trajectory (a) represents magnetization exactly 500 Hz above the transmitter frequency ν_0 and it experiences a cumulative nutation of $\pi/2$ radians with no net precession between pulses. Trajectories (b) through (i) represent increasing offsets in steps of 2.5 Hz up to a total of 520 Hz above ν_0, the unlabeled trajectories representing the corresponding offsets below 500 Hz.

number of complete revolutions around the Z-axis during the delay τ', i.e. $\delta\nu = k/\tau'$ (k is an integer), M will remain in the Y-Z plane during each successive pulse blip and a cumulative rotation of $\pi/2$ about the X-axis will be achieved. Therefore, in the Fourier Transform spectrum only those resonances that are offset from the transmitter frequency by $\delta\nu = k/\tau'$ Hz (k is an integer) are excited to a significant extent.

Figure 9.13 together with its caption is from the article titled "Seletive Excitation in Fourier Transform Nuclear Magnetic Resonance" by Gareth A. Morris and Ray Freeman [66]. This Figure illustrates the trajectories of different offset $\delta\nu$ for a sequence of 20 pulses with $\alpha = \pi/40$ and $\tau' = 2$ms. This first sideband condition is thus $\delta\nu = 500$ Hz and the rotating frame is chosen to synchronize with the first sideband at $\nu_0 + 500$ Hz. The magnetization vector M for $\delta\nu = 500$ Hz will remain in the Y-Z plane and will be rotated from the Z-axis to the Y-axis after 20 small pulse kicks. Vectors greater than 25 Hz away from $\delta\nu = 500$ Hz will from nearly circular trajectories near the Z-axis, leaving no significant component in the transverse plane, i.e. no significant excitation. Therefore, only a small range of resonance frequencies around $\delta\nu = 500$ Hz will be excited and contribute to the magnetization in the transverse plane. The DANTE sequence was first shown to work in the NMR of liquids. To apply DANTE to solids, one needs to "turn off" the dipolar coupling.

We tried to combine the DANTE sequence and our imaging block $\{2, 0, -Y, Y\}$ used in Figure 9.11 to achieve slice selection in solids. Figure 9.15 shows the slice

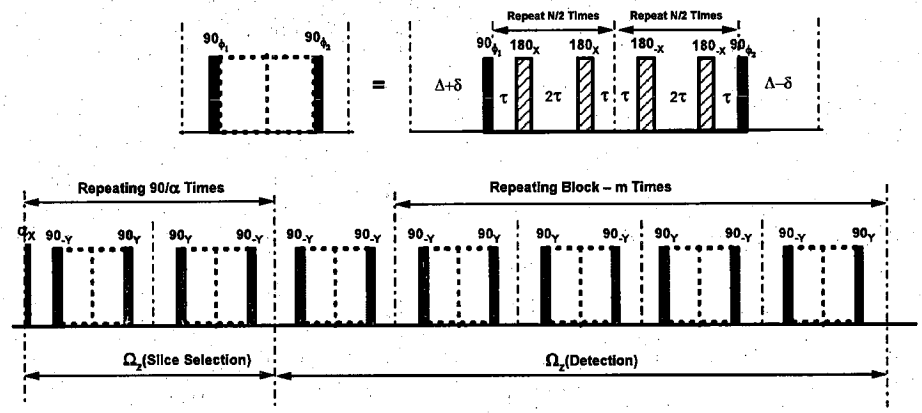

Figure 9.14: The pulse sequence used for the slice selection data presented in Figure 9.15

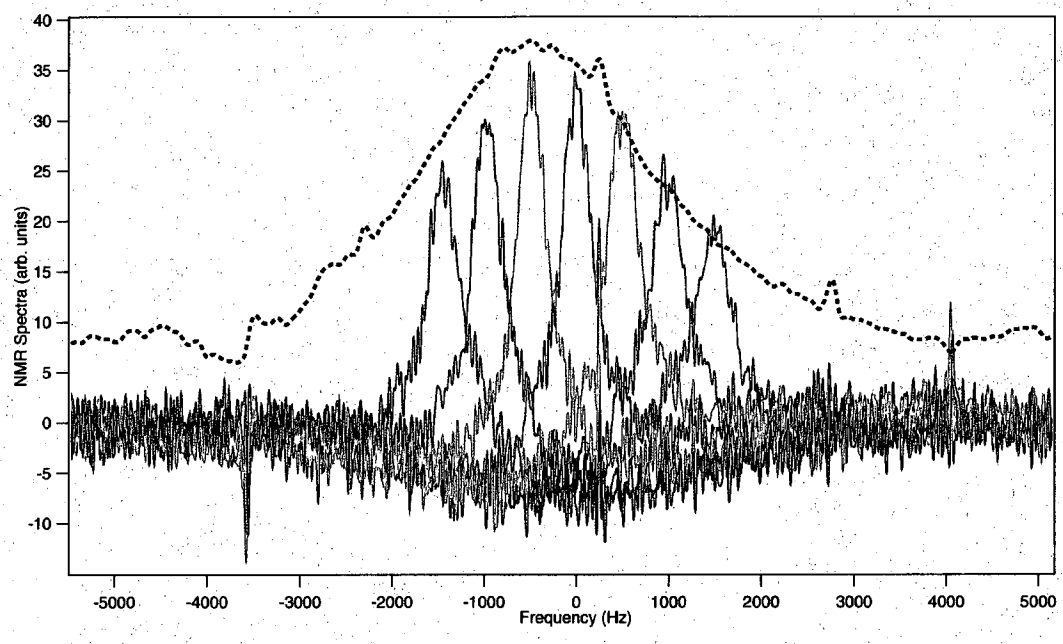

Figure 9.15: The demonstration of slice selection using the pulse sequence described in Figure 9.14. The data were acquired with ^{31}P in a sample of human teeth. Each slice was the Fourier Transformation of a pseudo-FID obtained with a different ν_{offset}^{global}, 0 Hz (red), $\pm$500 Hz (yellow), $\pm$1000 Hz (green), and $\pm$1500 Hz (blue). The black curve was the the reference spectrum obtained though the pseudo-FID acquired using the pulse sequence with a hard 90° replacing the DANTE 90°. $\omega_1/2\pi$=4.3 kHz for the small $\alpha = 4.5°$ pulses, $\omega_1/2\pi$=28.9 kHz for all other pulses, and τ=5 μs. Data taken at room temperature in a field of 12 Tesla with Lamor frequency of 206.945 MHz.

selection data obtained using the pulse sequence described in Figure 9.14. The back dash-line is the "full" spectrum (containing only Zeeman linewidth) obtained by replacing the DANTE 90° pulse by a hard 90°. The color traces are the few slices selected by a chosen ν_{offset}^{global} value. Note that the side band we chose to observe here is $k = 0$ in the formula $\delta\nu = k/\tau'$ (k is an integer) discussed above [66]. Even though the slices are far from being perfect, each trace is clearly a small slice of the "full" spectrum and the magnitude of the slices also follows the overall shape of the black. Our slice selection sequence discussed here is not necessarily better than some other sequences that have been done before [12], but it offers a different approach based on our understanding of the multiple pulse sequences. Further efforts will be devoted to improve this slice selection technique in the future, such as observing the sideband of $k = 1$ using alternating α_X and α_{-X} kicks [12].

9.4 Limits of This New Approach to Coherence Control

Since the conditions assumed in our model may not be achievable for many samples, we consider the following limits on our approach.

First, in analysis we assumed uniform pulses for the small samples with low coil filling factors used in our experiments, while in reality pulse strength varies across a big sample. Fortunately, our experiments show that an intentional uniform misadjustment of all pulse angles leads to similar line-narrowing performance (Figure

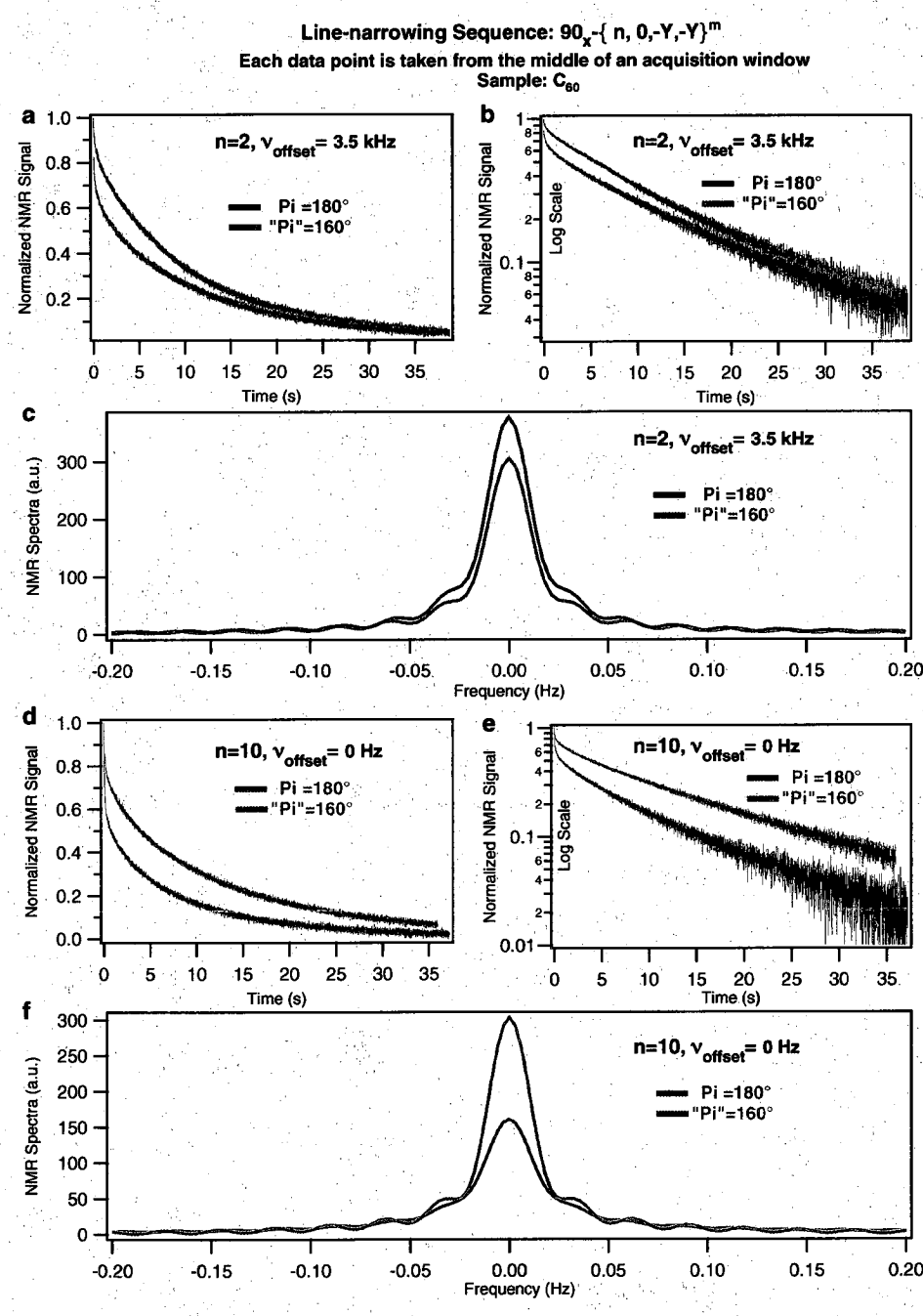

Figure 9.16: The slow exponential signal decay observed with our line-narrowing sequence is similar even when there is an intentional uniform misadjustment of all pulse angles. (a-c) with n=2 and ν_{offset}^{global}=-3.5kHz; (d-f) with n=10 and ν_{offset}^{global} =0 Hz. Experiments were carried out on C_{60} using the LapNMR.

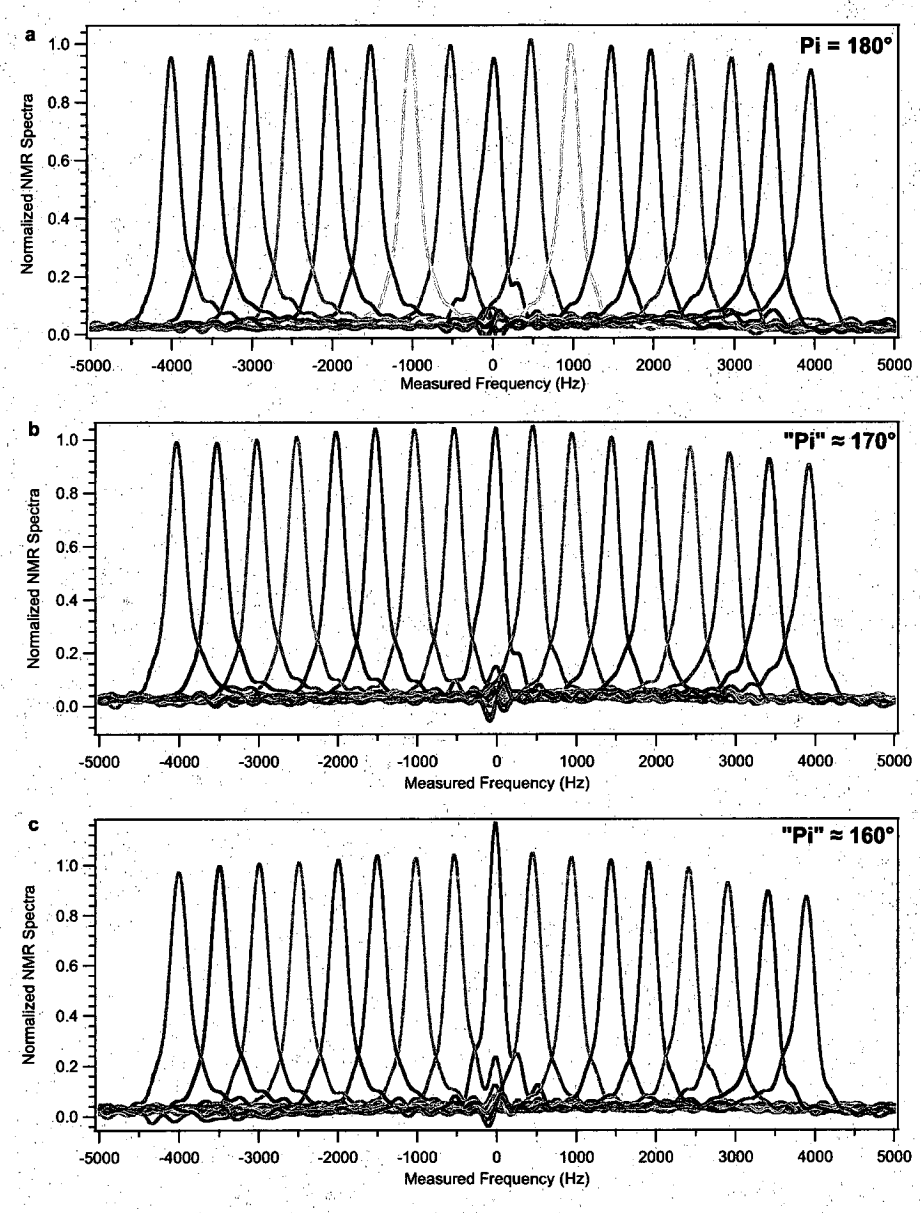

Figure 9.17: (a) The MRI top-hat lineshape in Figure 9.11 uses optimized pulse angles (Pi=180°). (b,c) An intentional uniform misadjustment of all pulse angles leads to similar MRI top-hat lineshapes. Experiments were carried out on C_{60} using the Apollo.

9.16) and similar MRI boxtop lineshapes (Figure 9.17), which suggests that these two applications are not very sensitive to pulse errors.

Second, for the experiments presented in this Chapter our model requires that $\| \mathcal{H}_Z \| \geq \| \mathcal{H}_{zz} \|$. While it is true that for many important nuclei, such as protons, the dipolar broadening dominates the magnetic broadening, the condition $\| \mathcal{H}_Z \| \geq \| \mathcal{H}_{zz} \|$ can still be reached by using a non-zero ν_{offset}^{global}. This is demonstrated in the proton NMR experiments performed by Rona G. Ramos using Adamantane (Figure 9.18). While these preliminary results are promising, the $\bar{\mathcal{H}}^{(0)} + \bar{\mathcal{H}}^{(1)}$ theory presented in this thesis does not apply, because the AHT expansion parameter $\| \mathcal{H}_{int} \| t_c$ is about ten times larger than the value used in our C_{60} experiments, and higher order correction terms are needed. Shorter t_c, which has been limited by our current spectrometer, is required to improve the experiments toward our model. Future work will use microcoils [68, 80, 93] to reach even shorter t_p and t_c, which should improve the utility of our model for proton NMR experiments.

Third, in our model we assume strong pulses. For those interesting NMR applications with weak pulse strength, our model does not apply since the parameter $\| \mathcal{H}_{int} \| t_c$ is so large that the Magnus expansion will not converge quickly, if at all.

Our sequences may help in the study of some important biomaterials, since the assumed $\mathcal{H}_{int}$ here is very similar to that of ^{31}P in bones and teeth [92, 91]. Preliminary results are encouraging [75].

In conclusion, coherence can be manipulated using the non-zero duration of strong

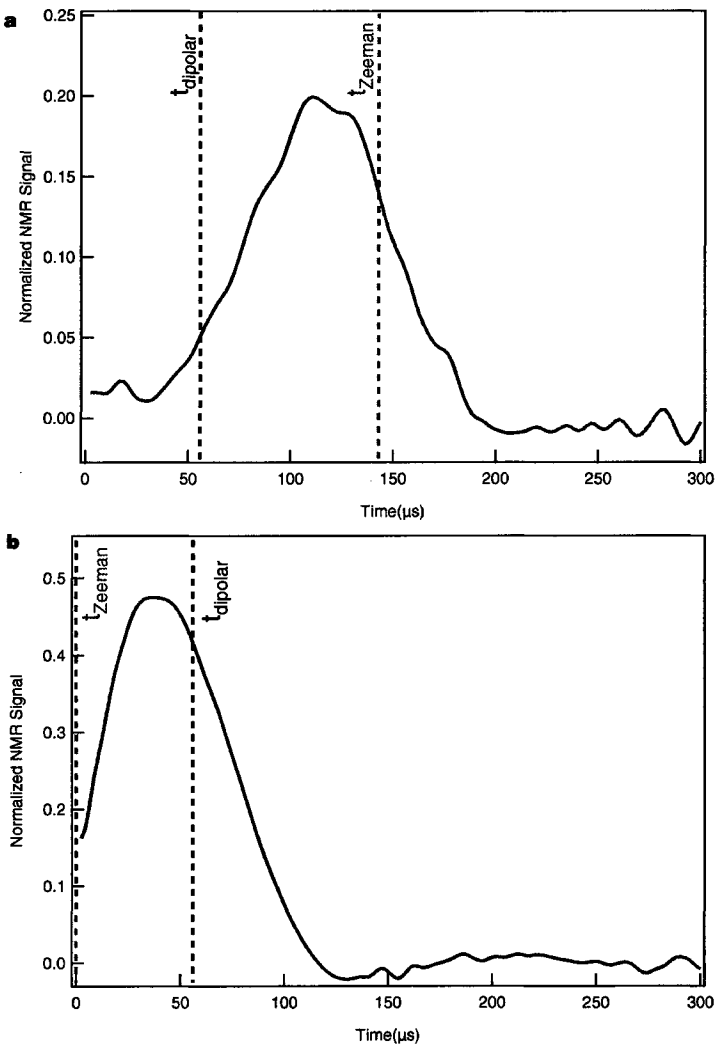

Figure 9.18: Proton NMR in adamantane ($C_{10}H_{16}$) using the Apollo. (a) An echo using the sequence $\{-X, X\}^n - 90_X$, as in Figure 8.2, but with ν_{offset}^{global}= -25 kHz. (b) An improved echo using the composite sequence $\{-X, X\}^{n/2} - \{X, -X\}^{n/2} - 90_{-X}$ and ν_{offset}^{global}= 25 kHz. Both (a) and (b) use n=20 and τ=5.6 μs. The pulse strength $\omega_1/2\pi$=89.3 kHz is approximately 6 times bigger than the 15 kHz linewidth of ^{1}H in adamantane, with a 127.79 MHz Larmor frequency at a 3 Tesla magnetic field at room temperature.

π pulses in repeating blocks of the form $(\tau - 180_{\phi_1} - 2\tau - 180_{\phi_2} - \tau)$. Terms up through first-order in the average Hamiltonian expansion have been used to carry out analogs of well-known NMR spin echo experiments. Related effects can occur for a wider variety of $\mathcal{H}_{int}$ and $\mathcal{H}_{p_\phi}$ than we have treated here, provided that $[\mathcal{H}_{p_\phi}, \mathcal{H}_{int}] \neq 0$. Shaped pulses, soft pulses, and strongly-modulated pulses have proven to be important elements of the NMR toolbox. Exploiting the internal structure of strong π pulses provides experimentalists with yet another technique to control the coherent evolution of quantum systems.

Appendix

All the simulations presented in this thesis were carried out with Igor 5.03. This appendix gives the outline and details for the CPMG simulation as an example. Simulations of APCPMG, CP, APCP were done in a similar manner. This finite-pulse simulation procedure was modified from the δ-pulse approximation simulation procedure wrote by Kenny MacLean.

The flow chart of the CPMG simulation procedure is shown in Figure A-1. The first big step of the simulation is to build a Silicon diamond lattice. This step is achieved by a few functions. The first function *fcc(N)* is to build a simple FCC lattice, which is then used to create the diamond lattice out of the FCC lattice using the function *Diamondvalue()*. This Silicon diamond lattice is later chopped to have a spherical boundary of radius R using the function *SphericaLattice(R)*. Note that for convenience, function *Dimondvalue()* and *SphericalLattice(R)* are called in the end of the function *fcc(N)*, so the user only needs to run function *fcc(N)* to get a spherical Silicon diamond lattice. Here N=5 can produce a lattice with 525 sites, which is large enough to accommodate the small number of spins used in our simulations (mostly $\leq$ 6 spins) with 4.67% natural abundance.

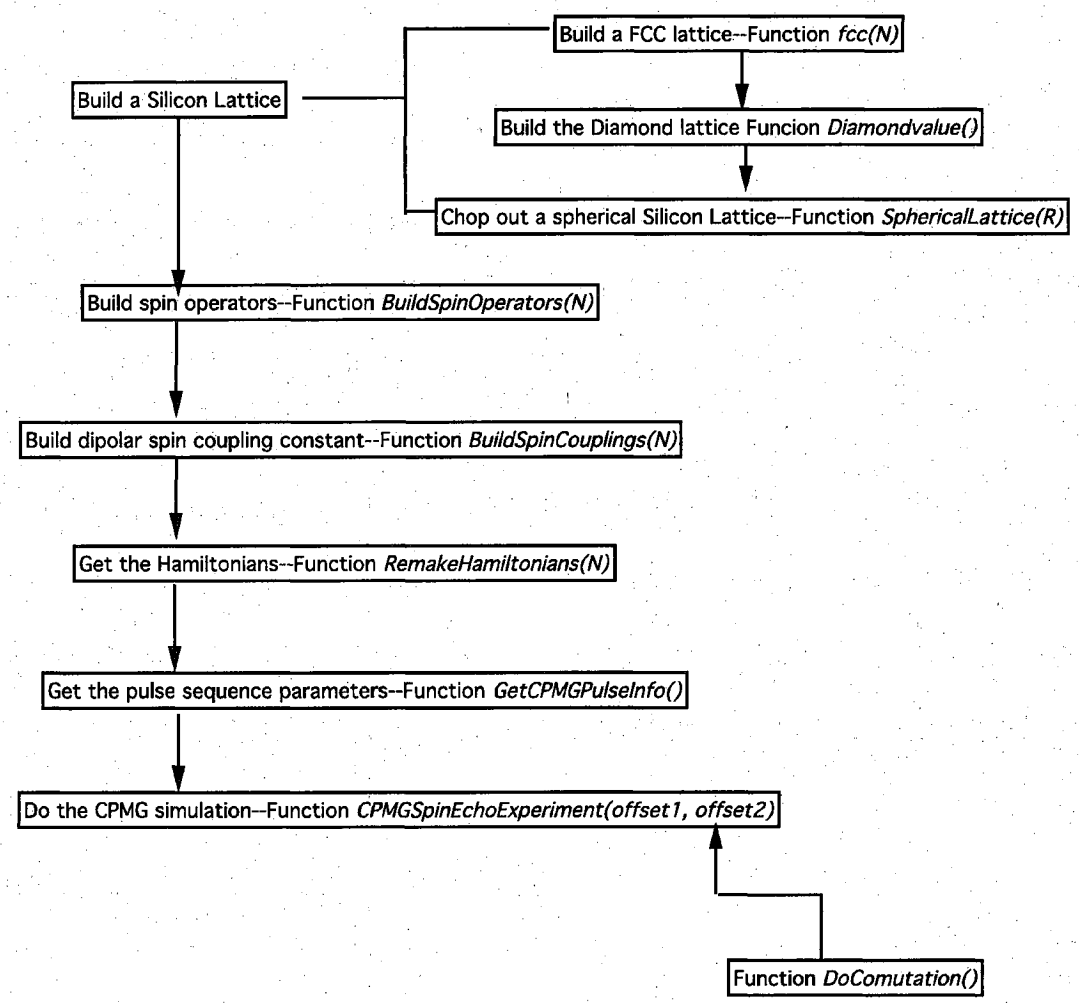

Figure A-1: Flow chart for CPMG simulation procedure using Igor 5.03

The second step is to build the spin operators $I_{x_i}, I_{y_i}, I_{z_i}$, where $i = 1, 2, \cdots$ N and N is the number of spins included in the simulation. Each spin operator is represented by a $2^N \times 2^N$ matrix in I_z basis.

The dipolar coupling constant is calculated in the third step using the function *BuildSpinCouplings(N)*. In this function, the ^{29}Si spins are populated on the spherical Silicon lattice around a center spin according the nature abundance of 4.67%. Then N-1 spins with the biggest dipolar coupling constant to the center spin are chosen. These N-1 spins plus the center spin are the N spins chosen for a single DR simulation, whose lattice coordinates are used to calculate the dipolar coupling constants.

Once all the spins are chosen and their dipolar coupling constants are calculated in the third step, each Hamiltonian can be constructed using the proper spin operators built in the second step. All the Hamiltonians are constructed in the fourth step using the function *RemakeHamiltonian(N)*. For CPMG, four Hamiltonians are used, $\mathcal{H}_1$ during the free evolution, $\mathcal{H}_2$ during the first tipping pulse 90_X , and $\mathcal{H}_3$ and $\mathcal{H}_4$ for the two 180_Y pulse (for CPMG,$\mathcal{H}_3$ and $\mathcal{H}_4$ are the same).

All the parameters used in the CPMG simulation are input in the fifth step using function *GetCPMGPulseInfo()*. This function will give dialogue windows to let the user to input values such as the spin number N, the number of disorder realizations, the pulse strength, the time delay τ, the number (N_1) of data points during the 90_X pulse, the number (N_2) of data points during the delay τ. The placement of data points are shown in Figure A-2. There is always one point at the beginning of a pulse

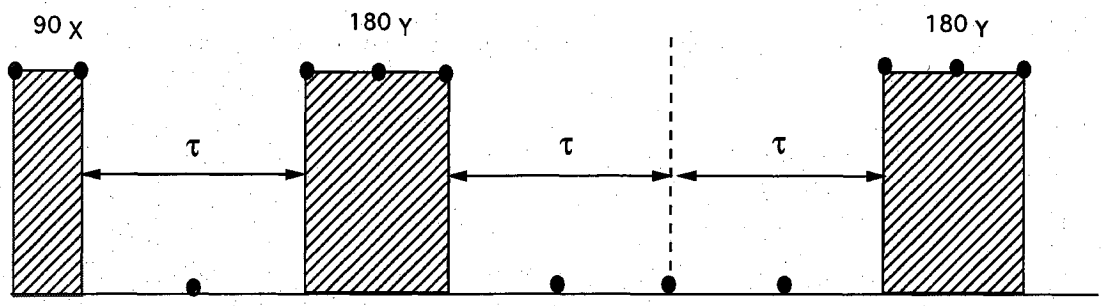

Figure A-2: The detailed placements of the data points for CPMG simulation, for $N_1 = 2$ and $N_2 = 1$.

and another point at the end of the pulse, which defines the precise duration of each pulse. So the minimum value for N_1 is 2, and the minimum value for N_2 is 1. The dwell time (the time delay between two adjacent points) has a fixed value during all the pulses and another fixed value during all the free evolution periods. If τ is a long delay and there is an echo expected in between two π pulses, then N_2 should be large enough to show the echo.

The major controlling part of the procedure that calls other functions is *CPMGSpinEchoExperiment(f_1, f_2)*, where f_2 is the Zeeman spread varying for each spin (each spin has a different Zeeman offset drawn from a Gaussian distribution with FWHM=f_2 Hz), while f_1 is the Zeeman spread varying from DR to DR (all the spins in one DR have the same offset drawn from a Gaussian distribution with FWHM=f_1 Hz).

The major part of calculation is done by the function *DoComputation()*. During this function, each Hamiltonian, for example $\mathcal{H}_1$, is diagonalized to solve for the eigenvalues and eigenvectors. All the eigenvectors are written as a unitary matrix

$\mathcal{U}$ and its corresponding $\mathcal{U}^\dagger$ is obtained. To ensure that the eigenvalues and unitary matrices are correct, two check points are placed in the function. The first check is $\mathcal{U}\mathcal{U}^\dagger = I$, where if the product $\mathcal{U}\mathcal{U}^\dagger$ has a diagonal entry being out of the range of 1 ± 10^{-4}, an error message will be sent and the function will be aborted. The second check is $\mathcal{U}\mathcal{E}\mathcal{U}^\dagger$, where $\mathcal{E}$ is a diagonal matrix with the eigenvalues. If any entry of the checking matrix $\mathcal{H}_1 - \mathcal{U}\mathcal{E}\mathcal{U}^\dagger$ is bigger than 10^{-3}, an error will be sent and the procedure will be aborted. Moreover, at the beginning of each pulse, the density matrix will be transformed to the corresponding eigenbasis of the pulse Hamiltonian ($\mathcal{H}_2$, $\mathcal{H}_3$, or $\mathcal{H}_4$); at the end of each pulse, the density matrix will be transformed to the eigenbasis of the free evolution Hamiltonian $\mathcal{H}_1$.

Since most of the functions are called in the controlling procedure, only two functions are needed to executed for a CPMG simulation:

(1) *fcc(N)*

(2) *CPMGSpinEchoExperiment(f_1, f_2).*

Note that more complicated simulations that have been done during this thesis project were carried out with another procedure, which is not as user-friendly since it is trying to accommodate many different needs. This complicated procedure will not be discussed here, but it can be understood based on the understanding of this simpler CPMG simulation.

Bibliography

[1] A. Abragam. *The Principles of Nuclear Magnetism.* The International series of monographs on physics. Clarendon Press, Oxford, 1983.

[2] R. H. Acosta, R. C. Zamar, and G. A. Monti. NMR Proton Spin Dynamics in Thermotropic Liquid Crystals Subject to Multipulse Excitation. *Physical Review E*, 68:041705, 2003.

[3] A. Allerhand. Analysis of Carr-Purcell Spin-echo NMR Experiments on Multiple-spin Systems I. the Effect of Homonuclear Coupling. *Journal of Chemical Physics*, 44:1, 1966.

[4] H. Alloul and P. Dellouve. Spin Localization in Si:P – Direct Evidence From ^{31}P NMR. *Physical Review Letters*, 59:578, 1987.

[5] E. R. Andrew, A. Bradbury, and R. G. Eades. Nuclear Magnetic Resonance Spectra from a Crystal rotated at High Speed. *Nature*, 182:1659, 1958.

[6] E. R. Andrew, A. Bradbury, and R. G. Eades. Removal of Dipolar Broadening of Nuclear Magnetic Resonance Spectra of Solids by Specimen Rotation. *Nature*, 183:1802, 1959.

[7] George B. Arfken and Hans-Jurgen Weber. *Mathematical Methods for Physicists.* Elsevier, Boston, 6th edition, 2005.

[8] F. Bloch. Nuclear Induction. *Physical Review*, 70:460, 1946.

[9] F. Bloch, W. W. Hansen, and M. Packard. Nuclear Induction. *Physical Review*, 69:127, 1946.

[10] F. Bloch, W. W. Hansen, and M. Packard. The Nuclear Induction Experiment. *Physical Review*, 70:474, 1946.

[11] G. A. Bonvallet. *Differential Scanning Calorimetric Study of the Nematic Liquid Crystal 5CB.* Physics Department, The College of Wooster, Wooster, Ohio 44691.

[12] P. Caravatti, M. H. Levitt, and R. R. Ernst. Selective Excitation in Solid-State NMR in the Presence of Multiple-Pulse Line Narrowing. *Journal of Magnetic Resonance*, 68:323, 1986.

[13] H. Y. Carr and E. M. Purcell. Effects of Diffusion on Free Precession in Nuclear Magnetic Resonance Experiments. *Physical Review*, 94:630, 1954.

[14] A. B. Cohen. *Concepts of Nuclear Physics.* McGraw-Hill, 1971.

[15] D. G. Cory, A. F. Fahmy, and T. F. Havel. Ensemble Quantum Computing by NMR Spectroscopy. *Proceedings of the National Academy of Sciences of the United States of America*, 94:1634, 1997.

[16] D. E. Demco and B. Blumich. Solid-state NMR imaging methods. Part II: Line narrowing. *Concepts in Magnetic Resonance*, 12:269, 2000.

[17] A. E. Dementyev, D. Li, K. MacLean, and S. E. Barrett. Anomalies in the NMR of Silicon: Unexpected Spin Echoes in a Dilute Dipolar Solid. *Physical Review B*, 68:153302, 2003.

[18] Anatoly E. Dementyev. *Spin in the Quantum Hall Effect: OPNMR Studies of Skyrmions and Composite Fermions.* PhD thesis, Department of Physics, Yale University, May 2004.

[19] W. C. Dickinson. Dependence of the ^{19}F Nuclear Resonance Position on Chemical Compound. *Physical Review*, 77:736, 1950.

[20] D. P. DiVincenzo. Quantum Computation. *Science*, 270:255, 1995.

[21] D. P. DiVincenzo and D. Loss. Quantum Computers and Quantum Coherence. *Journal of Magnetism and Magnetic Materials*, 200:202, 1999.

[22] Ronald Y. Dong. *Nuclear Magnetic Resonance of Liquid Crystals.* Springer, second edition edition, 1997.

[23] R. R. Ernst, G. Bodenhausen, and A. Wokaun. Principles of Nuclear Magnetic Resonance.

[24] T. C. Farrar. *An Introduction to Pulse NMR Spectroscopy.* Farragut Press, Chicago, 1987.

[25] M. B. Franzoni and P. R. Levstein. Manifestations of the Absence of Spin Diffusion in Multipulse NMR Experiments on Diluted Dipolar Solids. *Physical Review B*, 72:235410, 2005.

[26] Ray Freeman. *Spin Choreography : Basic Steps in High Resolution NMR.* Spektrum, Oxford, 1997.

[27] Eiichi Fukushima and Stephen B.W Roeder. *Experimental Pulse NMR : a Nuts and Bolts Approach.* Addison-Wesley Pub. Co., Advanced Book Program, Reading, Mass., 1981.

[28] S. E. Fuller, E. M. Meintjes, and W. W. Warren. Impurity NMR Study of the Acceptor Band in Si(B). *Physical Review Letters*, 76:2806, 1996.

[29] P. Glover and P. Mansfield. Limits to Magnetic Resonance Microscopy. *Reports on Progress in Physics*, 65:1489, 2002.

[30] H. S. Gutowsky. Chemical Shifts in the Magnetic Resonance of ^{19}F. *Physical Review*, 80:110, 1950.

[31] H. S. Gutowsky and G. E. Pake. Nuclear Magnetism in Studies of Molecular Structure and Rotation in Solids: Ammonium Salts. *Journal of Chemical Physics*, 16:1164, 1948.

[32] H. S. Gutowsky and G. E. Pake. Structural Investigations by Means of Nuclear

Magnetism. II. Hindered Rotation in Solids. *Journal of Chemical Physics*, 18:162, 1950.

[33] U. Haeberlen, J. D. Ellett, and J. S. Waugh. Resonance Offset Effects in Multiple-pulse NMR Experiments. *Journal of Chemical Physics*, 55:53, 1971.

[34] U. Haeberlen and J. S. Waugh. Coherent Averaging Effects in Magnetic Resonance. *Physical Review*, 175:453, 1968.

[35] Ulrich Haeberlen. *High Resolution NMR in Solids : Selective Averaging*, volume 1. Academic Press, New York, 1976.

[36] E. L. Hahn. Spin Echoes. *Physical Review*, 80:580, 1950.

[37] P. A. Heiney, J. E. Fischer, A. R. McGhie, W. J. Romanow, A. M. Denenstein, J. P. McCauley, and A. B. Smith. Orientational Ordering Transition in Solid C_{60}. *Physical Review Letters*, 66:2911, 1991.

[38] John David Jackson. *Classical Electrodynamics*. Wiley, New York, 3rd ed edition, 1999.

[39] R. D. Johnson, C. S. Yannoni, H. C. Dorn, J. R. Salem, and D. S. Bethune. C_{60} Rotation in the Solid State: Dynamics of a Faceted Spherical Top . *Science*, 255:1235, 1992.

[40] B. E. Kane. A Silicon-Based Nuclear Spin Quantum Computer. *Nature*, 393:133, 1998.

[41] B. E. Kane. Silicon-Based Quantum Computation. *Fortschritte Der Physik-Progress of Physics*, 48:1023, 2000.

[42] H. Kessemeier and W. K. Rhim. NMR Line Narrowing by Means of Rotary Spin Echoes. *Physical Review B*, 5:761, 1972.

[43] T. D. Ladd, J. R. Goldman, F. Yamaguchi, Y. Yamamoto, E. Abe, and K. M. Itoh. All-Silicon Quantum Computer. *Physical Review Letters*, 89:017901, 2002.

[44] T. D. Ladd, D. Maryenko, Y. Yamamoto, E. Abe, and K. M. Itoh. Coherence Time of Decoupled Nuclear Spins in Silicon. *Physical Review B*, 71:014401, 2005.

[45] P. C. Lauterbur. Image Formation by Induced Local Interactions: Examples Employing Nuclear Magnetic Resonance. *Nature*, 242:190, 1973.

[46] Dale Li. *Unexpected Spin Echoes in Dipolar Solids: Instrinsic Effects of Finite Pi Pulses on Quantum Coherence.* PhD thesis, Department of Physics, Yale University, December 2007.

[47] Dale Li, A. E. Dementyev, Yanqun Dong, R. Ramos, and S. E. Barrett. Generating Unexpected Spin Echoes in Dipolar Solids with π Pulses. *Physical Review Letters*, 98:190401, 2007.

[48] Dale Li, Yanqun Dong, Rona G. Ramos, John D. Murray, Kenneth MacLean, Anatoly E. Dementyev, and Sean E. Barrett. The Intrinsic Origin of Spin Echoes

in Dipolar Solids Generated by Strong π Pulses. *Physical Review B*, 77:214306, 2008.

[49] David R. Lide and H. P. R. Frederikse, editors. *CRC Handbook of Chemistry and Physics.* CRC Press, Inc., 75th edition, 1994.

[50] I. J. Lowe. Free Induction Decays of Rotating Solids. *Physical Review Letters*, 2:285, 1959.

[51] S. A. Lyon. Si:P ESR CPMG. Private Communication.

[52] I. Huang M. Nielsen. *Quantum Computation and Quantum Information.* Cambridge University Press, 2000.

[53] W. Magnus. On the Exponential Solution of Differential Equations for A Linear Operator. *Communications on Pure and Applied Mathematics*, 7:649, 1954.

[54] F. Mandl. *Statistical Physics.* John Wiley and Sons, 2nd edition, 1988.

[55] P. Mansfield. Symmetrized Pulse Sequences in High Resolution NMR in Solids. *Journal of Physics Part C Solid State Physics*, 4:1444, 1971.

[56] P. Mansfield and P. K. Grannell. NMR Diffraction in Solids? *Journal of Physics-Solid State Physics*, 6:L422, 1973.

[57] M. M. Maricq. Application of Average Hamiltonian Theory to the NMR of Solids. *Physical Review B*, 25:6622, 1982.

[58] S. Matsui. Solid-state NMR Imaging by Magic Sandwich Echoes. *Chemical Physics Letters*, 179:187, 1991.

[59] S. Matsui. Suppressing the Zero-Frequency Artifact in Magic-Sandwich-Echo Proton Images of Solids. *Journal of Magnetic Resonance*, 98:618, 1992.

[60] M. Mehring. *Principles of High-Resolution NMR in Solids.* Springer-Verlag, Berlin, 2nd, rev. and enl. ed edition, 1983.

[61] M. Mehring and G. Sinning. Dynamics of Heteronuclear Spin Coupling and Decoupling in Solids. *Physical Review B*, 15:2519, 1977.

[62] S. Meiboom and D. Gill. Modified Spin-echo Method for Measureing Nuclear Relaxation Times. *Review of Scientific Instruments*, 29:688, 1958.

[63] O. Mensio, C. E. Gonzalez, and R. C. Zamar. Dipolar Quasi-invariants in 1H NMR of Nematic Thermotropic Liquid Crystals. *Physical Review E*, 71:011704, 2005.

[64] O. Mensio, R. C. Zamar, E. Anoardo, R. H. Acosta, and R. Y. Dong. On the Role of Collective and Local Molecular Fluctuations in the Relaxation of Proton Intrapair Dipolar Order in Nematic 5CB. *Journal of Chemical Physics*, 123:204911, 2005.

[65] J. B. Miller, D. G. Cory, and A. N. Garroway. Line-Narrowing Approaches

to Solid State NMR Imaging: Pulsed Gradients and Second Averaging [and Discussion]. *Philosophical Transactions Royal Society A*, 333:413, 1990.

[66] Gareth A. Morris and Ray Freeman. Selective Excitation in Fourier Transform Nuclear Magnetic Resonance. *Journal of Magnetic Resonance*, 29:433, 1978.

[67] E. D. Ostroff and J. S. Waugh. Mutiple Spin Echoes and Spin Locking in Solids. *Physical Review Letters*, 16:1097, 1966.

[68] T. L. Peck, R. L. Magin, and P. C. Lauterbur. Design and Analysis of Microcoils for NMR Microscopy . *Journal of Magnetic Resonance, Series B*, 108:114, 1995.

[69] A. Pines and J. S. Waugh. Quantitative Aspects of Coherent Averaging – Simple Treatment of Resonance Offset Processes in Multiple-Pulse NMR. *Journal of Magnetic Resonance*, 8:354, 1972.

[70] J. A. Pople. The Theory of Chemical Shifts in Nuclear Magnetic Resonance. I. Induced Current Densities. *Proceedings of the Royal Society of London*, A239:541, 1957.

[71] J. A. Pople. The Theory of Chemical Shifts in Nuclear Magnetic Resonance. II. Interpretation of Proton Shifts. *Proceedings of the Royal Society of London*, A239:550, 1957.

[72] V. Privman, I. D. Vagner, and G. Kventsel. Quantum Computation in Auantum-Hall Systems. *Physics Letters A*, 239:141, 1998.

[73] W. G. Proctor and F. C. Yu. The Dependence of a Nuclear Magnetic Resonance Frequency upon Chemical Compound. *Physical Review*, 77:717, 1950.

[74] E. M. Purcell, H. C. Torrey, and R. V. Pound. Resonance Absorption by Nuclear Magnetic Moments in a Solid. *Physical Review*, 69:37, 1946.

[75] R. G. Ramos, Yanqun Dong, Dale Li, and S. E. Barrett. (to be published).

[76] W. K. Rhim, D. D. Elleman, and R. W. Vaughan. Enhanced Resolution for Solid-State NMR. *Journal of Chemical Physics*, 58:1772, 1973.

[77] W. K. Rhim and H. Kessemeier. Transverse-Magnetization Recovery in the Rotating Frame. *Physical Review B*, 3:3655, 1971.

[78] W. K. Rhim, A. Pines, and J. S. Waugh. Violation of Spin-Temperature Hypothesis. *Physical Review Letters*, 25:218, 1970.

[79] W. K. Rhim, A. Pines, and J. S. Waugh. Time-Reversal Experiments in Dipolar-Coupled Spin Systems. *Physical Review B*, 3:684, 1971.

[80] D. Sakellariou, G. Le Goff, and J. F. Jacquinot. High-resolution, High-sensitivity NMR of Nanoliter Anisotropic Samples by Coil Spinning. *Nature (London)*, 447:694, 2007.

[81] J. J Sakurai and San Fu Tuan. *Modern Quantum Mechanics*. Addison-Wesley Pub. Co., Reading, Mass., 1994.

[82] Y. Shimoikeda, H. Utsumi, K. Saito, T. Shimizu, and T. Nakai. Fullerene as a Standard Sample for Adjusting the NMR Spectral Resolution in Multiple-Quantum Magic-Angle-Spinning Experiments. *Analytial Sciences*, 23:1007, 2007.

[83] R. G. Shulman and B. J. Wyluda. Nuclear Magnetic Resonance of ^{29}SI in N-type and P-Type Silicon. *Physical Review*, 103:1127, 1956.

[84] C. P. Slichter. *Principles of Magnetic Resonance.* Springer, New York, 3rd edition, 1990.

[85] R. K. Sundfors and D. F. Holcomb. Nuclear Magnetic Resonance Studies of Metallic Transition in Doped Silicon. *Physical Review A*, 136:810, 1964.

[86] K. Takegoshi and C. A. McDowell. A "Magic Echo" Pulse Sequence for the High-resolution NMR Spectra of Abundant Spins in Solids. *Chemical Physics Letters*, 116:100, 1985.

[87] R. Tycko, G. Dabbagh, R. M. Fleming, R. C. Haddon, A. V. Makhija, and S. M. Zahurak. Molecular dynamics and the phase transition in solid C_{60}. *Physical Review Letters*, 67:1886, 1991.

[88] R. Tycko, R. C. Haddon, G. Dabbagh, S. H. Glarum, D. C. Douglass, and A. M. Mujsce. Solid-State Magnetic-Resonance Spectroscopy of Fullerenes. *Journal of Physical Chemistry*, 95:518, 1991.

[89] R. Vrijen, E. Yablonovitch, K. Wang, H. W. Jiang, A. Balandin, V. Roychowd-

hury, T. Mor, and D. DiVincenzo. Electron-Spin-Resonance Transistors for Quantum Computing in Silicon-Germanium Heterostructures. *Physical Review A*, 62:012306, 2000.

[90] S. Watanabe and S. Sasaki. ^{29}Si Nuclear-Spin Decoherence Process Directly Observed by Multiple Spin-Echoes for Pure and Carrier-less Silicon. *Japanese Journal of Applied Physics Part 2-Letters*, 42:L1350, 2003.

[91] Y. Wu, J. L. Ackerman, H. M. Kim, C. Rey, A. Barroug, and M. J. Glimcher. Nuclear Magnetic Resonance Spin-Spin Relaxation of the Crystals of Bone, Dental Enamel, and Synthetic Hydroxyapatites. *Journal of Bone and Mineral Research*, 17:472, 2002.

[92] Y. Wu, D. A. Chesler, M. J. Climcher, L. Garrido, J. Wang, H. J. Jiang, and J. L. Ackerman. Multinuclear Solid-State Three-Dimensional MRI of Bone and Synthetic Calcium Phosphates. *Proceedings of the National Academy of Sciences of USA*, 96:1574, 1999.

[93] K. Yamauchi, J. W. G. Janssen, and A. P. M. Kentgens. Implementing Solenoid Microcoils for Wide-line Solid-state NMR . *Journal of Magnetic Resonance*, 167:87, 2004.

[94] C. S. Yannoni, R. D. Johnson, G. Meijer, D. S. Bethune, and J. R. Salem. ^{13}C NMR-Study of the C_{60} Cluster in the Solid-State-Molecular-Motion and Carbon Chemical-Shift Anisotropy. *Journal of Physical Chemistry*, 95:9, 1991.